2011

Removal of particulate matter from condensable vapors using a moving bed granular filter

Lysle Ervin Whitmer
Iowa State University

Removal of particulate matter from condensable vapors using a moving bed granular filter

by

Lysle Ervin Whitmer

A thesis submitted to the graduate faculty
in partial fulfillment of the requirements for the degree of
MASTER OF SCIENCE

Co-majors: Mechanical Engineering; Biorenewable Resources and Technology

Program of Study Committee:
Robert Brown, Major Professor
Theodore Heindel
Stephen Vardeman

Iowa State University

Ames, Iowa

2011

TABLE OF CONTENTS

LIST OF FIGURES

LIST OF TABLES

ACKNOWLEDGEMENTS

I dedicate this work to my late grandfather, Richard "Dick" Ervin, who even in death provides a bright beacon and shining example of that which can be accomplished through hard work and dedication. I would also like to acknowledge the unwavering support of my mother and father, without whom, I would never have the solid foundation on which to build a successful career and live a fruitful life.

Secondly, I must thank Dr. Robert Brown for the opportunity to conduct such fascinating work, and the guidance that helped shape an engineer into a research scientist. I would also like to thank Dr. Theodore Heindel and Dr. Stephen Vardeman for agreement to reside on my committee and their support through the research process.

I would like to recognize Jim Moreland and Jay Hamilton from Sargent Metal Fabrication for aide in fabricating the filter. I would also like to provide special thanks AJ Pollard, Andrew Olthoff, Andrew Friend, Trevor Heithoff, Clark Ennis, Dustin Dalluge, Nick Creager and Jordan Funkhouser for their help in the accelerated build and testing process, without whom the project surely would not have been completed to such high standards. I would also like to thank Robbie Hable, Cassidy Leclaire, John Hoyt, Patrick Johnston, and Marge Rover for their help with the laboratory analysis. I would also like to recognize Jerry Amenson and Warren Straszheim of the Materials Analysis and Research Lab (MARL) for their help with the SEM analysis of materials produced in my research.

Lastly, I would like to immensely thank Kelsey for her support and sacrifice through my entire graduate school experience, without which, the process would have been unachievable and its completion unfulfilling.

ABSTRACT

Products from the fast pyrolysis of biomass were filtered at 500°C using a moving bed granular filter. The filter was able to operate continuously at stable temperatures and pressures at a range of granular flow rates. Pyrolysis product yields with the filter were similar to those obtained during baseline operation. Imaging of spent filtration media confirmed the presence of primary char, demonstrating the ability of the filter to remove particulate matter in-situ. Additional imaging also confirmed the presence of filtration media derived dust contaminating bio-oil samples. The filter was not able to reduce trace metal content of resulting bio-oil over baseline samples due in part to the dust contamination. Accelerated aging trials conducted on the filtered bio-oil confirmed oligomerization of the samples likely due to the presence of alkali remaining in the oil. A modeling study of the aged samples revealed a trend of increased aging with increased filtration granular flow rate.

CHAPTER 1. OVERVIEW

1.1 Introduction

High temperature filtration presents many challenges to industrial processes as an application pushing the limits of material capabilities and requiring the ability to maintain steady operation while meeting increasingly strict emission standards. The fast pyrolysis of biomass introduces the need for increased solids removal in one of the harshest environments possible; a complex mixture of acidic compounds, alkali earth metals, long chain hydrocarbons and well over 300 compounds existing at a temperature of 500°C.[1]

1.1.1 Goal

The goal of this research was to investigate an alternative hot gas cleanup system and apply it to the harsh conditions present in the fast pyrolysis of biomass. The system would be evaluated based on its ability to remove fine solid particulate matter from the hot gas stream as well as the impact of the filtration process on overall product distribution and quality. Quality was evaluated using state-of-the art methodologies developed for analysis of pyrolysis products.

CHAPTER 2. BACKGROUND AND LITERATURE REVIEW

2.1 The Fast Pyrolysis of Biomass

Fast pyrolysis of biomass is the rapid thermal decomposition of organic compounds in the absence of oxygen to produce liquids, gases, and char. The distribution of products depends on the biomass composition, the heating rate and the duration of heating. Liquid yields as high as 78-percent are possible with relatively short residence times of 0.5-2 s, moderate temperatures of 400-600°C and with rapid quenching at the end of the process.[2] The resulting brownish liquid that is collected is called bio-oil; the bio-oil is typically acidic, viscous, and heavily aromatic.

Pyrolysis is believed to take place in multiple stages[3]. First, primary reactions occur as moisture and volatiles are expelled from the biomass particles forming gases, vapors, aerosols, and a carbonaceous residue resembling the biomass (referred to as primary char). The liquid aerosol droplets, gases, and vapors is referred to as the pyrolysis vapor stream. These common reactions can be seen in any backyard fire-pit as the white smoke rises from a smoldering fire. Secondary reactions occur between the primary vapors, aerosols, and the char. These secondary reactions are thought to be autocatalytic and result in the cracking of pyrolysis vapors into water, low molecular weight oxygenated organic compounds, and additional secondary char (which hardly resemble the biomass feedstock). The secondary reactions are, in most cases, undesirable for bio-oil production; and therefore, the residence time between the vapors and char particles is minimized in order to reduce opportunity for secondary reactions.

2.2 Particulate Matter

Particulate matter is simply defined as particles suspended in a fluid medium. These particles can be either solid particulate matter or very fine liquid aerosol droplets and are typically on the order of 0.1 to 10 µm in size. The parameters that describe particles are size, concentration, and chemical composition.[4] The most crucial of these parameters with regards to filtration is particle size, usually defined by the diameter of the particle. A chart is provided in Figure 1 that gives examples of particle size ranges; in the case of non-spherical particles, an equivalent diameter is assigned. Aerodynamic diameter, for example, is the diameter of a spherical particle with unit density and equal terminal settling velocity. Another defining characteristic of particles less than 1µm is their ability to agglomerate to sizes larger than several µm. These particles are often characterized by their mobility diameter which is the diameter of a sphere with equivalent velocity to momentum ratio of the agglomerate.

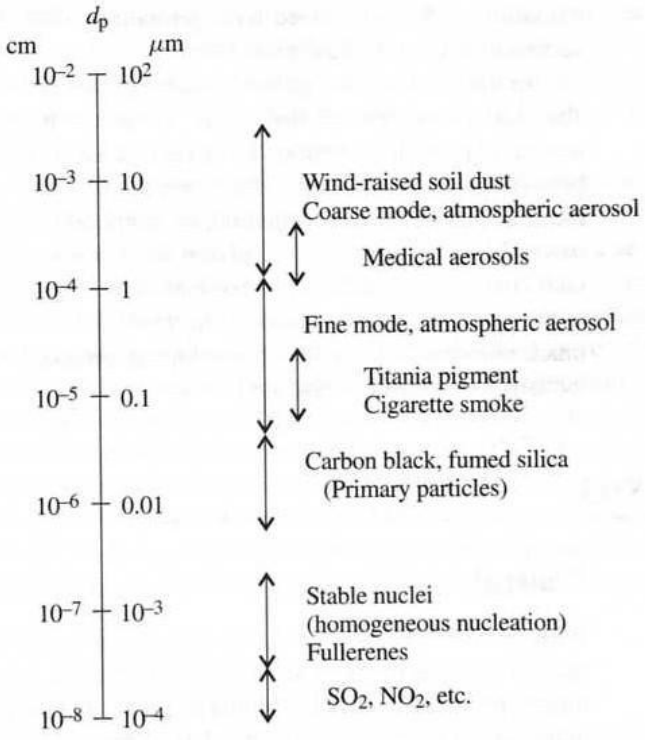

Figure 1: Examples of Particle Size Ranges [4]

There are several methods that can be used to define the concentration of particulate matter. Number concentration is the number of particles per unit volume of gas while mass concentration is the mass of particles per unit volume of gas. Typical mass concentrations are 20 μg/m^3 for unpolluted air versus 200 μg/m^3 for polluted air.[4]

Solid particulate matter and aerosols as they apply to pyrolysis, can be distinguished by their distinct chemical makeup. Particulate matter tends to be made of substances that cannot exist as a liquid such as black carbon or mineral matter. Aerosols tend to be classified as very fine liquid droplets. However, aerosols should not be confused with vapors, which are defined as condensable gases and can be differentiated by the way they are collected. Aerosols have a tendency to collect only when they impinge on a surface. Vapors, however, tend to collect on surfaces cooled below the dew point of the vapor. This can happen several

ways; heat could be removed from the system using a cooling medium causing vapors to condense, and the partial pressure of the vapor could be lowered through geometry changes in the system also allowing the vapor to condense. Diameter ranges can be specified in order in an effort to distinguish between solid particulate matter, liquid aerosols and vapors. Figure 2 illustrates particle size ranges of common materials. The solid char particulate matter produced during pyrolysis corresponds well with that of coal dust from 1 to 100 µm in size. Aerosols produced in pyrolysis are believed to correspond well with the smoke range indicated on the chart from 0.01 to 1 µm. Vapors will be considered to fall within the size range of gas molecules, from 10^{-5} to 10^{-3} µm. It could be considered that under proper conditions, aerosols can evaporate into vapors and vapors can condense into aerosols and solid particulate matter remains incapable of phase changes.

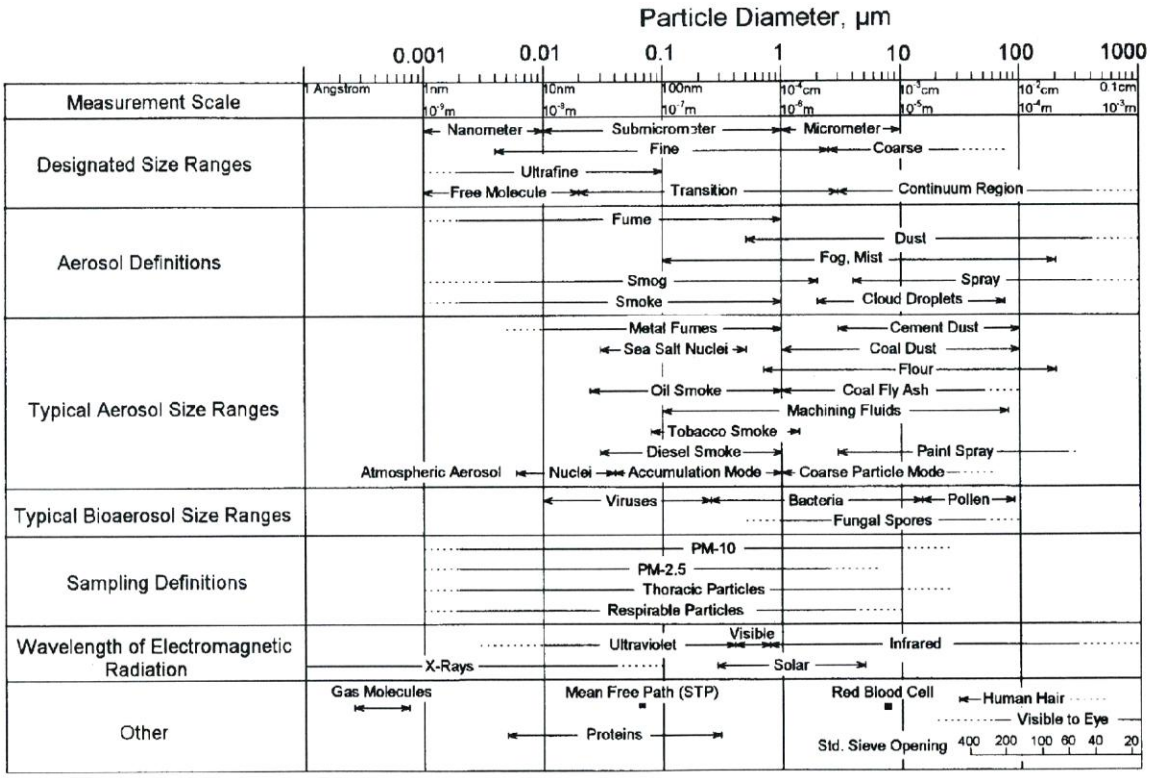

Figure 2: Particle Size Ranges and Definitions for Aerosols[5]

2.3 Aerosol Collection

Several mechanisms contribute to the collection of aerosols depending on collection geometry and particle size. Particle sedimentation occurs when an aerosol is pulled out of the stream by gravity. Simply put, the gravitational force acting on the aerosol mass is too great to overcome inertial force of the gas stream propelling it. Straining can occur when the aerosol laden stream is forced through a filtration media in which the pore size of the media is smaller than the aerosol. The gas passes through the media but the aerosol is caught and strained out.

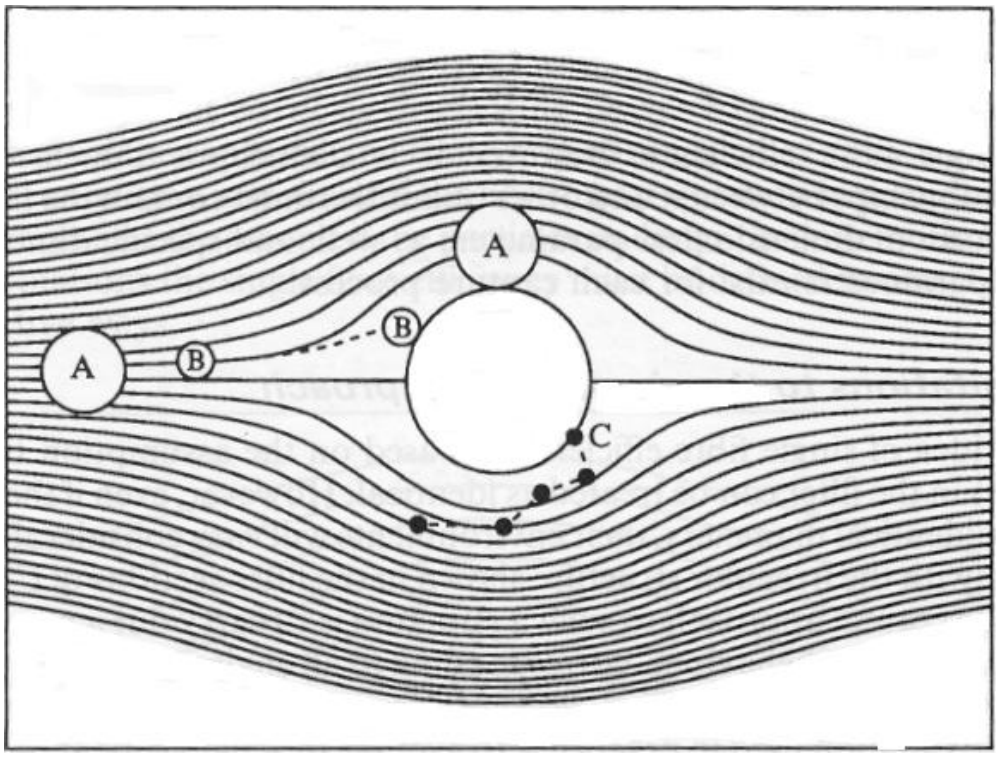

Figure 3: Mechanisms of deposition: A. Interception B. Inertial impaction C. Diffusion [6]

Figure 3 depicts three of the most utilized mechanisms used to collect aerosols; these include interception, impaction, and diffusion. The figure shows an aerosol-laden fluid

streaming around a collection device placed in the fluid's path. This device could be a cylinder or sphere; but it is not hard to adapt the same mechanisms in other geometries, for example, such as 90° piping bends or a plate collector. Particle A undergoes collection by interception, which occurs when the fluid streamlines bring the aerosol close enough to the collection device that the aerosol sticks to the surface. Particle B undergoes collection by inertial impaction. Aerosols entrained in a fluid stream have a certain inertia based on the velocity of the flow and the mass of the particle. When the fluid stream diverges to flow around the collection device, some of the aerosols will carry enough momentum to disengage from the stream and impact on the collection surface. Inertial impaction is a very common mechanism for removal of aerosols. Particle C depicts removal by diffusion. Diffusion is a mass transfer process that is driven by the aerosol concentration at the surface of the collection device. Similar to how temperature differences drive heat transfer, a concentration gradient drives mass transfer that results in Brownian motion. For submicron aerosols, Brownian diffusion force is the dominant factor in determining deposition rate.[7]

Another mechanism for collecting aerosols is electrical migration where aerosols are electrically charged and then passed through an electric field that causes the particles to diffuse to the electrodes. Charging can occur by several methods, but the most common is attaching small ions or electrons to the particles. In this process ions strike the surface of particles when traveling along field lines that pass through the particle. The ions build up on the particle and distort the field as depicted in Figure 4. Once charged, the particle repels liked charged ions and forces its movement away from the ion source and usually into a collection wall.

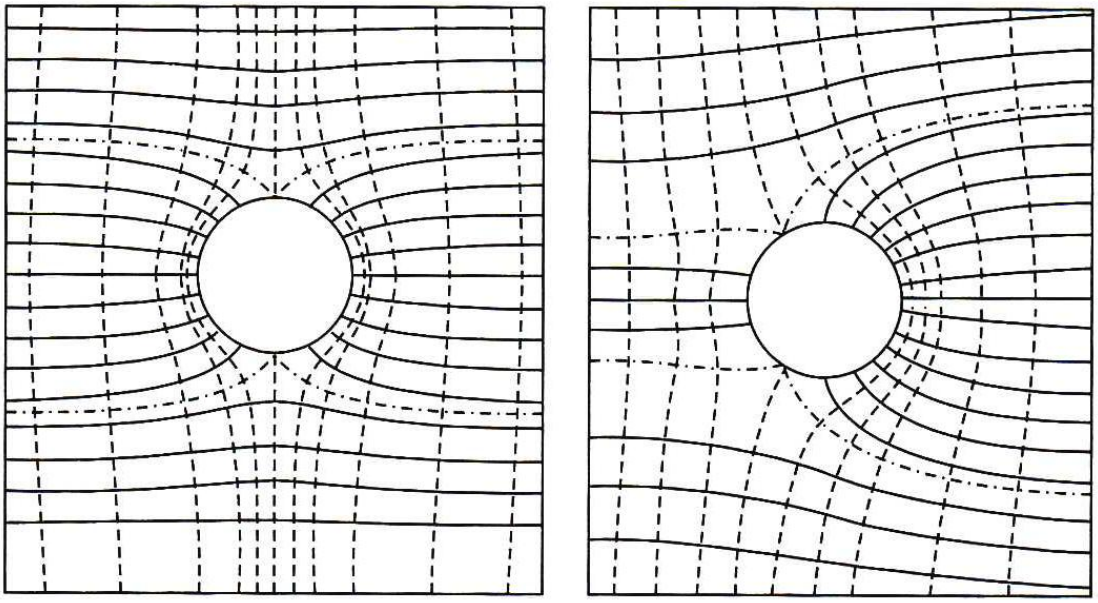

Figure 4: Electrical force (———) and equipotential (- - - -) lines around (a) an unchanged conducting sphere in a uniform field and (b) a partially charged conducting sphere in a uniform field. Ions present in the field migrate along the electric force lines: those moving along lines that intersect the surface tend to collide with the sphere. As the particle becomes charged, the field lines become distorted in such a way that the charging process slows [4]

It is interesting to note the role Van der Waals forces play in the collection of aerosols. While the mechanisms described thus far act on aerosols over large special differences, Van der Waals forces are important when particles are in close proximity to surfaces. Figure 5 depicts the interaction of a spherical particle with a flat surface. As distance S decreases, the attractive Van der Waals force increases between the particle and the surface. Van der Waals forces are due to random fluctuation of electron position in electron clouds that when properly aligned can create a dipole with enough force to act on small particles like aerosols. It is these forces that dominate when a particle gets near a collection surface and allows it to stick to the wall.[4]

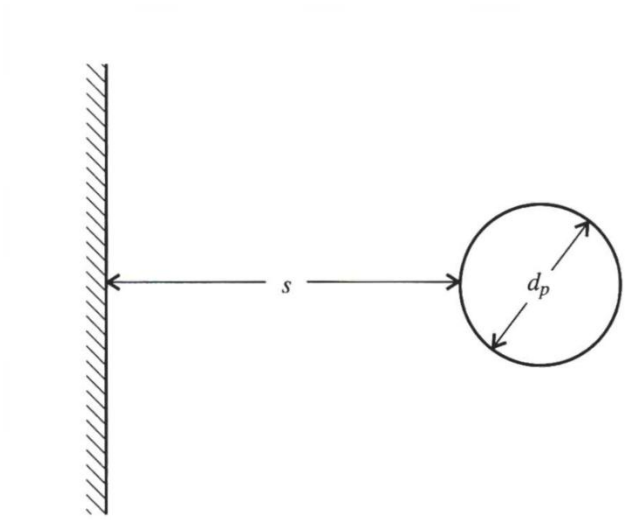

Figure 5: Interaction of a Spherical Particle with a Large Body Bounded by a Flat Surface [4]

A variety of collection devices have proven effective in removing aerosols from gas streams. Extremely common, barrier filters typically rely on straining filtration mechanism, but with an enhanced feature-the buildup of a filter cake. The fibers or mesh of the filter create small pores through which gas can pass but particles cannot. The larger particles stick in the pores and decrease the void space where gas flows. As more particles are caught in the mesh, the void space decreases and consequently the smaller particles can be caught. This buildup of particulate matter on the filter's surface increases collection efficiency by collecting smaller and smaller particles is called filter cake. However, the decrease in void space makes gas flow through the filter difficult; therefore, increases pressure drop across the filter, resulting in unsteady process conditions.

Cyclonic separators, cyclones, are typically used to remove solid particulate matter from gas streams based on a similar mechanism to that of inertial impaction. Figure 6 shows the schematic of a typical cyclone. The aerosol laden gas stream enters the annulus

tangentially in order to reduce pressure drop associated with the expansion. The gas then swirls and descends around the outer rim of the annulus before exiting the top of the cyclone. The particle's centrifugal motion carries them into the wall of the cyclone, removing them from the flow. Cyclones are very popular in pyrolysis due to their ease of manufacture, high temperature tolerance, low maintenance and high efficiency that usually exceeds 90% removal for particles greater than several μm in size.

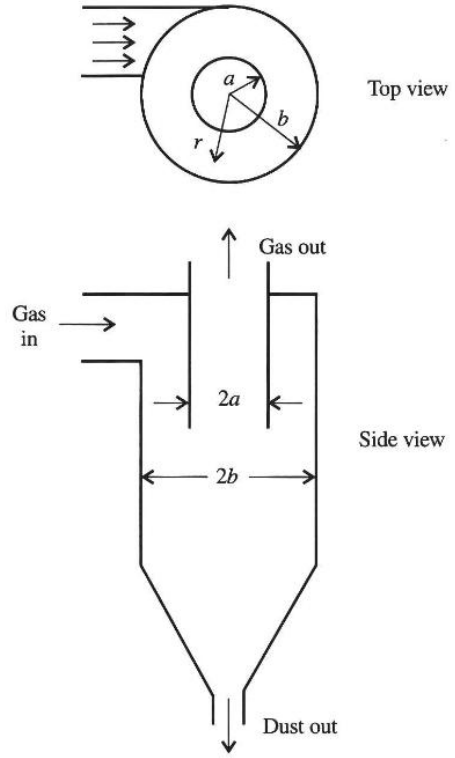

Figure 6: Schematic of a Cyclone Separator [4]

A simple but effective means of removing particulate matter is a wet scrubber. Typically, wet scrubbers utilize a chamber through which gas is passed and a mist of cleaning solution is sprayed. The liquid adheres to particles entrained in the gas and the

gravitational force on the additional mass carries the agglomeration to a collection pan in the bottom of the chamber. Consequently, the addition of the liquid can cool vapor in the gas stream, causing the vapors to condense and subsequently collect. Clean-up of power plant stack emissions often involves wet scrubbers with water as the scrubbing liquid. This limits the temperature at which the cleanup process can operate; however, some scrubbers utilizing oil, molten salt or glass as a scrubbing liquid can operate at elevated temperatures.[8] The use of wet scrubbers in pyrolysis is not likely due to the removal of desirable aerosols and vapors that are later condensed into bio-oil.

A swirling aerosol impinger uses a combination of scrubbing and cyclonic removal. Figure 7 depicts a tangential entrance, similar to a cyclone that ends in a series of jets directing gas flow at a lower reservoir annulus. The stream is designed to collect aerosols by directly impacting them onto the collection wall. The gas stream is then forced into an impinger reservoir and bubbled through to the exit of the system in an effort to further scrub particles from the gas and retain them in the solution. [9]

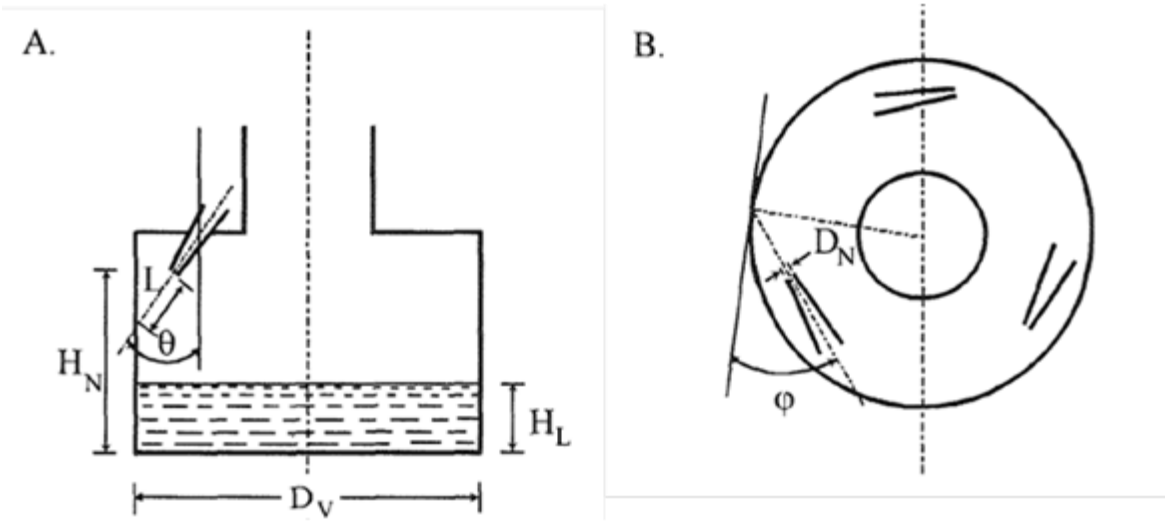

Figure 7: Schematic Diagram of Swirling Aerosol Collector (SAC): A. Side Elevation; B. Top View [9]

Electrostatic precipitators (ESPs) work on the principle of diffusion of charged particles under the action of an electric field. Particles in a gas flow are ionized by passing through a corona discharge, which produces electrons and small positively charged ions that become attached to the particles. The charged particles are passed through an electric field that accelerates them toward electrodes that collect the particles. ESPs for collecting ash from flue gas typically employ parallel plate geometries, which are cleaned by electromechanical rappers that vibrate the dust off the plates into a collection chamber. Small-scale ESPs are usually constructed from cylindrical pipe that serves as one electrode and a wire or rod located along the axis of the pipe that serves as the other electrode.

2.4 Biomass Fast Pyrolysis and the Production of Aerosols

The transport of products from fast pyrolyzers is not well understood.[10] One view is that organic compounds exit a pyrolyzer as vapor, which should be easily collected via condensation in shell-in-tube heat exchangers. An alternative is that organic compounds exist as vapors and liquid aerosols in the gas stream. In both scenarios, particulate matter, in the form of char and ash, can exit the pyrolyzer with the gas stream. Vapors can react to form compounds that are heavy enough to nucleate to liquid aerosols. Liquid aerosols formed under non-equilibrium conditions might vaporize as they are transported in the gas stream. Porous char particles entrained in the gas flow could absorb vapors and encourage unwanted secondary reactions that crack or polymerize the bio-oil. Research regarding the transport phase of pyrolysis vapors is limited due to the harsh environment in which these vapors exist. Daugaard and Brown[11] devised a method to track the mass fraction of bio-oil vapor as it exits a fluidized bed fast pyrolyzer. The results appeared to limit the mass fraction exiting as vapor to 5-10% of total output; this strongly refutes the hypothesis that most of bio-oil precursors exit the reactor as vapors. However, this would indicate that as much as 90% of the pyrolysis product stream exits the reactor as aerosols. In a second test, Daugaard highlighted the ability of aerosols collected on an impaction device to vaporize given sufficient residence time.[11] This occurrence is most likely caused by a combination of increased residence time and mass transfer interactions due to the increased slip velocity induced by their capture.

Further evidence of aerosol production in fast pyrolysis reactors has been provided in the advancement of bio-oil collection technology. In the past several years, ESPs have been introduced to target collection of aerosols existent in pyrolysis streams. Their application has

been demonstrated at Iowa State University and utilized a fluidized bed reactor equipped with traditional condenser collection train. Klauser [12] designed and installed an annular ESP for bio-oil collection after the condensers in order to remove the remaining aerosols in the product stream. This resulted in bio-oil collection with as much as 40 weight percent of the total yield.[13] The technology was further advanced by using a combination of temperature controlled condensers and ESPs to form a fractionated bio-oil recovery system as demonstrated by Sherwood-Pollard.[14] He found that by manipulating the partial pressures of the gas product stream, the vapors and aerosols could be collected independently and fractionated by macro chemical families with similar thermo-physical properties. Similarly, Garcia-Perez proposes macro chemical families as a mixture of water, monolignols, polar compounds with moderate volatility, sugars, extractive-derived compounds, heavy polar and non-polar compounds, methyl alcohol–toluene insoluble compounds and volatile organic compounds.[15] Although this process is not completely understood, the layout of condenser followed by ESP by condenser by ESP, with bio-oil collection in all fractions, supports the idea that aerosols are present throughout the condensing train. However, Sherwood-Pollard reports aerosol collection by ESPs to be 45% by mass of the total bio-oil yield, which varies with feedstock; however, only half the amount was reported by Daugaard et al.[11]. The drastic difference between aerosol production and collection volume suggests that the aerosols present at the exit of the reactor either undergo evaporation, due to adequate heat input into the system or undergo chemical cracking reactions resulting in char and gas.

Patwardhan et al. [16] suggests that volatile monomeric compounds formed from the pyrolysis of lignin are subject to secondary reactions that form oligomers. These oligomers

undergo condensation reactions in the vapor phase resulting in the production of aerosols. He also reported an increase in production of oligomeric compounds in the presence of acid suggesting their formation is acid catalyzed. Thus, fast pyrolysis can be expected to produce large quantities of liquid aerosols. These results suggest that aerosols may form from primary products of pyrolysis reactions and immediately undergo secondary reactions while in the vapor phase surrounding the biomass particle. The mechanisms surrounding these chemical reactions are not well understood and could be heat transfer or mass transfer limited, effecting aerosol production volumes within the reactor.

2.5 Stability of Bio-Oil

Bio-oil is considered a "thermochemical intermediate" in the production of biofuels. It would be transported to a centralized refinery where it would be catalytically upgraded to fuel-range hydrocarbon molecules. However, bio-oil is unstable due to the thermodynamic non-equilibrium in which it is produced. Short residence times and rapid cooling of the product stream do not allow chemical reactions to fully complete. Instead, these reactions are left to slowly terminate within the bio-oil in its collected state.[17] Ideally, upgrading or catalytic processing would take place immediately after bio-oil collection, minimizing the concern over product instability. Several factors contribute to the instability of bio-oil including acid, water, and char content. Acid compounds are thought to catalyze several reactions including transesterification, polymerization, acetalization and hydration reactions.[17]

The opinion has long been held throughout the pyrolysis community that the complete removal of char content from the pyrolysis stream will result in increased

stabilization of pyrolysis oils.[18-20] Char content is suspected of catalyzing secondary reactions that produce water and additional char, contributing to reduced bio-oil yields, reduced energy content and instability. It is suspected that this catalysis is a result of the high alkali metal content concentrated within the char.[21]

Traditionally, bio-oil stability was estimated by changes in water content and viscosity.[22] The water content measurement is capable of tracking the additional formation of water over time, a sign of aging. The viscosity measurement is able to track increases in viscosity that would result as bio-oil polymerizes further over time. However, due to the large sample volumes required, problematic calibration techniques, phase separation in bio-oil, and lack of uniformity between viscometers, other approaches have been explored in this study in order to better quantify the polymerization of bio-oil constituents over time.

One alternative method for characterizing changes in bio-oil stability is gel permeation chromatography (GPC), also known as size exclusion chromatography (SEC). GPC is a separation technique that segregates the constituents of the sample based on size. It has the ability to look at molecular weights of the constituents and generate a molecular weight distribution versus amplitude graph. As seen in Figure 8, the amplitude on the y-axis corresponds to the number of constituents in the sample that have the molecular weights shown on the x-axis. This particular graph depicts results from an early attempt to use GPC as a method for characterizing bio-oil stability.[23] The graph clearly depicts a shift to higher molecular weight as the oil undergoes accelerated aging tests.

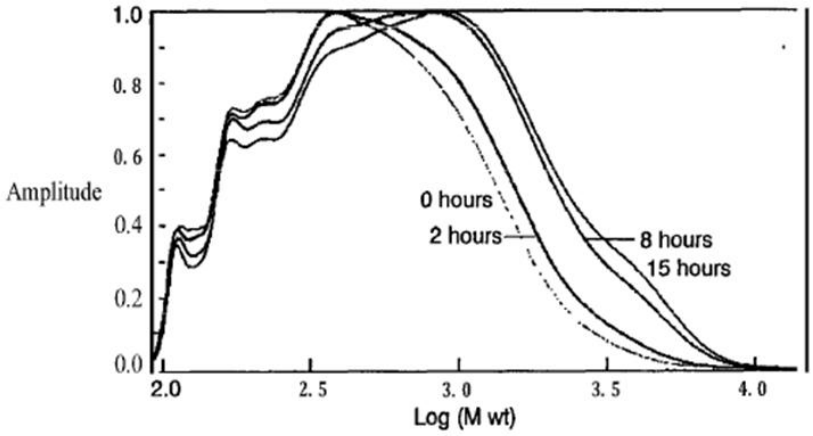

Figure 8: Molecular weight distribution of pyrolysis oil stored at 90℃ [23]

2.6 Filtration Approaches and their Application to Pyrolysis

In an effort to remove particulate matter from the pyrolysis vapors, multiple cyclones are commonly installed downstream of the reactor. The first cyclone is a high volume cyclone designed to separate out the majority of the larger particle char and can usually be designed to remove 90% of the solid matter. The second cyclone is a high efficiency cyclone and is designed to remove smaller diameter char particles with a similar 90% removal efficiency. In series the cyclone pair is very efficient, able to remove 99% of the char produced in the reactor.[24] However, any additional attempts at particulate matter removal with a cyclone yields diminishing returns and removal efficiency falls off drastically.[24] These cyclones are only able to efficiently remove particles larger than 10 μm, leaving the last 1% of char in this size range to be collected with bio-oil downstream. In order to increase the stability of the collected bio-oil, this remaining 1% must be removed.[25]

Several attempts have been made to more completely remove char particles from the high temperature vapor streams in situ. Most of these attempts make use of a barrier type filter. Scahill reported using a high temperature fiber filter to remove char fines without the aid of cyclones up stream.[19] He was able to repeatedly produce pyrolysis oils with alkali levels less than 10ppm and in one case, oil that could be combusted in a gas turbine engine. However, even with back-pulsing and filter regeneration, the process was unsteady and resulted in increasingly high pressure drop. The filter cake was sintered on to the barrier filter and extremely difficult to remove. This sintering of alkali onto the barrier filter surface is a common occurrence in the power generation and fuel production fields, and can take place at 75% of the mineral's absolute melting point.[26] A slight decrease in oil yield was also seen when compared to pyrolysis operation without the barrier filters and was coupled with a slight increase in water content. Most likely these phenomena are due to the secondary cracking reactions occurring on the surface of the filter. Figure 9 proposes an illustration of what may be happening on the barrier's surface while Figure 10 shows the results of a failed attempt at fine particle filtration with a barrier filter.

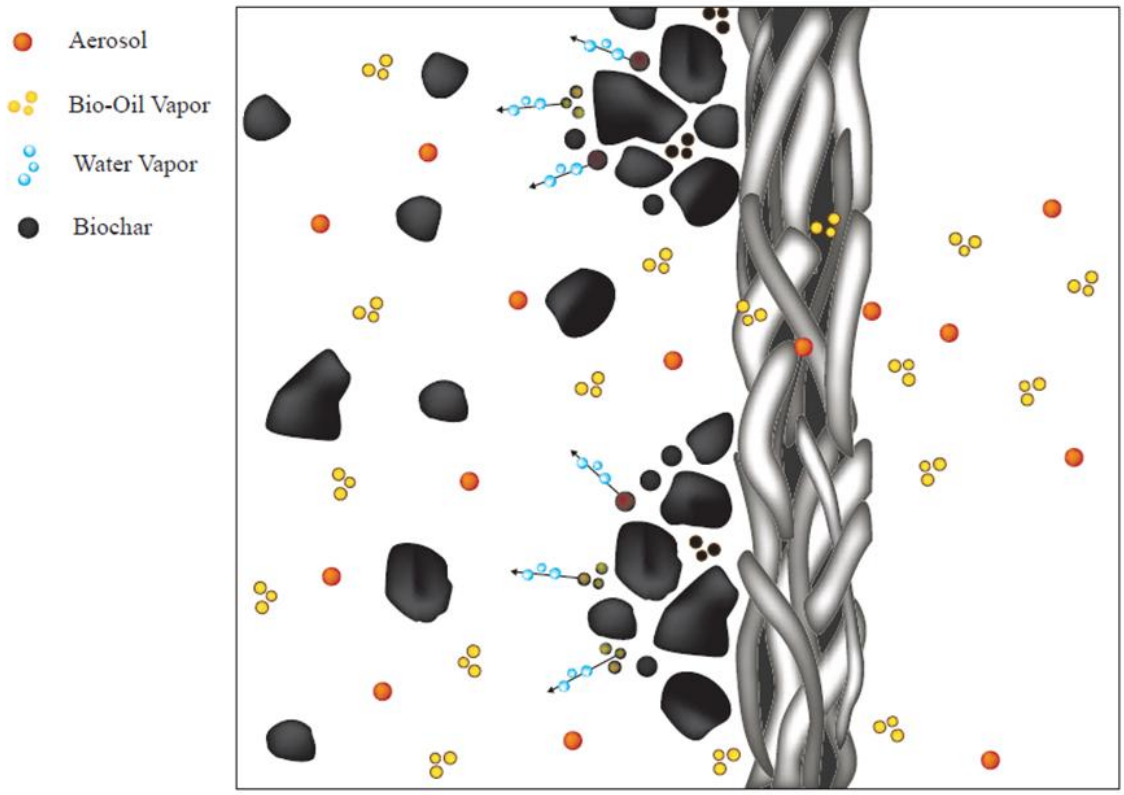

Figure 9: Cracking of Bio-oil Vapors and Aerosols on Barrier Filtration Surface; as char collects on a barrier surface, gas vapors are forced to pass through an ever thicker layer of porous particles. Char particles react catalytically with bio-oil vapors flowing past them to form lower molecular weight compounds, water, and more char.

The complex three phase system of vapor, solid particulate matter and liquid aerosol droplets undergo catalytic reaction, condensation and evaporation at the barrier filter surface. It is unknown whether the secondary reactions take place in the pores of the char or in the boundary layer around them. However, the result of these reactions is easily identified by the very fine, smooth, and sintered char layer that is left behind as evidence of their occurrence.

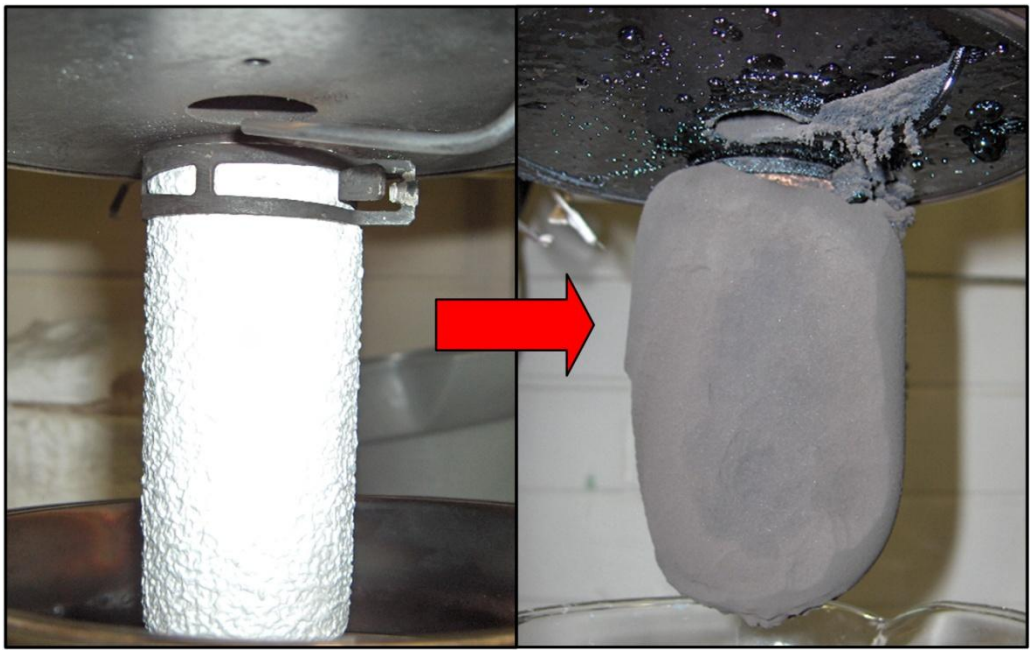

Figure 10: Barrier filter before and after exposure to vapors, aerosols, and particulate matter exiting a fast pyrolysis reactor. The buildup of particulate matter is mostly "secondary char" – formed when bio-oil vapors are cracked over char particles to form additional char.

Kang[27] demonstrated that particulate matter in bio-oil can be reduced using a combination of a cyclone and hot gas filter. The resulting pyrolysis oil had very low solids content at only 0.1 wt%. However, the water content of the oil was abnormally high in the 27-38 wt% range. This atypically high water content is most likely due to secondary reactions occurring on the surface of the ceramic barrier filters, similar to the phenomenon shown in Figure 10.

The University of Twente[28] also tested hot gas filtration in the freeboard of a fluid bed pyrolysis reactor. In this experiment, a 6 µm pore size mesh filter was placed at the top of a fluidized bed reactor within the expanded bed region in order to filter char as it was produced in the reactor. The filter was immersed in the fluidizing medium to take advantage

of the cleansing action of the bed particles and prevent filter cake buildup. The experimental setup allowed vapors to either pass through the filter or through a secondary exit in the reactor leading to a traditional cyclonic filtration train. This secondary exit allowed baseline oil to be collected that could be used for the basis of comparison. Figure 11 depicts both the location and a close-up of the filter used.

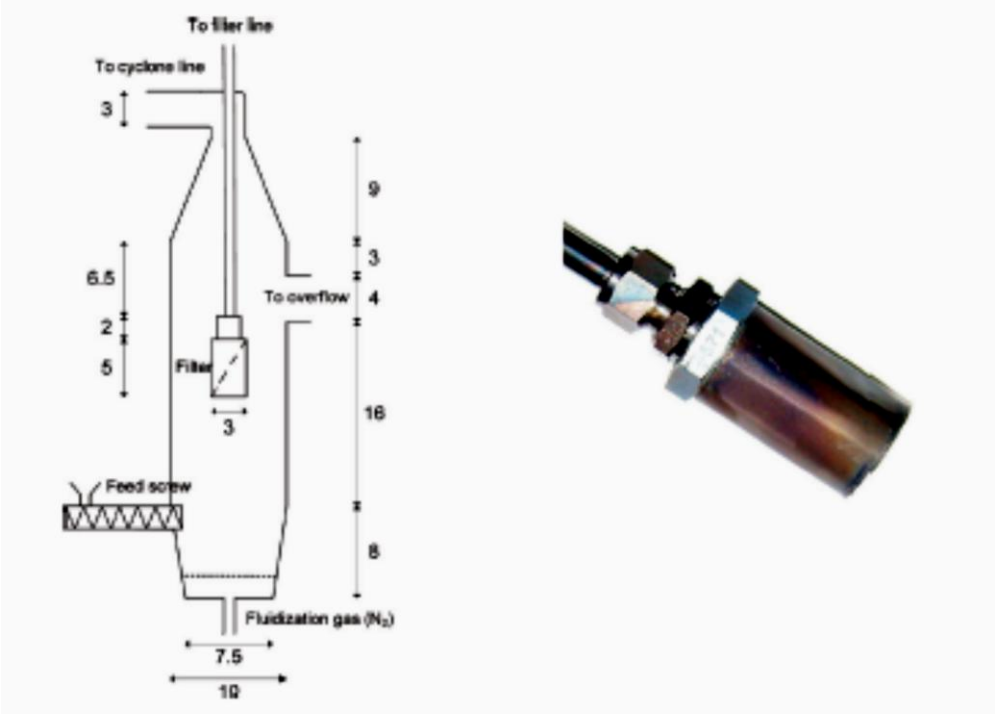

Figure 11: Continuous Bench Scale In Situ Barrier Filtration Schematic [28]

Results showed that the unfiltered bio-oil had a solids content of 0.11% by weight while the solids content of the filtered bio-oil was undetectable by gravimetric analysis. When the feedstock was doped with additional char, similar results were achieved as the unfiltered bio-oil solids increased to more than 1% weight and the filtered char remained undetectable. However, the experimental setup could encourage solids to preferentially pass

through the cyclonic removal train instead of the barrier filter. Any char that is removed from the barrier surface by the fluid bed material is re-entrained in the system and most likely ends up in the cyclone filtering train. Water content of the cyclonic oil was reported as 4-5% greater than that of the filtered oil; it was indicated that reactor geometry may preferentially feed water vapor from the biomass to cyclone filtration train rather than the barrier filter.

One previous study of the effectiveness of moving bed granule filters (MBGF) in removing particulate matter from pyrolysis vapors has been reported by researchers at the Industrial and Technology Research Institute (ITRI) of Taiwan.[29] They were able to realize a 10-fold decrease in bio-oil solids content when using a MBGF as opposed to traditional cyclone technology. As shown in Figure 12, the output of the 4.6kg/h fluidized bed reactor can be routed to either a pair of cyclones or to a MBGF for particle removal before proceeding to a common bio-oil collection train. The bio-oil produced by both filtering methods had similar density and pH levels. However, bio-oil yield inexplicably increased from 57% to 63%, when utilizing the MBGF. The solid content was also drastically different, decreasing from 0.95 to 0.10 weight percent for the cyclone and MBGF trains, respectively. Both methods operated with steady pressure drops at comparable absolute pressure levels.

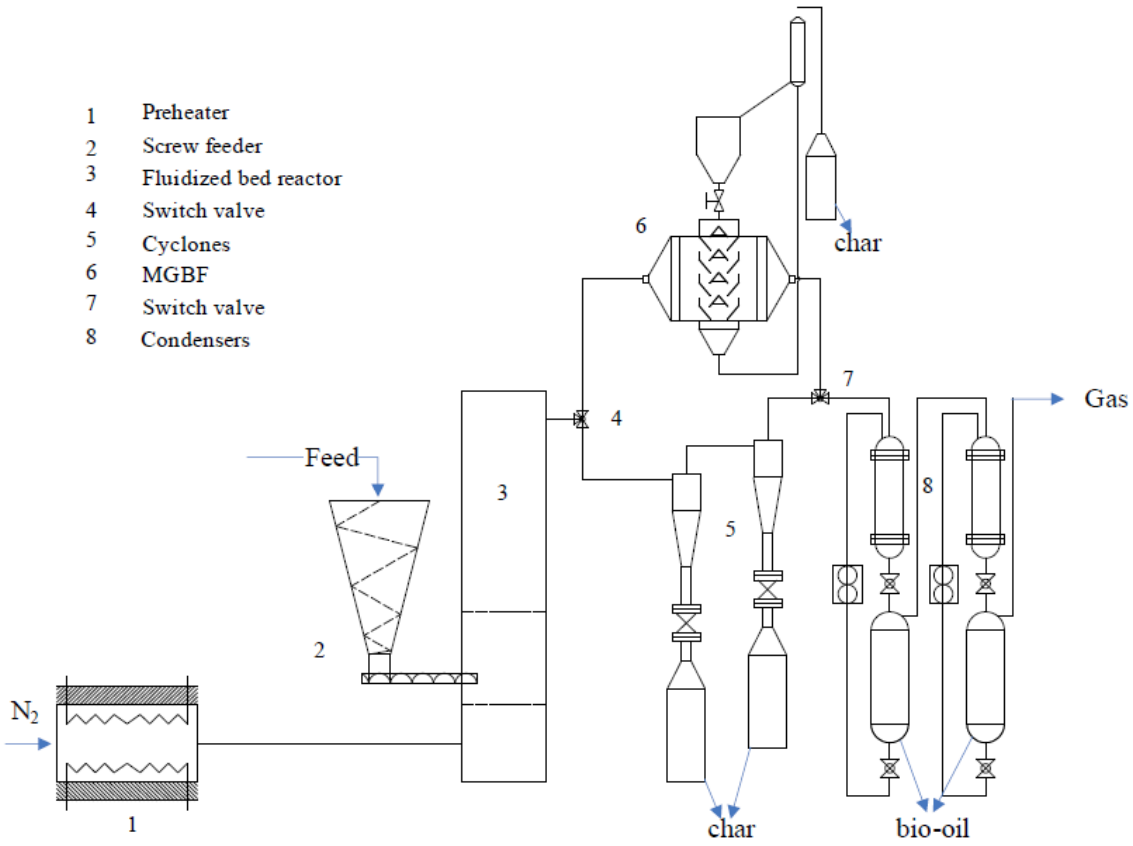

Figure 12: Bench Scale Moving Bed Granular Filter Schematic ITRI [29]

2.7 **Moving Bed Granule Filter**

Although the concept of granule bed filtration is not new, its application to pyrolysis gas streams is limited. Several successful filtration trails have been made on gasification processes, resulting in highly efficient particle removal in conjunction with precursory cyclonic filtration.[30, 31] Abatzoglou was able to achieve gasification collection efficiencies greater than 94% on 1-10μm particles while Nunez was able to note a significant reduction in the amount of large particulate matter using scanning electron microscope (SEM) images.

Similar to the moving bed granule filter utilized by Nunez, a counter-current MBGF has been designed for use with pyrolysis processes. Depicted in Figure 13, the moving bed filter uses a combination of both inertial impaction and the formation of a dust cake layer in order to filter particulate matter. The granule filtration media transverses the filter from top to bottom under the force of gravity, the throughput of which is metered with an auger at the base of the filter. The gas to be filtered enters the MBGF tangentially and spirals down the outside of the granule downcomer before encountering a set of straightening fins. The fins direct the gas into the granule/gas interface where granules spill out of the downcomer forming a conical expansion. This region is designated as the "Interfacial Region", and is where most of the dust collection occurs.[32-34] Here the collected particles form a dust cake similar to that found on the surface of a barrier filter. The dust cake formation is also responsible for high filtration efficiencies associated with the design.[35, 36] The constant flow of granule material facilitates the ability to minimize the dust residence time compared to traditional barrier filters while maintaining steady operating conditions by avoiding pressure drop increases.

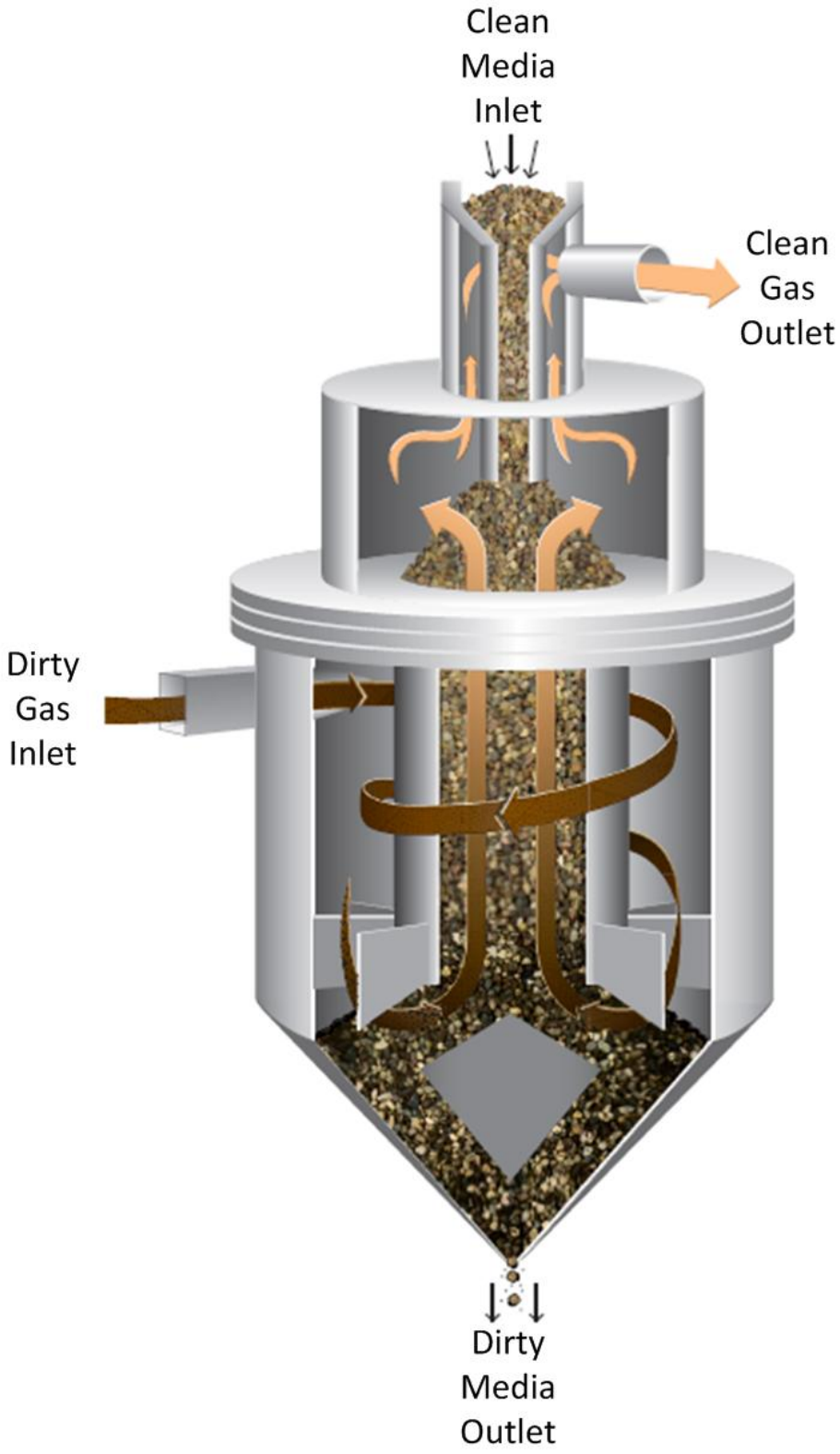

Figure 13: Moving Bed Granular Filter operating principle

Inertial impaction is the major collection mechanism causing particles with diameters greater than 1μm to deposit on the granule filtration media.[7] The conditions of these particle-particle interactions are best captured by utilizing the Stokes number, defined as follows:

Equation 1: Stokes Number

$$N_{St} = \frac{2\rho_p^2 \bar{U} a_p^2}{9\mu a_c}$$

where ρ_p is the particle density, U is the superficial velocity of the fluid, a_p is the particle radius, μ is the fluid viscosity and a_c is the granule radius. It follows that geometries promoting Stokes numbers less than one allow particles to stay within the streamlines of the fluid and not deposit on granule media. To the contrary, geometries which promote Stokes numbers greater than one result in inertial impaction and particle deposition on the granule surface.

In order to collect the char particulate matter and not the aerosols or bio-oil vapor, geometry of the filter and the granule size must be optimized. The Stokes number for char in the 1-10 μm must be greater than one while the Stokes number for aerosols ranging from 0.01 to 1 μm must be less than one to stay with the gas flow. Table 1 shows the calculated Stokes numbers for the current moving bed granule filter geometry regarding both char particulate matter and aerosols.

Table 1: Stokes Number for Specified MBGF Conditions

Particle Type	Interfacial	Downcomer
Aerosol	1.733×10^{-3}	6.738×10^{-4}
Particulate	1.905	0.741

In addition to maintaining proper Stokes numbers for particle filtration, minimizing char residence time will aid in the mitigation of secondary reactions that occur during filtration. By manipulating granule flow rate and tracking char movement through the filter in a series of cold flow tests, El Hedok was able to establish a minimum granule rate that maintains filtration efficiencies above 99%.[37] He was also able to propose an optimal operating condition that would prevent excessive char accumulation in the filter bed.

The filter design has been tested at elevated operating temperatures by Huisenga.[34] In these trials, model particulate matter was used in the form of fly ash gathered from a contemporary coal fired power plant and fed into the system using a powder feeder. Although only a moderate operating temperature could be reached, a distinct effect on filtration efficiency was evident. As shown in Figure 14, the test began with high filtration efficiency above 98% but as the operating temperature increased, filtration efficiency decreased to around 90%.

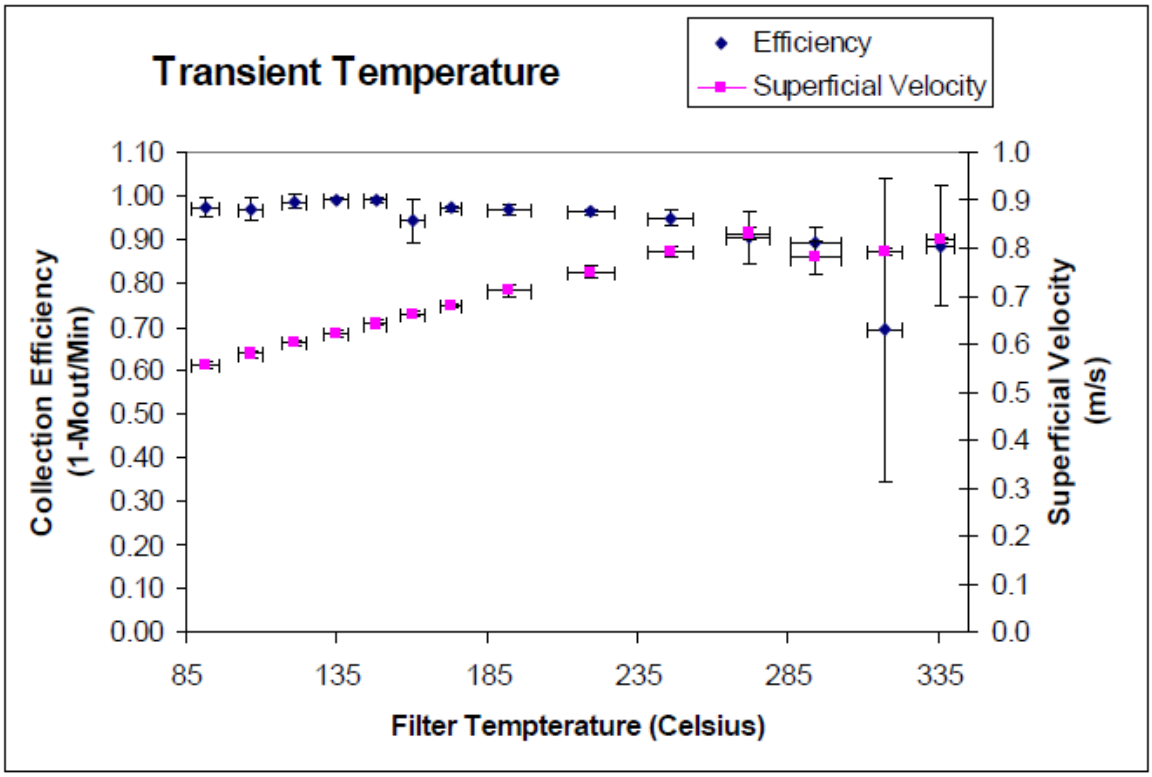

Figure 14: MBGF Transient Temperature Filtration Test [34]

2.8 Hypothesis

Hypothesis: Removal of particulate matter from bio-oil precursors through hot gas filtration will reduce percent solids in the resulting bio-oil and produce a product with increased stability.

Discussion of Hypothesis: Due to its high alkali and alkaline earth metal content, particulate matter in the high temperature bio-oil precursor stream provides a catalysis site for secondary reactions both during the transport phase and after the collection process. These reactions contribute to the instability of bio-oil, producing larger chain molecules shown as an increase viscosity and increased water content. By removing this particulate matter as soon as it exits the reactor, the secondary reactions will be minimized and therefore will result in a bio-oil with increased stability.

CHAPTER 3. EXPERIMENTAL METHOD

3.1 Experimental objective

The objective of this work is to qualify the ability of a high temperature moving bed granular filter to remove char particulate matter in-situ pyrolysis operating conditions. To this end, two metrics will be used: (1) the collection efficiency of the filter obtained through a quantitative mass balance and (2) the resulting stability of bio-oil produced with the filter in stream as demonstrated through an accelerated aging study and subsequent oil analysis.

3.2 Pyrolyzer Process Development Unit (PDU) Experimental Apparatus

A moving bed granular filter was constructed for installation into the 8 kg/h (1/4 ton per day) pyrolyzer PDU located at the BioCentury Research Farm (BCRF) in Boone, Iowa. This PDU is capable of continuous operation and utilizes a proprietary condensing train technology to collect bio-oil in 5 stage fractions. The unit's design and construction is detailed heavily by Sherwood-Pollard and was successfully demonstrated to fractionate bio-oil from three different biomass feed stocks.[14]

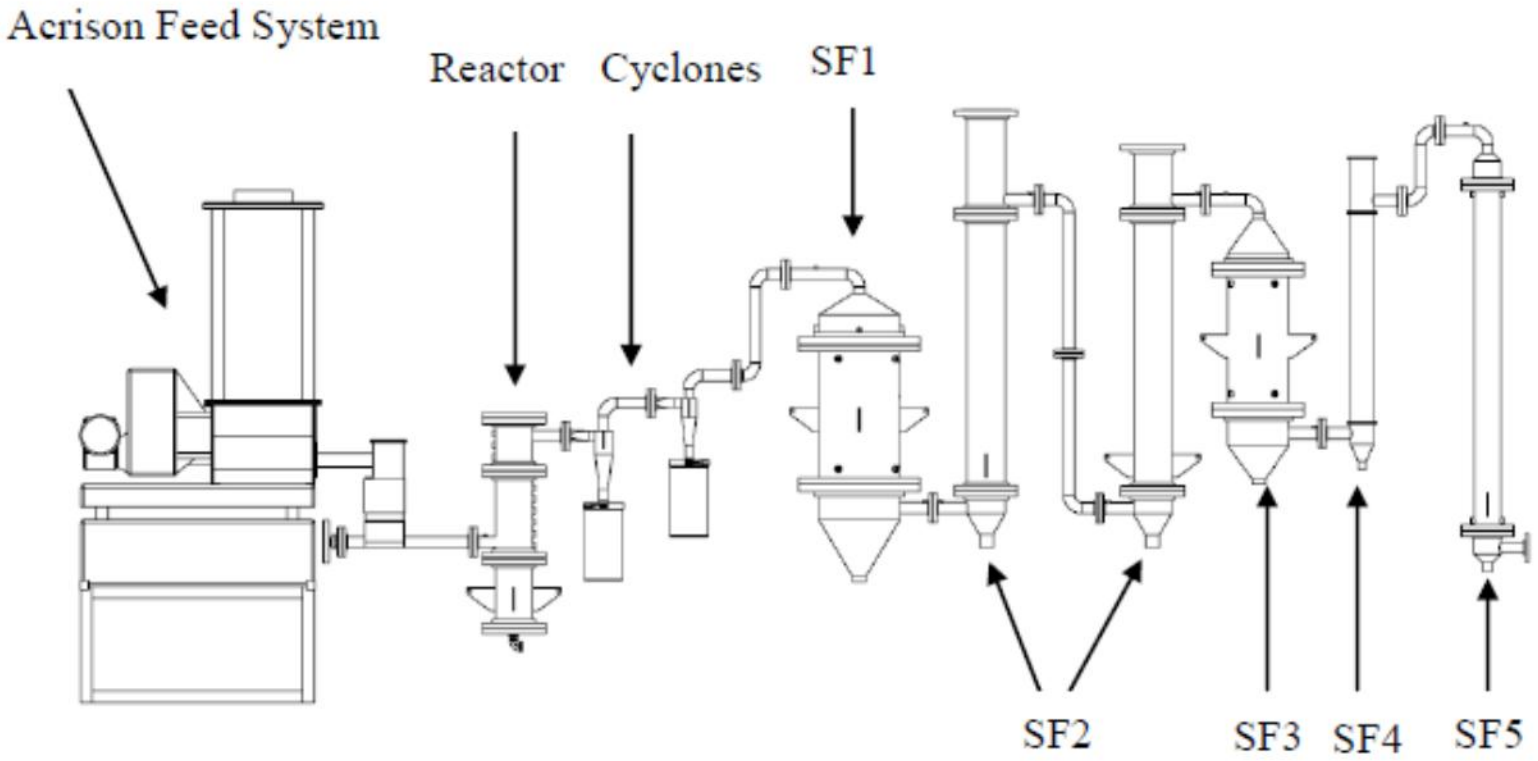

Figure 15: Pyrolyzer PDU System Schematic [14]

Biomass is conveyed into the system with a lock-hopper system using two feed hoppers and a pair of Wey® knife gate valves. The system uses a dual auger system consisting of a metering auger and an injection auger. The metering auger is part of an Acrison® weigh and loss feed system which is able to continually monitor mass flow. The metering auger drops the feed onto the constantly spinning injection auger transporting it into the bed.

The reactor is a bubbling fluidized bed, the 15.4 cm diameter vessel constructed of stainless steel. Bed material is pre-sized silica sand with a particle size distribution centered at 600 µm. Nitrogen is used as the fluidization medium and is preheated in three stages before entering the reactor plenum and passing through a distributor plate.

The solids removal system normally employed in the PDU consists of two cyclones in series; a high volume cyclone followed by a high efficiency cyclone. Both cyclones were constructed with rectangular inlets which enter the body tangentially without a scrolling section. The minimum diameter at which the cyclone is designed to filter particles with 50% efficiency (d_{50}) are 11 µm and 2 µm, respectively, for the high volume and high efficiency cyclones.[14]

The collection system is a combination of temperature controlled condensers and electrostatic precipitators totaling five stages as depicted in Figure 15. The first stage is a condenser operating at relatively high temperature followed by a pair of ESPs that are collectively designated as the second stage due to their identical operating conditions. The third stage is a condenser followed by an additional ESP collecting stage fraction 4. The final stage is a condensing unit. Finally, a glass wool filter is in line after the collection system to capture any remaining vapors or aerosols. Non-condensable gases are sampled

after the glass wool filter using a slipstream before the excess gas is combusted in a natural gas burner and discharged to the atmosphere.

3.3 Moving Bed Granule Filter Experimental Apparatus

3.3.1 Introduction

The moving bed filter consists of three subsystems: the granule feeder, the MBGF, and the granule collection system. The feeder purges granules of oxygen and brings them up to operating temperature and pressure before feeding them into the top of the MBGF. The MBGF brings the granular media into contact with the dirty gas stream such that there is a counter-flow of gas and media. . The collection system controls the flow of media through the MBGF, cools the collected material, and disengages it from the pressurized environment. Each of these systems and their design is described in detail below.

3.3.2 Feed System

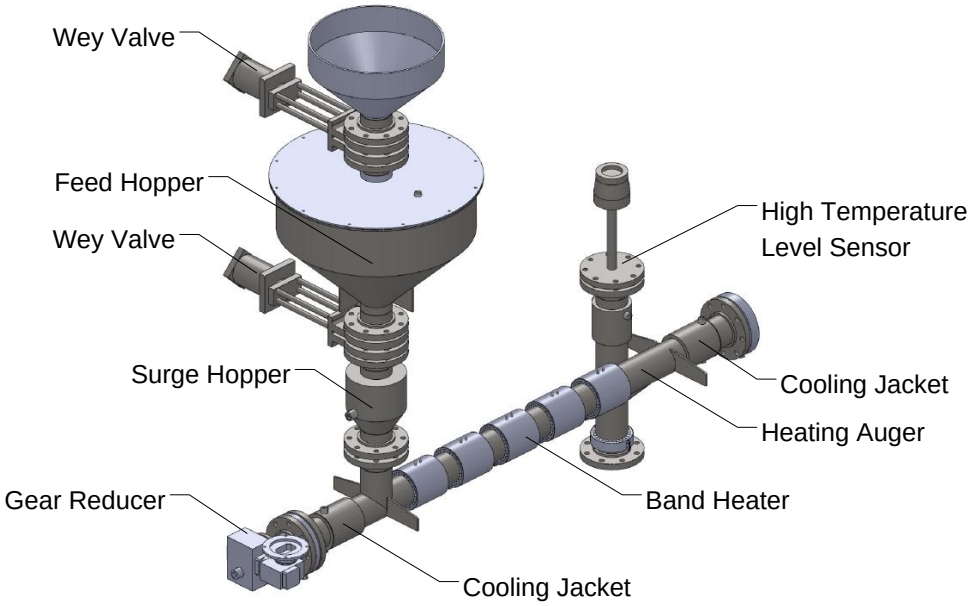

Figure 16: Feed System Schematic

The feeder shown in Figure 16 consists of three parts: the feed hopper, the surge hopper, and the heating auger. The feed hopper is isolated on both its inlet and outlet by a gas tight, 10.2 cm Wey® model NA1 knife gate valve designed specifically for cutting off flow of granular material. By isolating the feed hopper from the rest of the filter, media can be transferred into the system and the void volume purged of air using a lock hopper style feeding process. First the bottom gate is closed to isolate the system, followed by opening the top gate. The new media is transferred into the hopper and purged using a small flow of nitrogen introduced at the bottom of the chamber. The upper gate is closed followed by the opening of the lower gate, completing the filling cycle. The feed hopper is capable of housing 200 kg of filtration media, allowing an operating range of 8 - 25 hours of run time.

The feed hopper has been outfitted with a pair of Allen-Bradley® type 875C capacitive proximity sensors: a high level sensor to indicate the hopper is full and a low level sensor to warn material is running empty. The sensors are tunable to a range of dielectric constants and are adept at detecting granular material. The feed hopper empties into the surge hopper, which provides a small reservoir of filtration media from which the system can draw while new media is loaded into the feed hopper. The surge hopper holds around 10 kg of material and is similarly outfitted with a low level proximity sensor designed to indicate when media is running low.

The final component of the feeder is the heating auger depicted in Figure 17. The heating auger utilizes a custom designed adjustable paddle auger fabricated using 304 stainless steel. The paddle design promotes increased mixing over standard auger design by allowing higher rotational speed with less linear material conveyance. In order to verify the soundness of the design, a series of auger test rigs were constructed to establish baseline data for material movement and heat transfer to the filter media. The results of these tests are detailed in APPENDIX A and APPENDIX B respectfully.

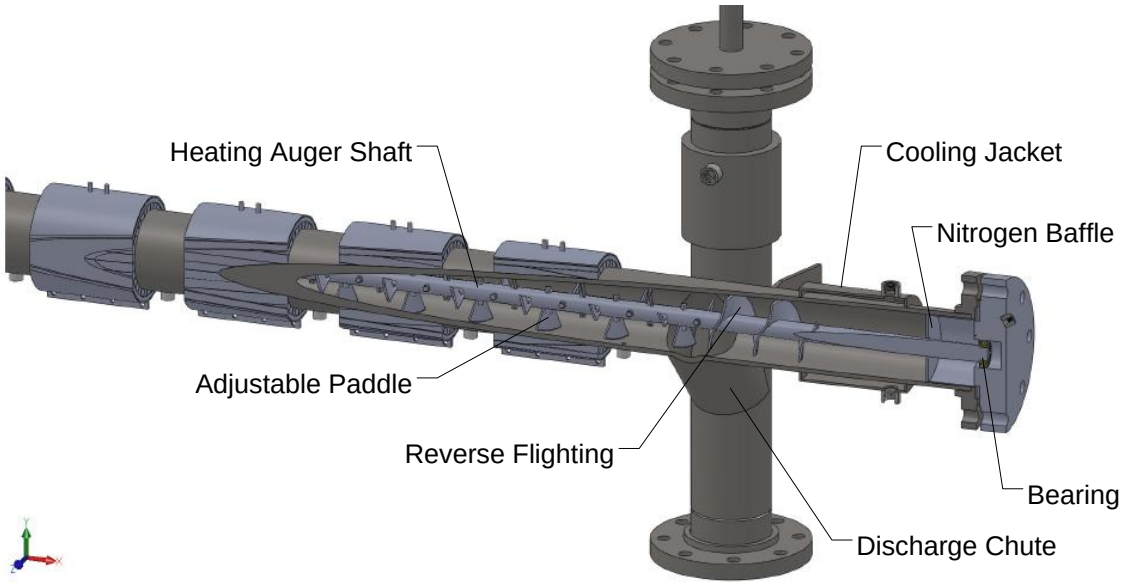

Figure 17: Heating Auger Cut-Away View

The heating auger also features a custom bearing end-cap that houses two seals and one bearing from SKF. The inner seal is a high pressure unit designed to retain the slight pressure experienced by the system. The bearing is a deep groove ball bearing unit designed to resist both axial and radial loading of the auger shaft and is pressed into the housing. The outer seal is designed to retain grease in the bearing housing cavity and protect the bearing from external dirt contamination. The bearing is axially located on the shaft against a shoulder and retained using a snap ring. On the opposite side of the heating auger, a second bearing is pressed on to the end of the auger shaft and located against a shoulder. This bearing floats in a bottomed cavity allowing it to hold pressure with no shaft seals while still allowing axial expansion caused by the high temperature in the heating section of the auger. Both bearing end-caps use standard flange bolt patterns and spiral wound gaskets. They also feature extruded bosses that serve to radially locate the end-caps holding concentricity with

the housing and aligning the bearings. Each end of the auger retains a removable purge baffle which directs cooling nitrogen around the auger shaft in order to keep heat out of the bearing. The housing is cooled on both ends with a baffled jacket that forces cooling water to flow down the bottom of the jacket, through a gap in the baffles, and back across the top of the jacket before exiting. Detailed drawings of the entire MBGF can be found in **Error! eference source not found.**.

The housing is heated using five, independently controlled ceramic band heaters manufactured by Chromalox®. The 240 volt, 2000 watt resistance heaters are equally spaced and provide 26 watts/in^2. The system is insulated with calcium silicate and Kaowool™ blanket insulation. Details on the design and sizing of the heating auger are provided in APPENDIX D.

3.3.3 Moving Bed Granule Filter

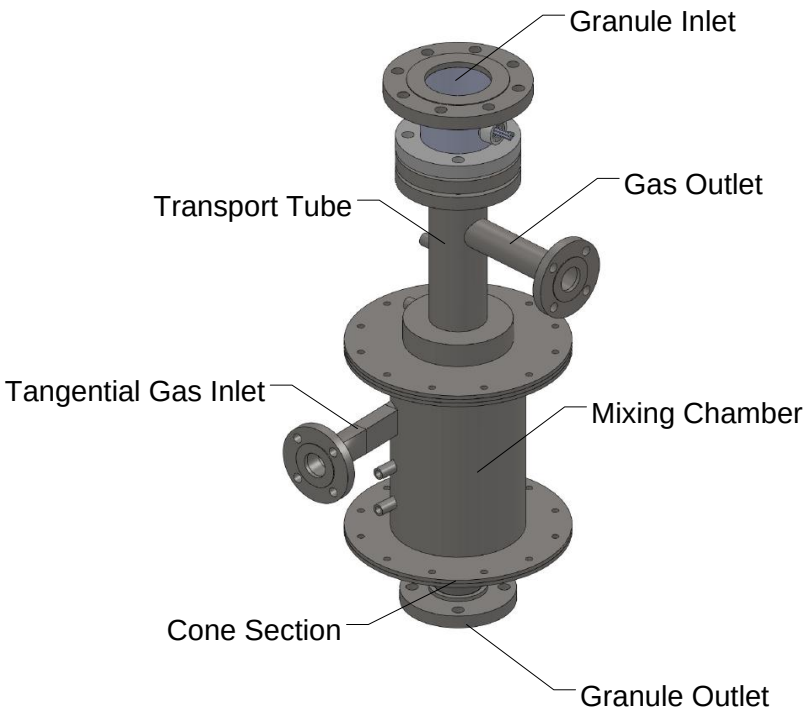

Figure 18: Moving Bed Granular Filter

The operational theory of the MBGF filter is detailed in section 2.7. Gas streams are directed to and from the filter using high temperature stainless steel model SS-T67MF24-A220 ball valves utilizing Grafoil® seats manufactured by Swagelok®. The three valves are oriented such that the PDU can be operated with or without operation of the MBGF. A normally open (NO) valve is located between high efficiency cyclone and condenser one of the PDU. A normally closed (NC) valve is also in line on both the entrance and the exit of the filter. Heat control to the filter is provided in four independent zones consisting of the

gas inlet, gas outlet, transport tube, and mixing chamber. The system is insulated with solid calcium silicate and Kaowool™ blanket insulation.

3.3.4 Collection System

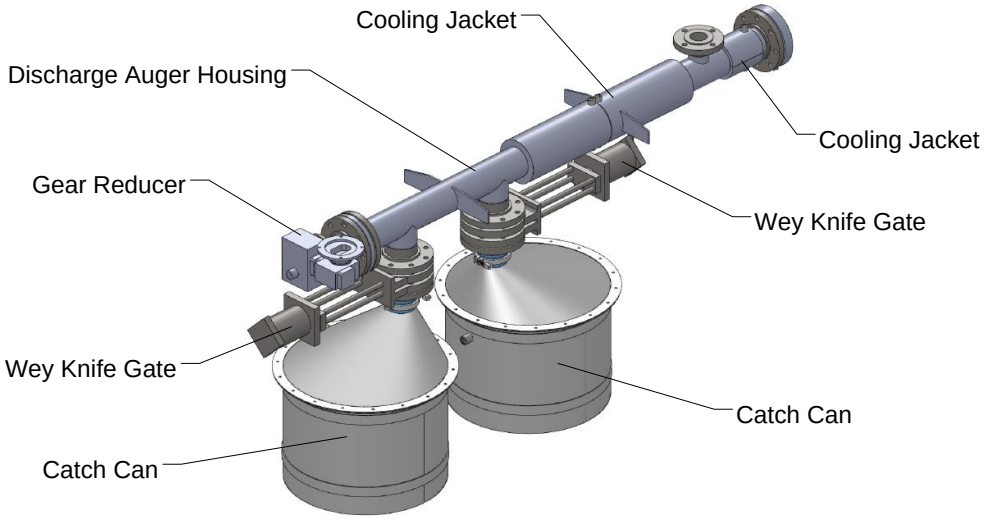

Figure 19: Collection System Schematic

The granule collection system consists of three parts, a discharge auger and two catch cans. The discharge auger serves as both a means of conveying spent filter material out of the system as well as metering the flow of granules though the moving bed filter. The discharge auger first sends the material through a water jacketed cooling section designed to lower the granule temperature to one suitable for operation of the Wey® knife gate valves. Once cooled, the spent media can pass through one of two discharge outlets; each leading to a knife gate and catch can combination. This orientation allows for continuous operation by closing one gas tight valve in order to empty its catch can while material is conveyed into the

other can. The discharge auger features identical bearing design, bearing end-caps, and water jacketed cooling section as the heating auger for part interchangeability.

The catch-cans are of identical construction and feature an internal copper coil designed to provide additional cooling to spent media. The connection type is a quick connect stainless steel sanitary fitting which allows for easy installation and removal with a wing-nut clamp. Both cans utilize a high level sensor, identical to that used in the feed system, as well as a temperature indicating thermocouple.

3.3.5 Data Acquisition and Control

The control system used to operate the pyrolyzer PDU was expanded for use with the MBGF. This system is based on Rockwell Automation control software utilizing an HMI (human machine interface), a historian data server, power cabinet, and I/O (input/output) racks. Its design and operation are described in detail by Sherwood-Pollard.[14]

A similar power cabinet and I/O rack were built to operate the MBGF. The cabinets were linked to the PDU system processor and primary rack using Allen Bradley® Stratix Ethernet switches and subsequent patch cables. The main control cabinet contains the main buss fusing, circuit breakers, solid state relay (SSR) systems to control heating zones, and variable frequency drives (VFD) to control motor speeds. The I/O cabinet houses the Ethernet switch, 24VDC power supply, and the cards used to take data and supply operation signals. These two systems were isolated in separate cabinets in order to avoid signal contamination in the low voltage instrumentation. Detailed drawings of the control boxes can be found in **Error! Reference source not found.**.

All pressure readings were acquired using Dwyer® Series 677 differential pressure transducers with varying calibration ranges of either 0-10" or 0-25" water column. The transducers have a 0.4% full scale accuracy, resulting in pressure readings with at least ±0.05" water column accuracy. The system is detailed elsewhere by El Hedok.[37]

All temperature measurements are taken using Omega Engineering® brand type K thermocouples which feature chromel-alumel elements, capable of reading temperatures between -200 and +1350°C. A custom Omega Engineering® Profile Probe that takes multiple readings along its length was used to provide temperature readings that correspond to pressure reading locations throughout the bed of the MBGF.

In order to maintain steady flow through the filter between the heating and discharge augers, the granule level on top of the filter is monitored using a high temperature level sensor. This RF Admittance level transmitter is an Ametek Drexelbrook® model RCT 12 which features high temperature materials rated up to 816°C.

During system operation, the granule rate is set using the discharge auger. As granule media is removed from the system, a desired level is maintained on top of the filter using the RF level transmitter and adjusting the speed of the heating auger accordingly. The heating cycles of the band heaters are then regulated using a specified discharge temperature at the auger's exit and the varying load based on granule throughput.

3.4 Test Methods

3.4.1 Granular Filtration Media Preparation

Before testing can begin, the filtration media must be prepared for testing. The media used in this study is 3 mm x 1.5 mm river rock obtained from Red Flint Sand and Gravel® and was chosen due to its filtration ability demonstrated by previous research.[37] Due to the large amount of dust and sand mixed in with the media as received, both a sieving operation and a dust removal process was necessary in order to eliminate dust contamination through elutriation during filtration. A large tray sieve shaker was modified with a series of air nozzles to both remove the sand through a 0.058 mm screen and blow the dust away in one process. Once cleaned and conditioned for size, the media was stored in a warm, dry space to eliminate any moisture concerns prior to use during filtration tests.

3.4.2 Test Procedure

A moving bed granular filter test begins by bring the pyrolyzer PDU to steady state operation. The desired testing conditions are selected through the human machine interface bringing the reactor, heat traced transfer lines, condensers and ESPs up to temperature. The pyrolyzer operating condition were held constant through all tests, holding the fluidized bed temperature at 500°C and 183 standard liters per minute nitrogen fluidizing gas. The first condenser wall temperature was operated at 85°C. The first and second ESPs were operated to maintain gas temperatures of 125°C and set points of 35,000 volts and 30,000 volts respectively. Condenser 2 wall temperatures were maintained at 65°C resulting in gas temperatures at 75°C. ESP 3 is not temperature controlled but well insulated resulting in semi isothermal gas temperatures of 75°C and a voltage potential of 15,000 volts. The last

condenser is cooled to 18°C as provided by the chilled water system available from the building supply. Red Oak was used as the biomass feedstock in all tests and was fed at a rate of 6kg/h.

The MBGF operating temperatures were also held constant during all experiments. Gas transfer lines into and out of the filter were maintained at 450°C as limited by the operational temperatures of the ball valves. The filter bed itself was maintained at 475°C using a combination of the discharge temperature of granules exiting the heating auger, the transport pipe temperature, and the mixing chamber temperature. These set points varied based on the desired granule flow rate through the system. The granules exiting the filter were cooled to a temperature less than 40°C before being discharged to the catch cans.

The night before an experimental trial, the micro gas chromatograph (GC) used for non-condensable gas analysis undergoes bake-out to clear the columns of any contamination. Condensers 1, 2, and 3 are also turned on and allowed to come to steady-state operating temperatures overnight. When initiating a run, air used as fluidizing gas is set to the desired flow rate and the injection auger is turned on. The fluidizing gas preheaters and bed clamshell heaters are cycled on to heat up to operating temperature. All heat tapes for the cyclones and gas transfer lines for both the PDU and the MBGF are turned on and allowed to reach steady-state. Once the fluidized bed temperature reaches 350°C, nitrogen replaces air as the fluidizing gas.

At this point the micro-GC is taken out of bake-out and calibration verification is run to ensure accuracy of the micro-GC. The sample line first passes through a set of impingers consisting of 3 glass wool filters and a desiccant canister residing in an ice bath. This procedure allows the non-condensable gas sample line to remain vapor and moisture free

before passing into the GC. A few samples are taken at this point to verify that there are no leaks in the sampling system as indicated by high oxygen content in the reading.

Biomass feeding begins when all components have reached their operating conditions starting with a set point of 2kg/h. At this point the non-condensable gas combustor is turned on along with the ESPs which are brought to their operational set points. The reactor is allowed to come to steady- state temperatures before increasing the feed rate to 4 kg/h. The process is repeated once more before achieving the desired 6 kg/h set point. The system is considered to be in steady-state operation once all temperatures and pressures have stabilized and the first condenser is producing a steady stream of bio-oil. At this point helium tracer gas is added to the fluidizing gas at a rate of 2.5 standard liters per minute and steady-state gas analysis data is taken for one hour. Depending on the test, collection bottles may be switched to collect steady-state pyrolysis oil for baseline.

Once biomass feeding has begun, the process to bring the MBGF to steady-state continues. The resistance heaters on the MBGF heating auger are turned on and the discharge auger set to a low granule flow rate to start warming up the system. The discharge auger is only open to the catch can farthest away from the filter during warm-up and initial filtration. When the pyrolyzer reaches steady-state, the granule flow rate through the filter is increased to the desired set point. Once steady-state pyrolyzer gas data has been collected and the filter bed has reached steady-state temperature, the ball valves are actuated to route pyrolysis gas through the filter and into condenser 1. First the NC valve at the filter exit is opened, followed by the NC valve at the filter inlet before finally closing the NO valve between the cyclone and condenser 1. This process avoids any extreme pressure build up in the system due to restricted gas paths.

Pressure drop across the various sections of the filter bed are monitored in order to determine when steady-state operation has been reached as indicated by flat pressure trends. The time period required to reach these conditions is dependent on the granule flow rate selected as is the ultimate pressure drops reached in each section. The filter is then run for a period of time required to fill the discharge auger with steady-state spent filtration media. After this time period, the granule catch can closest to the filter is opened to collect steady-state spent media. The bio-oil collection bottles are switched out for new steady-state filtration bottles on the pyrolyzer, along with changing the char catches and starting non-condensable gas analysis. The collection period for filtered oil was two hours before proceeding to shut down.

Experiments were terminated by stopping the biomass feeder, closing the close granule catch, opening the far catch, shutting off the heating auger, and allowing the filter bed to empty. The bio-oil collection bottles and char catches were changed back out and the micro-GC turned off. The heaters on the fluid bed and MBGF were shut down. The NO valve between the cyclone and condenser 1 is opened allowing nitrogen to pass through both systems in order to cool down the components. Nitrogen flow is stopped only after the reactor temperature has decreased below 300°C to prevent the auto-ignition of material remaining in the bed.

3.4.3 Design of Experiments

In order to effectively evaluate the performance of the filter, a set of experiments was chosen that would be able to balance the ability to prove or disprove the hypothesis yet be

achievable from an operational standpoint. Therefore, only one independent variable was selected, granule feed rate through the filter, while holding all other variables constant. The order of the tests was selected at random to minimize any random error that could occur between tests.

Table 2: Test Plan

Test #	Granule Feed Rate	Filter Bed Temp	Reactor Temp
1-20101210 GR24	24 kg/hour	475°C	500°C
1-20110120 GR8	8 kg/hour	475°C	500°C
1-20110124 GR16	16 kg/hour	475°C	500°C
1-20220127 GR16	16 kg/hour	475°C	500°C
1-20110202 GR8	8 kg/hour	475°C	500°C
1-20110204 GR24	24 kg/hour	475°C	500°C
1-20110221 GR16	16 kg/hour	475°C	500°C

The midrange feed rate of 16 kg/h was replicated twice while both the high and low range feed rates had a single replication for a total of 7 tests. The overall range of flow rates tested was based on the success of previous cold-flow testing [37] and the ability of the system to heat the granule media to the desired operating temperature of 475°C.

3.4.4 Bio-Oil, Char, and Gas Analysis

MASS BALANCE

Mass balances were estimate from five measurements on the system. The overall biomass fed into the reactor was recorded based on weight measurements from the Acrison® scale at the beginning and end of the steady-state collection period. The mass of the char collected in both the high volume and high efficiency cyclones was also weighed and recorded. In order to evaluate how much char is collected by the moving bed filter, it must

first be separated from the filtration media. This was accomplished using an 20.3 cm diameter Ro-Tap sieve shaker and an 850 μm mesh screen. The shaker operates using a circular rotation to agitate the material while a weighted arm on top of the machine taps the top of the screen stack. The gravel is retained in the top screen, allowing the char to fall below into the bottom catch pan for subsequent mass determination. Each bio-oil collection bottle is pre-weighed before the test and the mass is again recorded after collection. Non-condensable gas content is measured using the micro-GC previously described. A known mass flow of inert helium tracer gas is passed through the pyrolysis system during steady-state operation to act as an internal standard. The volume percentages of all gasses are measured by the micro-GC and using the known mass flow of the helium tracer, the corresponding masses of the non-condensable gases can be calculated.

TGA

A large scale NAVAS Instruments TGA-1000 thermo gravimetric analysis (TGA) instrument was used to analyze the char separated from the filtration media for ash content. The instrument heats the sample to 105C and holds temperature in a nitrogen environment until the sample reaches constant weight, removing any moisture present. The TGA then heats the sample to 950C in nitrogen and holds temperature for 6 minutes, monitoring sample weight to quantify the volatile content. The sample is cooled under nitrogen to 750C before air is introduced to combust any carbon content present in the sample until constant weight is achieved. Any sample remaining is considered ash content and will include any filtration rock that was missed by the sieving separation process as well as ash content from biomass derived primary char collected in the filtration process.

MICRO-GC

The gas chromatograph used to analyze the non-condensable gases produced in the pyrolysis process is a Varian model CP4900. It utilizes three columns for identifying compounds. The first column is a Molsieve 5A and is used to identify helium, hydrogen, oxygen, nitrogen, methane and carbon monoxide. The second column is a Pora Plot U and is used to identify carbon dioxide, ethane, ethylene and acetylene. The final column is an Al2O3/KCl PLOT and is suitable for separating propane.

SOLIDS CONTENT

The solids content of the bio-oil is measured using a gravimetric technique. A five gram sample of oil is collected in a 100 mL centrifuge tube and dissolved in 75 mL of methanol. A quantitative grade number 50, 185 mm diameter filter paper is baked in a muffle furnace for 15 minutes at 105°C to remove any moisture before being pre-weighed. The paper is folded into a cone and placed into a funnel which is held under vacuum. The dissolved bio-oil sample is poured though the filter allowing the liquid portion to pass but any particles larger than the 2 µm pore size is retained. The paper is once again baked in the oven at 105°C for 30 minutes before a final mass is taken. The percent solids content is calculated according to the following formula:

Equation 2: Percent Solids Calculation

$$\%\, Solids = \frac{final\ filter\ paper\ mass - initial\ filter\ paper\ mass}{bio - oil\ sample\ mass} * (100\%)$$

Each solids measurement is performed in triplicate to ensure accuracy of results. The samples were also collected immediately after pyrolysis in order to reduce aging effects.

This approach also helps ensure uniformity in sampling by avoiding the settling time associated with storage before samples for analysis can be collected.

WATER INSOLUBLE CONTENT

Bio-oil consists of an aqueous fraction consisting mostly of small, carbohydrate-derived molecules and an insoluble fraction derived from lignin in the biomass, sometimes called "pyrolytic lignin." [38] The water insoluble fraction consists mostly of phenolic oligomers.

Analysis of the water insoluble content of bio-oil begins by the addition of hot water to a 2 gram sample of bio-oil followed by mixing and sonication in a vortex tube. The resulting solution is filtered through a size 42 filter paper which has been baked and pre-weighed. The percent water insoluble can then be calculated using the initial sample mass, tube mass, filter mass, and the following formula:

$$\%\ Insolubles = \frac{\sum \text{mass: filter paper, tube and lid (with solubles)} - \sum \text{mass: filter paper, tube and lid (empty)}}{\text{sample mass}} (100\%)$$

MOISTURE CONTENT

The moisture content of the bio-oil is determined using a Karl Fischer Moisture Titrator MKS-500 and by adhering to ASTM E203 standard. The instrument works on the basic principle of volumetric titration in which a known reactant of unknown concentration, or the water in bio-oil, is reacted with a reagent of known concentration. A well-mixed sample of bio-oil is obtained in a syringe and a 20-30 µg sample of the bio-oil is injected into the instrument were it is dissolved in a solvent, Hydranal Working Medium K. The resulting analyte solution is then titrated with the reagent, Hydranal Composite 5K, at a known

volumetric addition until no water remains in the solution. The syringe mass before and after the injection is entered into the instrument and the resulting moisture content is output as a percentage.

GPC

As a result of the stage fractionation process, the bio-oil produced from the PDU varies greatly in viscosity. Traditionally, viscosity is measured using a kinematic technique which is highly dependent on the temperature of the sample during measurement. It is therefore difficult to draw uniform comparisons across the various fractions using this technique due to the high viscosity of bio-oil at room temperature. This study employs an analytical technique based on an observation by Sadula and Brown[39] that bio-oil viscosity correlates with molecular weight as determined by gel permeation chromatography (GPC).

GPC techniques involve suspending a small amount of sample, around 0.02 g, in 10 mL of solvent, tetrahydrofuran (THF), and passing the resulting sample through a set of columns. The columns contain porous beads which are permeable based on the molecular weight of the sample passing through them. The permeating molecules are then routed to a pair of detectors, one refractive index (RI) and one ultra violet visible (UV-vis) detector, which determine molecular weight. Since all fractions can be analyzed using the same technique under the same operating conditions, it is much easier to obtain consistent results and draw comparisons across aged samples when compared to traditional techniques. In this study, each GPC sample was analyzed in triplicate to assure accuracy in results.

ACCELERATED AGING

A procedure for accelerated aging has been established by the Department of Energy (DOE) to simulate the effect of long term storage on bio-oil.[40] In this study, accelerated aging was used on oil collected after moving bed filtration in order to observe the resulting effect on bio-oil molecular weight using the GPC analysis described above. Three 10 gr samples of each fraction were obtained directly from the reactor. These three sets of samples were placed in an oven maintained at 90°C. After 8 hours, the first set of samples was removed followed by the second set after 16 hours and the final set after 24 hours. The GPC samples from fractions 1 and 2 were prepared immediately after removal from the oven to avoid aging resulting from reheating the high viscosity fractions in order to obtain samples for GPC analysis. The 8, 16 and 24 hour heating periods correspond to bio-oil stored at room temperature for 3, 8, and 12 months respectively.[41]

SEM

An FEI Quanta 250 FEG scanning electron microscope (SEM) was used to examine the structure of char obtained from various points in the pyrolysis and filtration process. This instrument has the ability to operate in both a high vacuum atmosphere with an Everhardt Thronley secondary electron detector (SED) or in a low vacuum atmosphere using a Large Field Detector (LFD). The instrument is also equipped with a Back Scatter Electron Detector (BSED) used to differentiate between different atomic weights that may be present in the sample. In this study, a variety of magnifications were used to gain an understanding of particle size distribution and particle morphology of the various samples.

SEM with EDS

A Hitachi S-2460N SEM coupled with an Oxford Instruments Isis energy dispersive x-ray spectroscopy (EDS or EDX) detector was used to examine the metal content of collected char samples. The SEM has the ability to run in both high and low vacuum operating regimes in order obtain the best sample magnification without charging interference. The x-ray analyzer is equipped with quantitative analysis software capable of point detection down to a few tenths of a percent. Multiple points were examined within each sample to confirm uniformity of results. The analyzer is also capable of performing x-ray mapping which gives a qualitative distribution of elements present in the sample. Samples used in this analysis were the same samples used for the above SEM analysis.

ICP-AES

A Spectro Ciros CCD inductively coupled plasma atomic emission spectrometry (ICP-AES) was used to quantify the trace metal content of biomass and char samples obtained throughout the process. For this analysis, the samples were prepared with method 3051A. A 500 mg sample of each of the substances was digested with 10 ml nitric acid at 175 ºC for 10 min in a microwave digester. Following digestion, the solution was diluted with 100 ml of DI water, mixed, filtered and subjected to ICP-AES analysis. The resulting ppm concentrations were then adjusted by a dilution factor obtained from actual sample and dilution water masses.

CHAPTER 4. RESULTS AND DISCUSSION

4.1 MBGF Operational Parameters

During filtration, the MBGF was able to operate at steady temperatures and with stable pressure drops under the proper operating conditions. In addition to the tests outlined in Table 2, several other attempts were made to determine the operating limitations of the MBGF. An attempt was made to operate the MBGF at a lower filtration bed temperature of 350°C and a granular rate of 8 kg/h. Upon routing the pyrolysis gas through the filter, two trends were noticeable. The filtration bed temperature began to rise, assumed to be the result of the addition of the 500°C pyrolysis gas. This assumption was later confirmed through a simple energy balance. Secondly, the pressure drop across the interface of the filter began to climb and became excessive after 20 minutes of operation, necessitating rerouting the pyrolysis stream away from the filter and back through the condensing train. It was determined that the pressure drop was due to clogging of the bed, halting granule movement and shutdown of the heating auger due to insufficient level change on top of the MBGF. An additional attempt at these set-points again resulted in clogging and gas rerouting.

An additional attempt at low filtration bed temperature operation was made immediately following the test failure at 8 kg/h. The granular rate was increased to 16 kg/h, the filtration bed was allowed to clear, and the operational temperature was returned to 350°C. The pyrolysis gas stream was routed through the filter and the filter bed once again rose to 400°C in 30 minutes without the aid of the guard heaters around the bed. The pressure drop across the bed steadily increased and did not allow the system to reach steady-state operating conditions, resulting in the termination of the test. Upon disassembly of the

MBGF, evidence of bio-oil vapor condensation was evident throughout the downcomer and transport pipe indicating the temperature was too low for sustained operation.

The MBGF was also operated at a lower granular rate of 6 kg/h and a 500°C bed temperature in order to determine the minimal operating flow rate of the filter. Upon routing the pyrolysis gas through the MBGF, pressure drops across the filter began to rise. After several minutes of operation, the heating auger stopped feeding fresh granules to the filter indicating granule flow had stopped. A light rapping on the discharge auger resumed granule flow, returned pressure drops to acceptable levels and the test was continued. After several iterations of this cycle, each resulting in rapping the discharge auger to resume flow, the 6 kg/h operating condition was determined to be unstable.

Under the steady operating conditions outlined in Table 2, the MBGF was able to operate at steady temperatures. It was necessary to continually reduce the amount of heating to the filter body once pyrolysis gas was introduced to the system. This was most likely due to the combination of the hot gas running through the filter providing additional energy and the exothermic reactions transforming pyrolysis vapors into secondary char and water at the filter interfacial region.

The operational pressure drop was also very constant throughout the tests outlined in the test plan. Pressure drop was consistent and repeatable between tests at the same granular flow rate. As shown in Figure 20, the trend of increased pressured drop with decreased granular flow rate is clearly visible. This behavior is explained by increased char loading in the filter bed resulting in decreased void space between filtration media as granular flow rate decreases. The anomaly at the beginning of the GR8 test was due to additional char loading resulting from the closure of the cyclone catches in the transition to steady-state product

collection. The slower granular flow rate takes additional time to discharge char from the filtration region resulting in a pressure spike across the filter until the char is cleared by the granular movement.

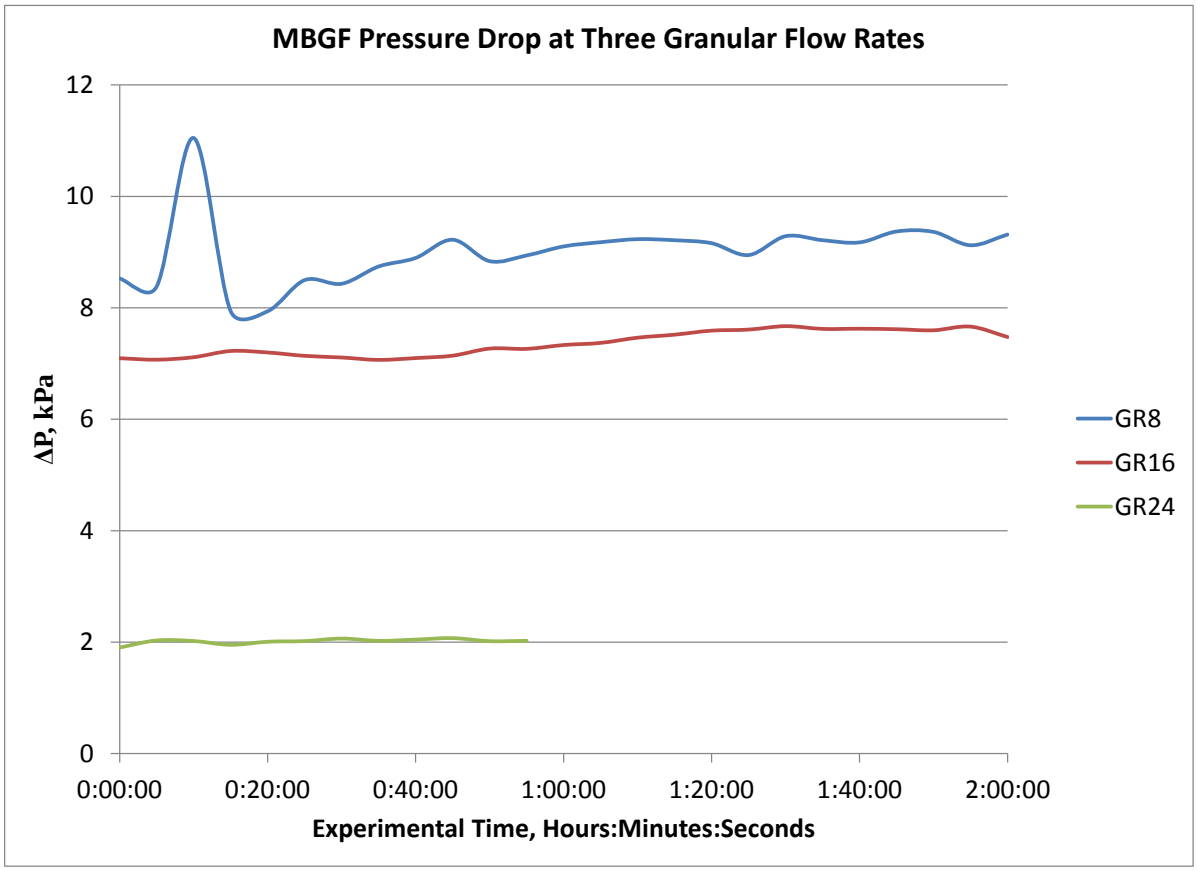

Figure 20: Pressure Drops Across MBGF during Three Granular Flow Rates

4.2 Mass Balance

The mass balance data for each test is displayed in Table 3 and Table 5. These tables include information pertaining to bio-oil, char and non-condensable gas yields along with average yields for each. The results were statistically compared using two sided Student's t-tests between each operating condition in order to identify any significant differences. The alpha value was set at 0.05 meaning a p-value less than alpha would reject the null

hypothesis and a statistically significant difference could be detected between the operating conditions. Analysis giving p-values greater than 0.05 would fail to reject the null hypothesis, indicating that a statistically significant difference was not detectable.

No significant differences could be detected in the yields of cyclone char, filter char and non-condensable gases between any of the filter operating conditions or the PDU baseline yield data. The same is true regarding stage fraction three, four and five mass yields. However, statistically different yields could be detected in stage fractions one and two in three cases: PDU baseline vs. GR8, PDU baseline vs. GR16, GR16 vs. GR24 operating conditions. Results indicate that using the moving bed filter as part of the pyrolysis cleanup process results in statistically significantly less heavy-end oil yield than in its absence. This analysis cannot however, detect where the reduced oil yield is transferred by way of statistically higher yields elsewhere in the process. It is interesting to note that a statistically significant difference can only be detected between two granule flow rates tested; the 24kg/h tests yielded more heavy-end bio-oil than the 16kg/h tests. Inferences about this relationship are difficult to make due to the lack of other significant relationships between set points.

Mass balances over 100% collection are theorized to be the result of elutriation of silica sand from the fluidized bed reactor that is subsequently removed in the cyclone collectors and counted toward char yields. Given sufficient time, the fluidization level of the reactor stabilizes and elutriation stops. The reactor bed was refilled to the same level after each test in order to maintain identical operating parameters.

Table 3: Mass Balance Table (Wet Basis)

Test #	Cyclone Char	Filter Char	SF1	SF2	SF3	SF4	SF5	NCG	Closure
1-20101026 PDU SS	24.5%	N/A	12.5%	19.3%	4.3%	1.4%	25.6%	18.3%	105.9%
1-20110210 PDU SS	16.4%	N/A	12.3%	21.3%	3.6%	1.8%	26.8%	22.8%	104.9%
Average	20.5%	N/A	12.4%	20.3%	3.9%	1.6%	26.2%	20.5%	105.4%
1-20110120 GR8	13.5%	0.9%	10.9%	18.5%	3.8%	1.7%	23.0%	20.9%	93.3%
1-20110202 GR8	13.8%	0.7%	10.6%	17.7%	3.8%	1.8%	26.3%	22.2%	96.8%
Average	13.7%	0.8%	10.8%	18.1%	3.8%	1.8%	24.7%	21.5%	95.1%
1-20110124 GR16	15.6%	1.2%	10.7%	17.0%	3.7%	1.8%	27.1%	22.5%	99.7%
1-20220127 GR16	13.1%	1.1%	9.2%	16.9%	3.9%	1.7%	25.4%	21.5%	92.9%
1-20110221 GR16	13.3%	1.0%	9.3%	16.4%	3.3%	1.6%	28.4%	24.0%	96.3%
Average	14.0%	1.1%	9.7%	16.7%	3.6%	1.7%	27.0%	22.7%	96.3%
1-20101210 GR24	17.6%	0.8%	11.7%	19.2%	3.3%	1.6%	28.2%	22.6%	105.0%
1-20110204 GR24	14.4%	1.9%	10.8%	17.0%	3.2%	1.6%	26.7%	24.2%	99.8%
Average	16.0%	1.3%	11.2%	18.1%	3.3%	1.6%	27.5%	23.4%	102.4%

Additional analysis was performed on the filter char obtained from sieve separating the filter media. Samples from one test at each granular flow rate were analyzed in triplicate for ash content using a large scale TGA. The results can be found in Table 4. The ash content is as high as 98% of filter separated char, which would include both dust derived from filtration media and ash from biomass derived primary char removed during filtration. A general trend of increased ash content with increased granular throughput is apparent, but still case dependent. This is likely due to the increased exposure to larger amounts of filtration media at higher flow rates. However, it still attests to the inconsistent grinding occurring in the MBGF during operation. In each case, a larger mass percentage was attributed to volatile content then to the amount of fixed carbon. This may be an indication of the collection of bio-oil vapors on the media during MBGF testing.

Table 4: MBGF Separated Char Ash Content

Sample	Moisture	Volatiles	Fixed C	Ash	Dry Volatiles	Dry Fixed C	Dry Ash
1-20110120 GR8	0.8%	14.7%	16.2%	68.3%	14.9%	16.3%	68.8%
1-20110120 GR8	0.8%	15.3%	16.9%	67.0%	15.4%	17.0%	67.6%
1-20110120 GR8	0.8%	15.1%	17.6%	66.4%	15.2%	17.8%	67.0%
Average	**0.8%**	**15.0%**	**16.9%**	**67.3%**	**15.2%**	**17.0%**	**67.8%**
1-20110202 GR8	0.6%	12.9%	8.7%	77.8%	12.9%	8.8%	78.3%
1-20110202 GR8	0.6%	14.1%	10.9%	74.3%	14.2%	11.0%	74.8%
1-20110202 GR8	0.7%	15.0%	12.3%	72.0%	15.1%	12.4%	72.5%
Average	**0.6%**	**14.0%**	**10.7%**	**74.7%**	**14.1%**	**10.7%**	**75.2%**
1-20110124 GR16	0.6%	12.7%	6.9%	79.8%	12.7%	6.9%	80.3%
1-20110124 GR16	0.6%	12.1%	6.3%	81.0%	12.2%	6.3%	81.5%
1-20110124 GR16	0.6%	12.6%	6.3%	80.5%	12.7%	6.3%	81.0%
Average	**0.6%**	**12.5%**	**6.5%**	**80.4%**	**12.5%**	**6.5%**	**80.9%**
1-20110127 GR16	0.6%	11.7%	10.2%	77.6%	11.7%	10.3%	78.0%
1-20110127 GR16	0.6%	12.2%	9.4%	77.8%	12.3%	9.5%	78.2%
1-20110127 GR16	0.5%	11.4%	9.5%	78.6%	11.5%	9.5%	79.0%
Average	**0.5%**	**11.8%**	**9.7%**	**78.0%**	**12.0%**	**9.9%**	**78.1%**
1-20110221 GR16	0.2%	7.6%	1.4%	90.9%	7.6%	1.4%	91.0%
1-20110221 GR16	0.2%	7.6%	1.1%	91.1%	7.6%	1.1%	91.3%
1-20110221 GR16	0.2%	7.7%	1.4%	90.8%	7.7%	1.4%	90.9%
Average	**0.2%**	**7.6%**	**1.3%**	**90.9%**	**7.6%**	**1.3%**	**91.1%**
1-20101210 GR24	0.1%	1.6%	0.0%	98.2%	1.6%	0.1%	98.4%
1-20101210 GR24	0.2%	1.6%	0.0%	98.3%	1.6%	0.0%	98.4%
1-20101210 GR24	0.1%	1.8%	-0.1%	98.2%	1.8%	-0.1%	98.3%
Average	**0.1%**	**1.7%**	**0.0%**	**98.2%**	**1.6%**	**0.0%**	**98.4%**
1-20110204 GR24	0.4%	10.1%	3.0%	86.5%	10.1%	3.0%	86.9%
1-20110204 GR24	0.5%	9.5%	3.4%	86.6%	9.6%	3.5%	87.0%
1-20110204 GR24	0.5%	10.3%	4.6%	84.6%	10.3%	4.7%	85.0%
Average	**0.5%**	**10.0%**	**3.7%**	**85.9%**	**10.0%**	**3.7%**	**86.3%**

A second yield analysis was conducted concentrating specifically on bio-oil yield. Table 5 contains bio-oil stage fraction yields as a fraction of total bio-oil produced. When analyzing these results in a similar fashion, a single statistically significant relationship emerged between PDU baseline data and filtration at 16kg/h media flow rate. A statistically significantly smaller amount of oil is produced in both stage fractions one and two during filtration than during baseline PDU tests. A statistically significant increase in stage fraction

five yields was also detected between filtration and baseline data. Once again, this phenomenon is a good indication that bio-oil vapor is cracking upon passage through the filter cake present with moving bed filtration, resulting in a decrease in yield of higher molecular weight compounds and an increase in yield of water. Inferences about cracking reactions are difficult to make on mass yield data alone and will be discussed further in section 4.4 pertaining to bio-oil moisture content.

Table 5: Bio-Oil Stage Fraction Mass Balance Normalized by Whole Bio-oil Yield

Test #	SF1	SF2	SF3	SF4	SF5
1-20101026 PDU SS	19.8%	30.6%	6.8%	2.2%	40.5%
1-20110210 PDU SS	18.7%	32.3%	5.4%	2.7%	40.8%
Average	19.3%	31.5%	6.1%	2.5%	40.7%
1-20110120 GR8	18.9%	31.8%	6.6%	3.0%	39.7%
1-20110202 GR8	17.6%	29.4%	6.2%	2.9%	43.8%
Average	18.2%	30.6%	6.4%	3.0%	41.7%
1-20110124 GR16	17.8%	28.1%	6.2%	3.0%	44.9%
1-20220127 GR16	16.1%	29.6%	6.9%	3.0%	44.4%
1-20110221 GR16	15.7%	27.8%	5.6%	2.7%	48.2%
Average	16.5%	28.5%	6.2%	2.9%	45.9%
1-20101210 GR24	18.2%	30.0%	5.2%	2.5%	44.1%
1-20110204 GR24	18.2%	28.6%	5.4%	2.6%	45.1%
Average	18.2%	29.3%	5.3%	2.6%	44.6%

4.3 Qualitative Properties of Products

A distinct difference in filtration media was observed after undergoing pyrolysis filtration. As shown in Figure 21, the material is darkened by the presence of char but remained free-flowing. The loose char was easily removed from the media using a sieve shaker, leaving a light coating of very fine char dust on the media surface. The freshly

discharged spent media also featured a unique aroma similar to that of smoky pyrolysis liquids.

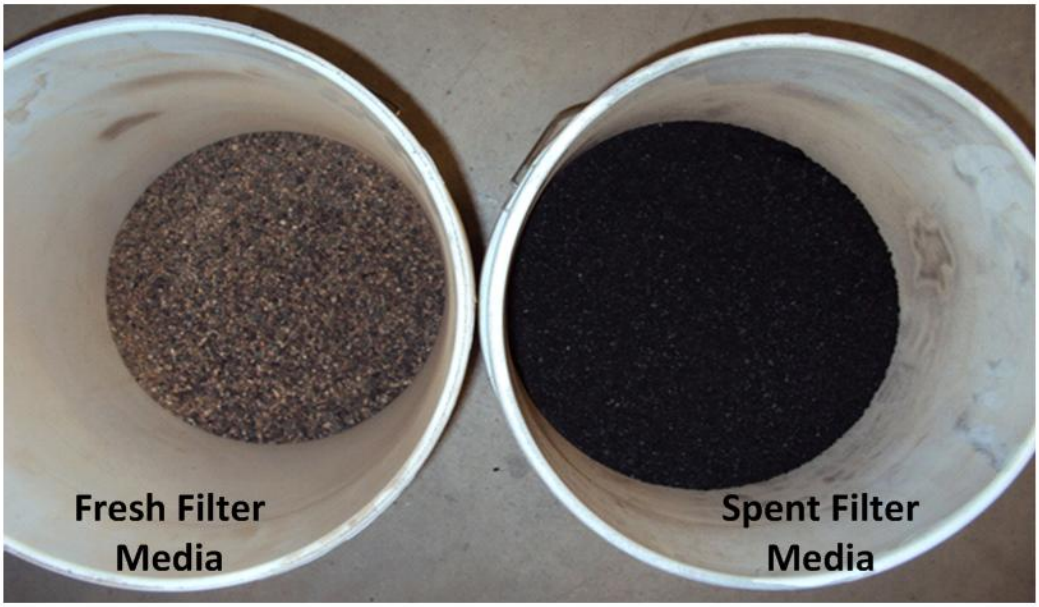

Figure 21: Fresh and Spent Filtration Media

The pyrolysis liquids themselves were similar to those produced previously,[14] with decreasing viscosity from stage fraction 1 to 5 and the first two fractions being solid at room temperature. No visual distinction was immediately evident between bio-oils produced with and without the MBGF. However, the instability of both baseline and MBGF SF5 fractions was apparent within a few days. Upon collection, these fractions were light pink in color, free of sediment, and acidic in smell. After several days under refrigerated storage, the liquid became dark red in color with black deposits precipitating on the bottom and walls of the storage containers.

4.4 Bio-oil Moisture Content

Bio-oil moisture content measurement is crucial in determining whether or not secondary reactions have occurred during the filtration process. By comparing baseline PDU moisture content to those resulting from moving bed granular filtration, additional insight into the occurrence of these reactions is provided.

The moisture content measurement was replicated between 4-6 times for each fraction in order to obtain statistically significant results. The following model was used to estimate the mean and standard error of the collected data:

Equation 3: Statistic Model

$$y_{ijk} = \mu_k + r_i + \varepsilon_{ijk}$$

where y_{ijk} is equal to the mean of analysis j, on run i, under condition k. The actual mean of the sample is defined as μ_k. The error between replicated runs is designated as r_i while the analytical error between individual measurements is designated as ε_{ijk}; the combination of these two error sources is defined as the standard error. The statistical analysis was conducted using SAS JMP™ software. The upper and lower 95% confidence intervals are then calculated according to the following pair of equations:

Equation 4: 95% Confidence Limits

$$Upper\ 95\%\ Limit = \mu_k + (Standard\ Error)(1.96)$$

$$Lower\ 95\%\ Limit = \mu_k - (Standard\ Error)(1.96)$$

The resulting means and confidence limits shown as error bars are displayed in Figure 22. A general trend of increasing moisture content with decreasing condenser temperatures is

apparent and is consistent with previous results.[14] However, no significant conclusions are apparent when comparing the baseline PDU moisture contents with that of any of the MBGF operating conditions.

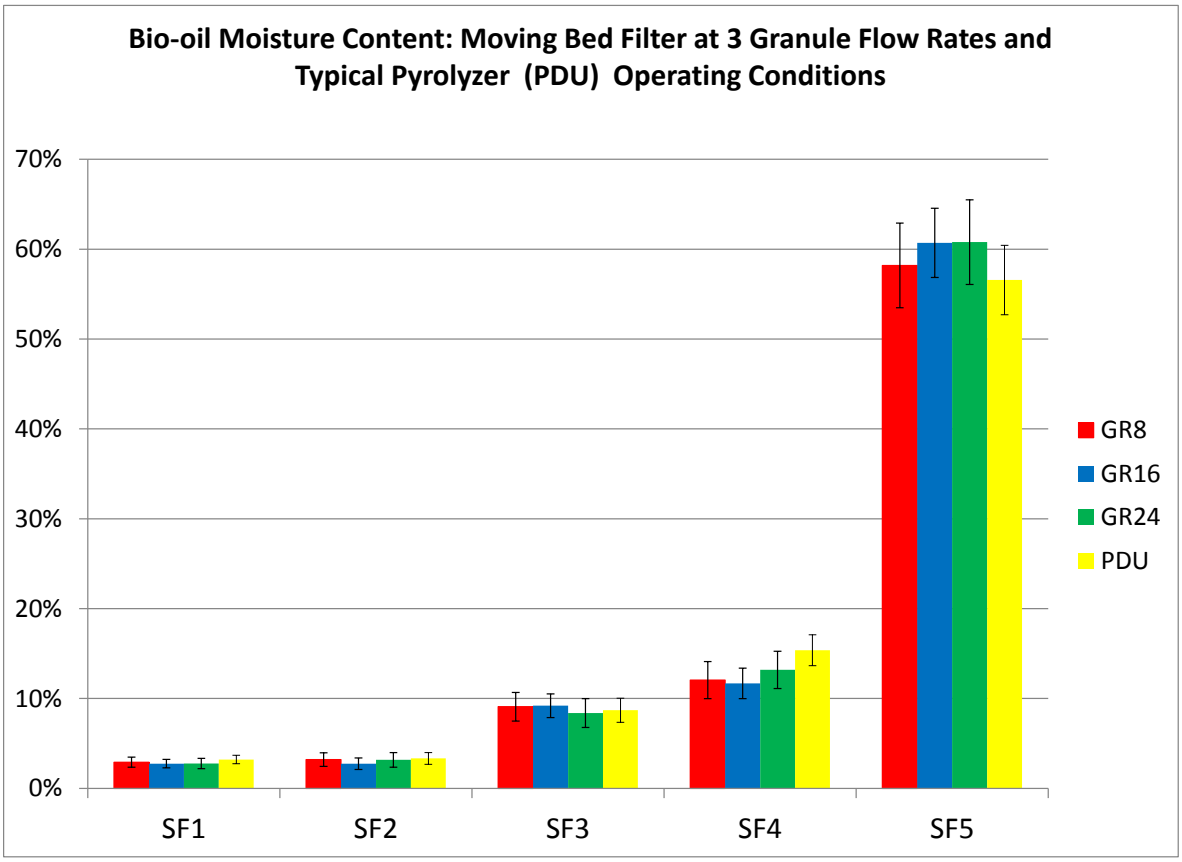

Figure 22: Bio-oil Moisture Content

The moisture content was mass averaged by fraction yield and compared on a whole oil basis using Equation 5. Figure 23 shows that the PDU baseline case produced bio-oil with a moisture content typically found with whole oil.[1] However, when modifying the process with the MBGF in situ, the resulting bio-oil moisture content increased by 2-5% depending on filter operating conditions. The majority of these increases took place in SF5 with the moisture content of the first four fractions remaining relatively constant.

Equation 5: Mass Averaged Moisture Content

$$\left(\frac{\%moisture}{100\%}\right)\left(\frac{g\ H_2O}{g\ \ Bio-oil}\right)\left(\frac{g\ Bio-oil}{g\ Whole\ Bio-oil}\right)$$

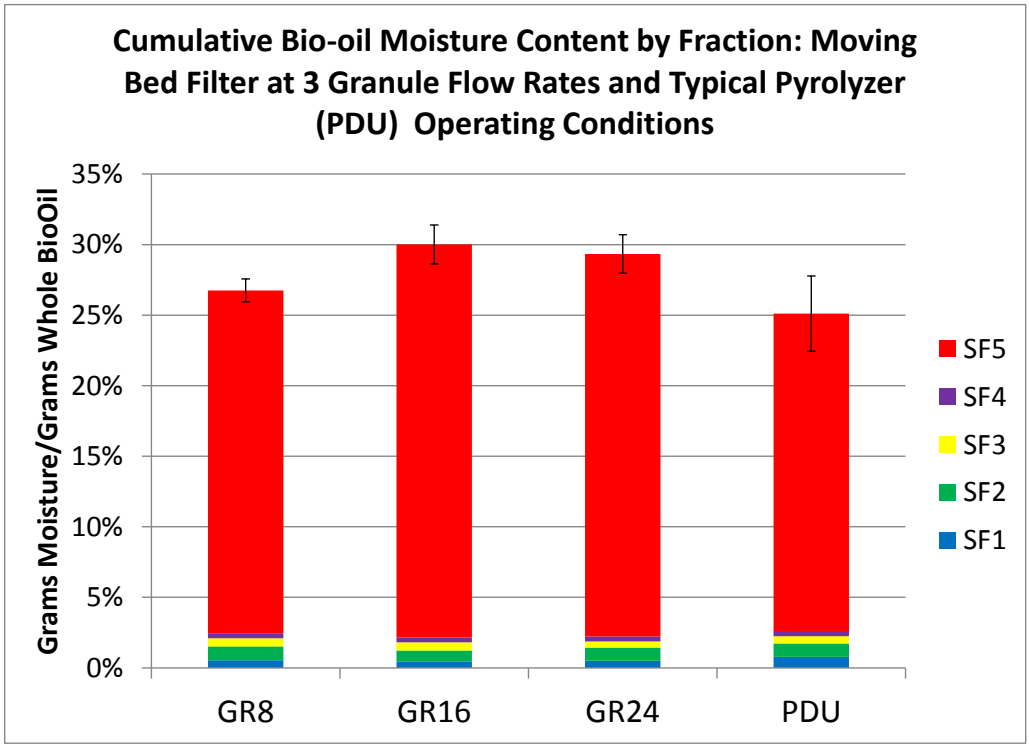

Figure 23: Mass Averaged Bio-oil Moisture Content

The increase in moisture content of MBGF derived bio-oils over baseline samples is a clear indication of the occurrence of secondary reactions within the filter. The 8 kg/h test resulted in a smaller increase in moisture content than either of higher flow rate tests. This operating condition is characterized by longer residence time of collected char in the filter due to the slower granule throughput. Both the 16 and 24 kg/h tests resulted in similar increases in water content over baseline oil. These operating conditions are characterized by shorter char residence time in the filter but with increased surface area for cracking to take place.

4.5 Bio-oil Water Insoluble Content

Bio-oil water insoluble content has been identified as relatively high molecular weight lignin derived species and is commonly referred to as "pyrolytic lignin".[20] The insoluble content of each stage fraction was measured in triplicate for each test and analyzed using statistical software as outlined in section 4.4. The results of are displayed in Figure 24. A general trend of decreasing water insoluble content with decreasing stage fraction collection temperature is observed and consistent with previous results.[14]

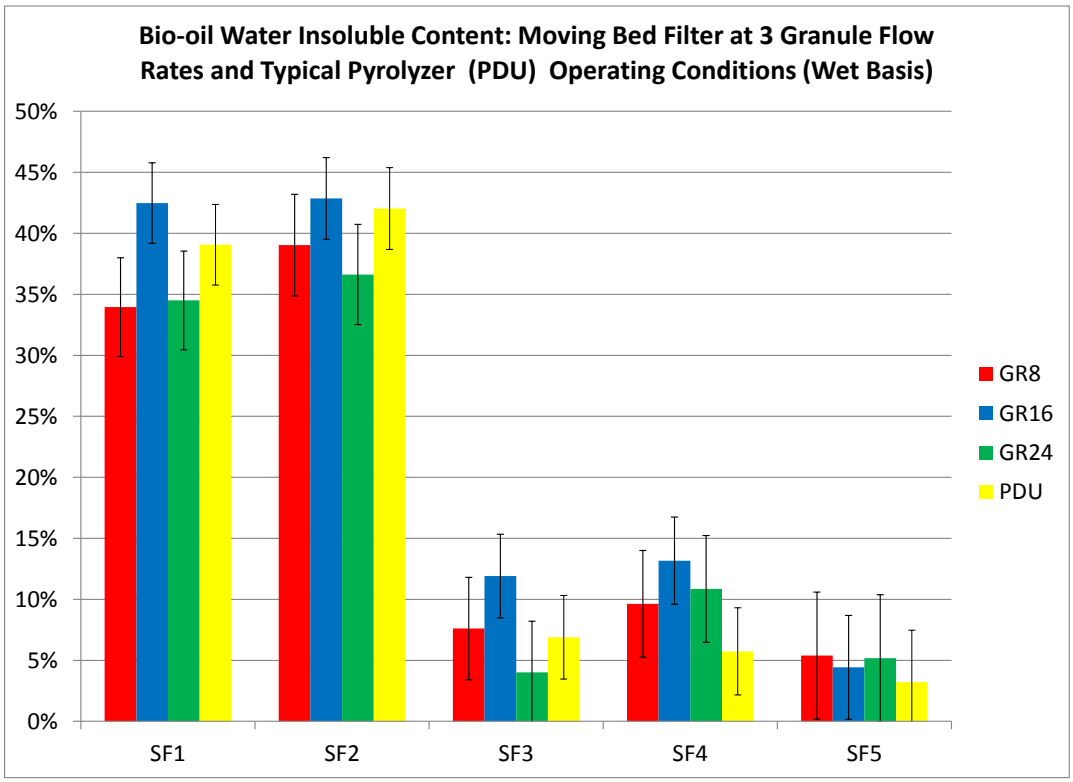

Figure 24: Bio-oil Water Insoluble Content (Wet Basis)

However, an interesting trend is present within the insoluble data. Operating the MBGF at granule flow rates of 8 and 24 kg/h resulted in similar bio-oil water insoluble content in the first two fractions, while operation at 16 kg/h and baseline PDU conditions

yielded as much as 10% higher water insoluble content. This phenomenon may indicate an optimum MBGF operating condition if the primary goal is to maintain similar water insoluble content as baseline pyrolysis. Although less pronounced, the mass averaged water insoluble content shown in Figure 25 displays a similar trend. The water insoluble content of the bio-oil under each operating condition amounted to approximately 20% of total bio-oil yield, which is similar to previously reported results.[14]

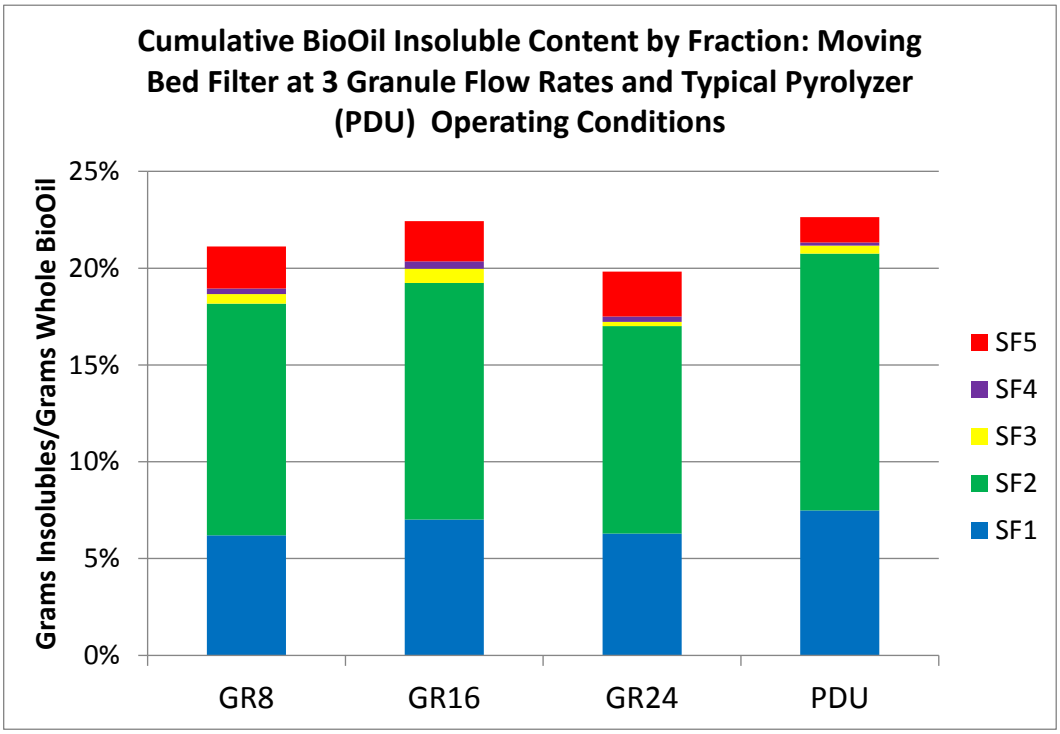

Figure 25: Mass Averaged Water Insoluble Content (Wet Basis)

4.6 Bio-oil Solids Content

Due to the inconsistency of previous results, a new method was developed for measuring bio-oil solids content. This method made use of larger sample sizes in an effort to obtain more representative samples. These pre-weighed samples were collected immediately after bio-oil generation while the viscous fractions were still at collection

temperature in order to avoid the possible increase in solids content that occurs with aging of bio-oil during heating. The samples were performed in triplicate for each test resulting in 6 instances each for GR8, GR24 and PDU baseline samples and 9 instances for GR16 samples. The data was analyzed and statistical model fit as previously described in section 4.4. However, this method of collection and analysis did not seem to improve the inconsistent results as displayed in Figure 26.

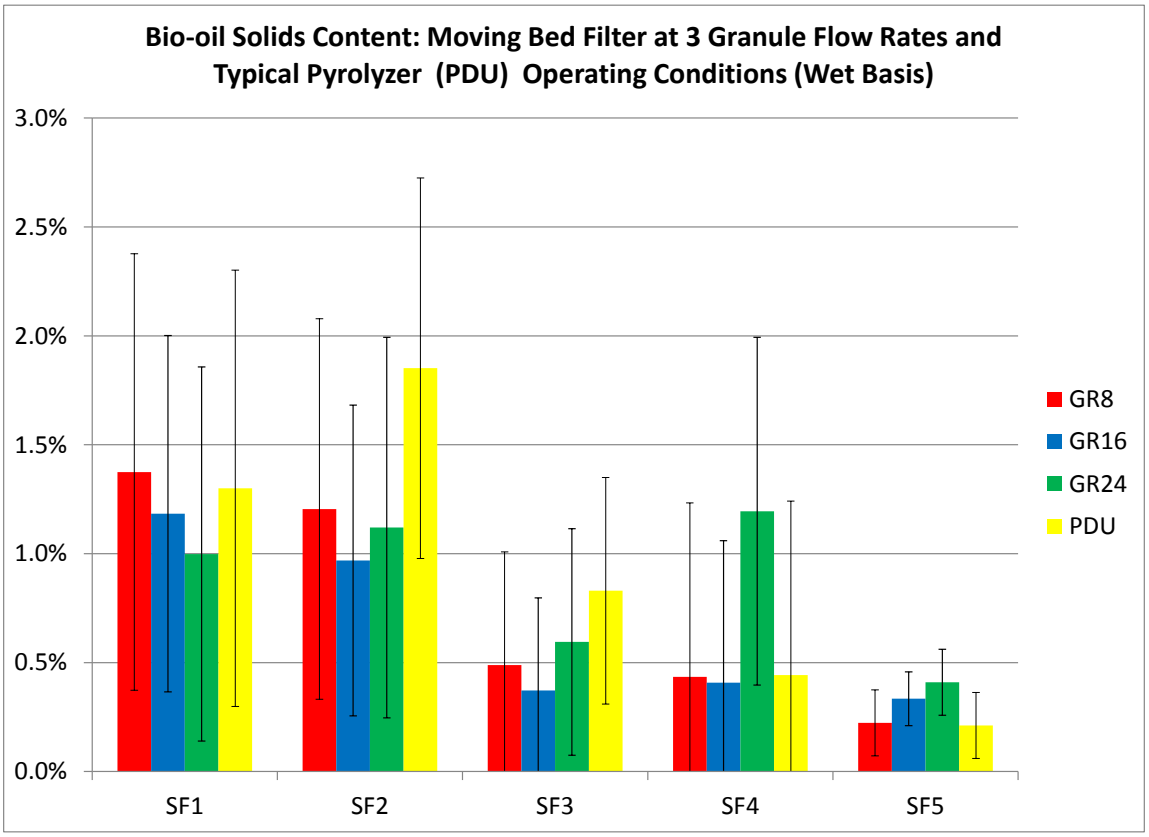

Figure 26: Bio-oil Solids Content (Wet Basis)

The error bars displayed on the chart correspond to 95% confidence intervals as taken across all sample instances at each operating condition. As a result, no meaningful quantitative conclusions can be drawn from this data. However, it would appear that at least

some solid content is present in all samples tested and could be higher than 1% in the first two stage fractions.

Inconsistent results can be attributed in part to the nature of bio-oil and the durability of its water insoluble content. Lignin derived materials can withstand the attack of some of the most aggressive solvents such as the methanol used in this analysis. They are therefore not always dissolved sufficiently allowing this material to be caught in filter paper and erroneously contribute to the solids content. Evidence of this effect is present in the consistent error associated with stage fraction 2 solids content, regardless of operating conditions, as this fraction is designed to capture lignin derived materials.

4.7 SEM

In an effort to better understand the properties of the char collected throughout the filtration process, samples were analyzed using SEM technology. Samples collected from the cyclone, separated from the filtration media, and extracted from bio-oil were analyzed for both morphology and trace metal content.

Figure 27 displays images obtained with the microscope at three different magnifications. In general, the 100x magnification SEM images are taken as a representative example of the particle distribution found in each sample. Higher magnifications are useful in examining the morphology of smaller particles. As shown in Figure 27, char caught in the primary cyclone contains large numbers of elongated particles, some of which feature tubules and porous structures which appear to retain the original biomass structure. These particles are clearly charred plant fibers (primary char).

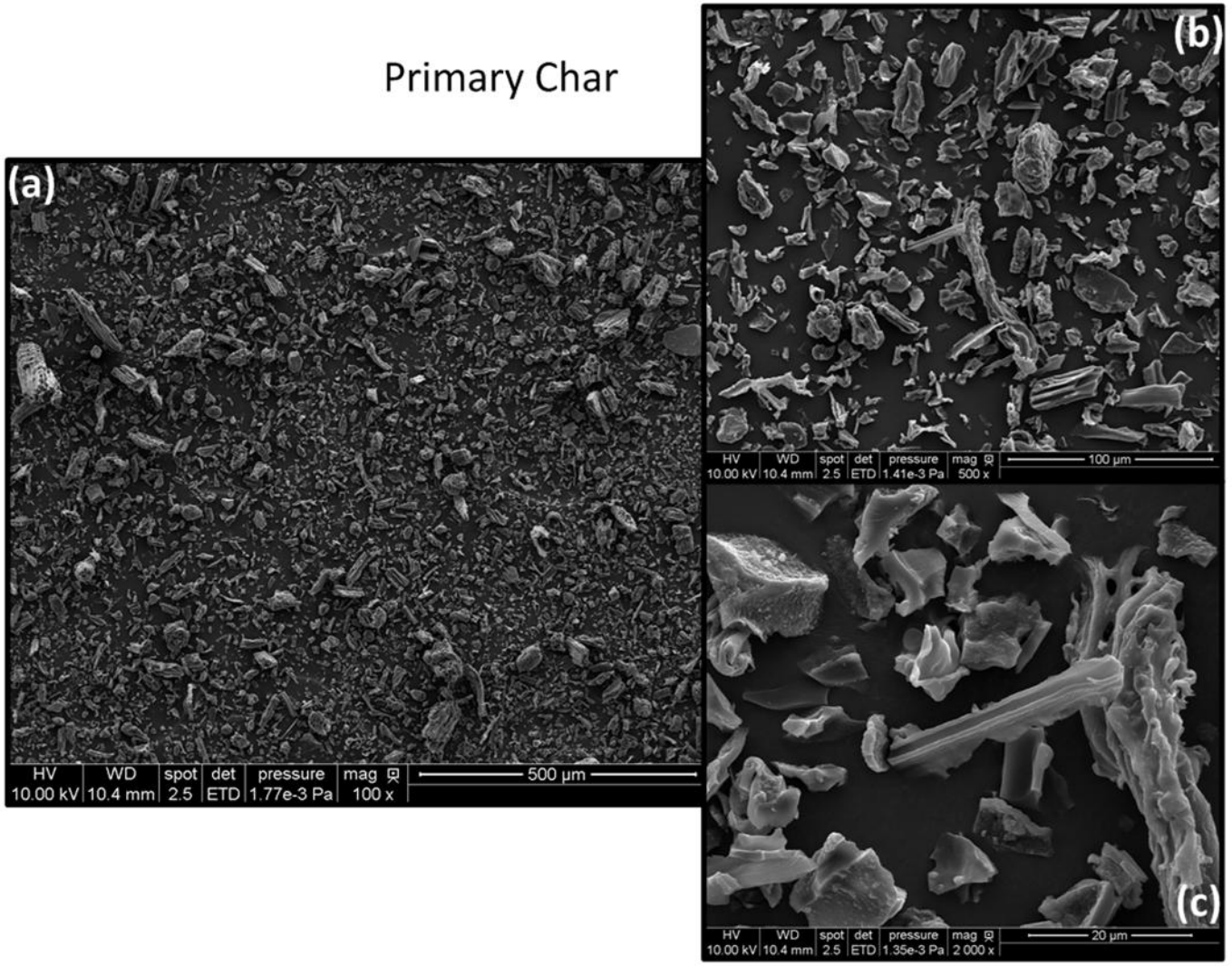

Figure 27: Primary Cyclone Char Images at a) 100, b) 500, and c) 2000x Magnification

Char separated from the filtration media is shown at several magnifications in Figure 28. At 100x magnification the filtration media (50-200 μm dia.) is clearly identified. The image taken at 500x magnification allows the smaller particles, which originate from the gas flow, to be better distinguished. Two different types of morphological structures are present. Elongated, porous particles typical of primary char are evident. These contrast with amorphous particles that do not appear to be the primary product of pyrolyzing biomass. Instead, these carbonaceous particles appear to have been generated from the shattering of a vitreous monolith into many small fragments. Generation of such monoliths would require the impaction of liquid aerosols or the condensation of vapors onto the granular filter media where they could form a liquid film. The film then polymerized and/or dehydrated to a thin plate of charcoal on and between the granular media. As the granules flowed down through the filter, the thin plates of smooth char would collapse and break into particles observed in the SEM. Magnification to 5000x reveals that the surfaces of the vitreous fragments are covered with tiny, spherical particles, which suggest that fine aerosols were the origin of the liquid phase.

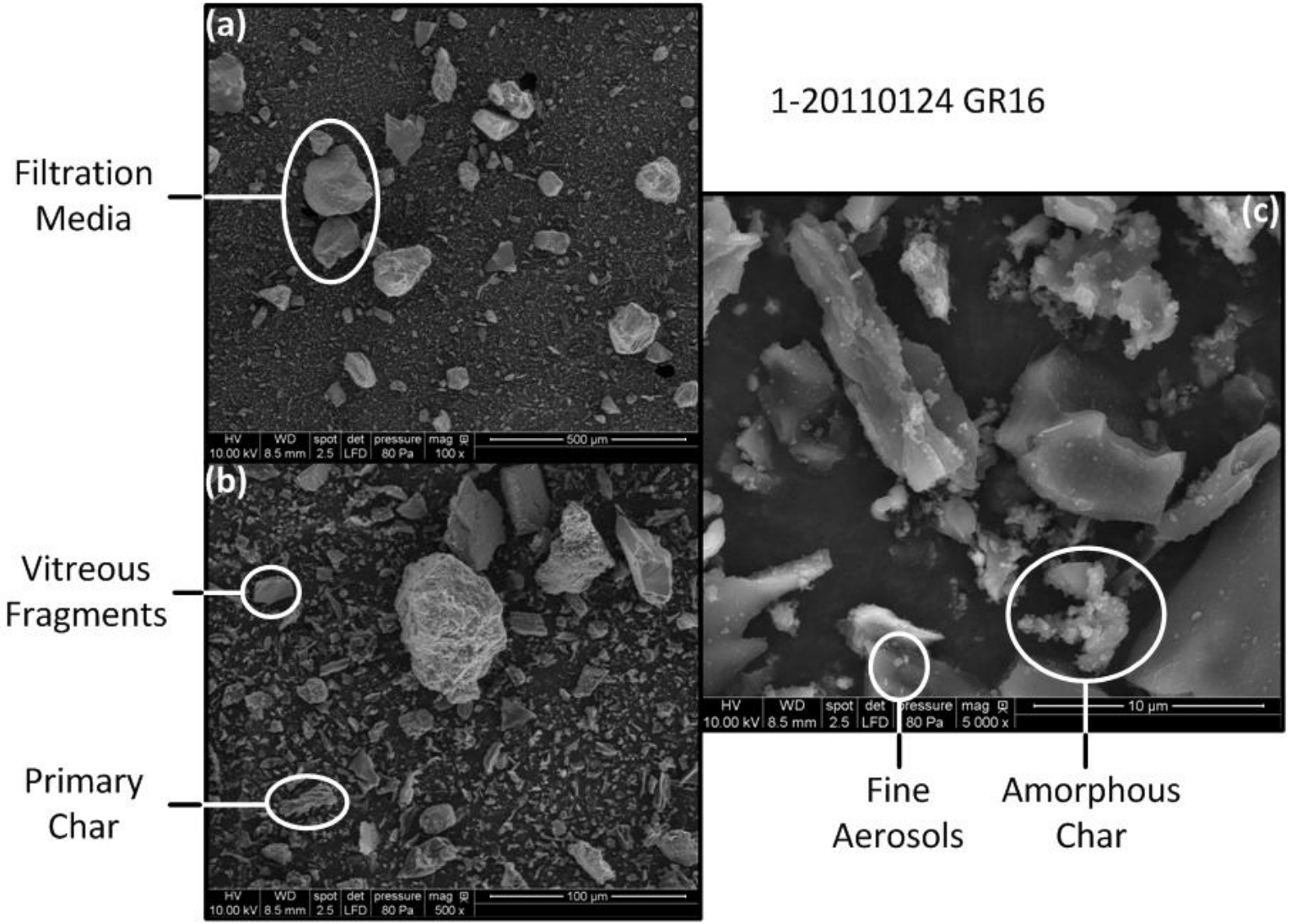

Figure 28: MBGF Separated Char Images at a) 100, b) 500, and c) 5000x Magnification

In order to have a complete examination of the char throughout the filtration process, char was extracted from bio-oil collected downstream of the moving bed filter. Bio-oil was dissolved in methanol and filtered; the filter was then scraped to obtain a solids sample which could then be analyzed using the SEM. Figure 29 displays SEM images for particulate matter collected from the MBGF and bio-oils from stage fractions 1 and 2 for three media flow rates at 100x magnification. Similarly to the 16 kg/h flow rate previously discussed, the 8 and 24 kg/h MBGF samples contain a variety of particulate matter including mineral matter from the breakdown of filtration media. Qualitatively, it would appear that the 24 kg/h test had the most mineral matter content followed by the 16 kg/h test with the 8 kg/h test having the least filtration media content. This suggests that higher auger speeds promotes grinding of stone used as filter media, the resulting mineral dust being entrained with the gas flow moving through the filter. This apparent increase in mineral matter dust may also be due simply to the increased exposure of pyrolysis gases to larger amounts of filtration media at higher granular flow rates.

Amorphous particles are present in all SF1 extracted samples and are markedly similar to those observed in the MBGF separated particulate. No evidence of primary char was observed in these samples. SF2 extracted solid content was also composed entirely of the amorphous particulate matter and in a seemingly smaller quantity than that of stage fraction 1. Both 24 kg/h stage fraction derived samples appear to have a higher concentration of particulate matter than tests at lower flow rates. This could be an indication that sufficient filter cake may not develop at the higher granular flow rate resulting in decreased filtration efficiency.

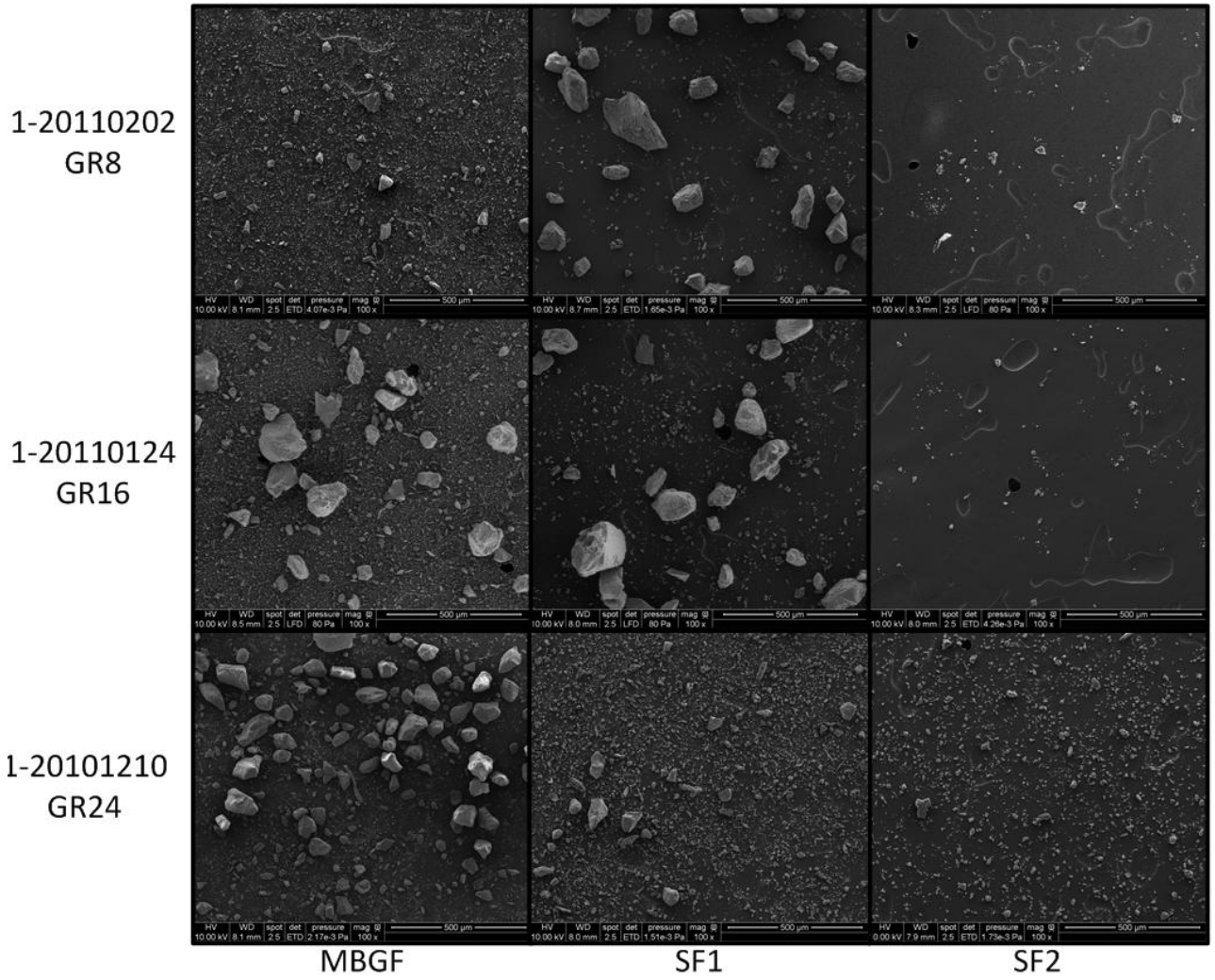

Figure 29: SEM images (100x) of particulate matter recovered from the filtration media of the MBGF and two stages of bio-oil recovery (SF1 and SF2) for three granular flow rates through the filter (GR8, GR16, and GR24 corresponding to 8, 16, and 24 kg/h, respectively)

Figure 29 also reveals the presence of jagged edged particulate in the SF1 bio-oil recovery samples for all three granule flow rate conditions. A hypothesis was formed that the material is mineral matter dust derived from the filtration media which has elutriated from the moving bed filter. In order to test this hypothesis, an SF1 extracted sample was analyzed using a second SEM equipped with EDS detector capable of measuring trace metal content. If the jagged edged particulate is derived from filtration media, a comparison of SF1 extracted particulate and a sample of clean filtration media would result in corresponding x-ray spectrums. Such a comparison is presented in Figure 30. The signal peaks of sodium, aluminum, silica, and potassium correlate well between the two spectrums and have very similar response magnitudes. This is a good indication that the trace metal content in the bio-oil solids is mineral matter dust elutriating from the MBGF and collecting in SF1.

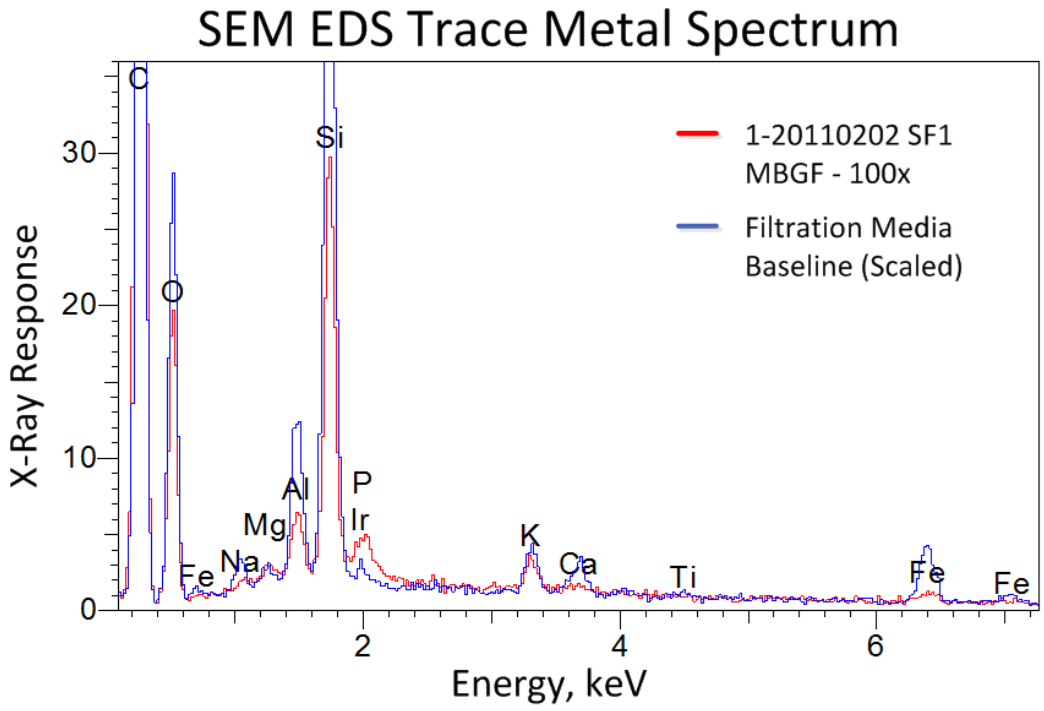

Figure 30: Trace Metal EDS X-Ray Spectrum of Particulate Matter Recovered from SF1 8 kg/h MBGF Test (red) Compared to Clean Crushed Filtration Media – Scaled X-Ray Response (blue)

The large iron (Fe) peak associated with filtration media is due to the method by which the sample was prepared. In order to properly image the media, it had to be crushed and ground to a uniform size. However, during the ball milling operation, stainless steel ball bearings were used to grind the media after which, the surface of the bearings were noticeably dull. It is believed that the media sample was contaminated by the wearing of the steel surface against the media, resulting in the noticeable spike in Figure 30.

In addition to spectrum analysis, the EDS detector is capable of x-ray mapping samples to indicate the origin of trace metal signals as indicated by a lighter appearance in the map. An x-ray map of the SF1 solids content of an 8 kg/h MBGF test is shown in Figure 31. The background picture in the upper left-hand corner indicates the position of jagged edged particulate matter located throughout the sample. It is very clear through this analysis that the material is primarily composed of aluminum and silica with small amounts of potassium, calcium, magnesium, and iron which correlates well with the baseline filter media spectrum from above.

The mapping does not indicate the presence of trace metals in the smaller amorphous particulate matter contained in the sample. Some sodium content is present, however the particles are mainly composed of oxygen and carbon as indicated in Figure 31. Since alkali metal concentration is typically high in primary char, the absence of trace metal in this particulate matter suggests that it was formed after primary pyrolysis during solid-vapor phase interactions (secondary char). It should be noted that the dark shadow regions in the carbon trace map are due to the angle of the EDS detector in relation to the sample causing the larger, jagged edged particulate to overshadow portions of the sample.

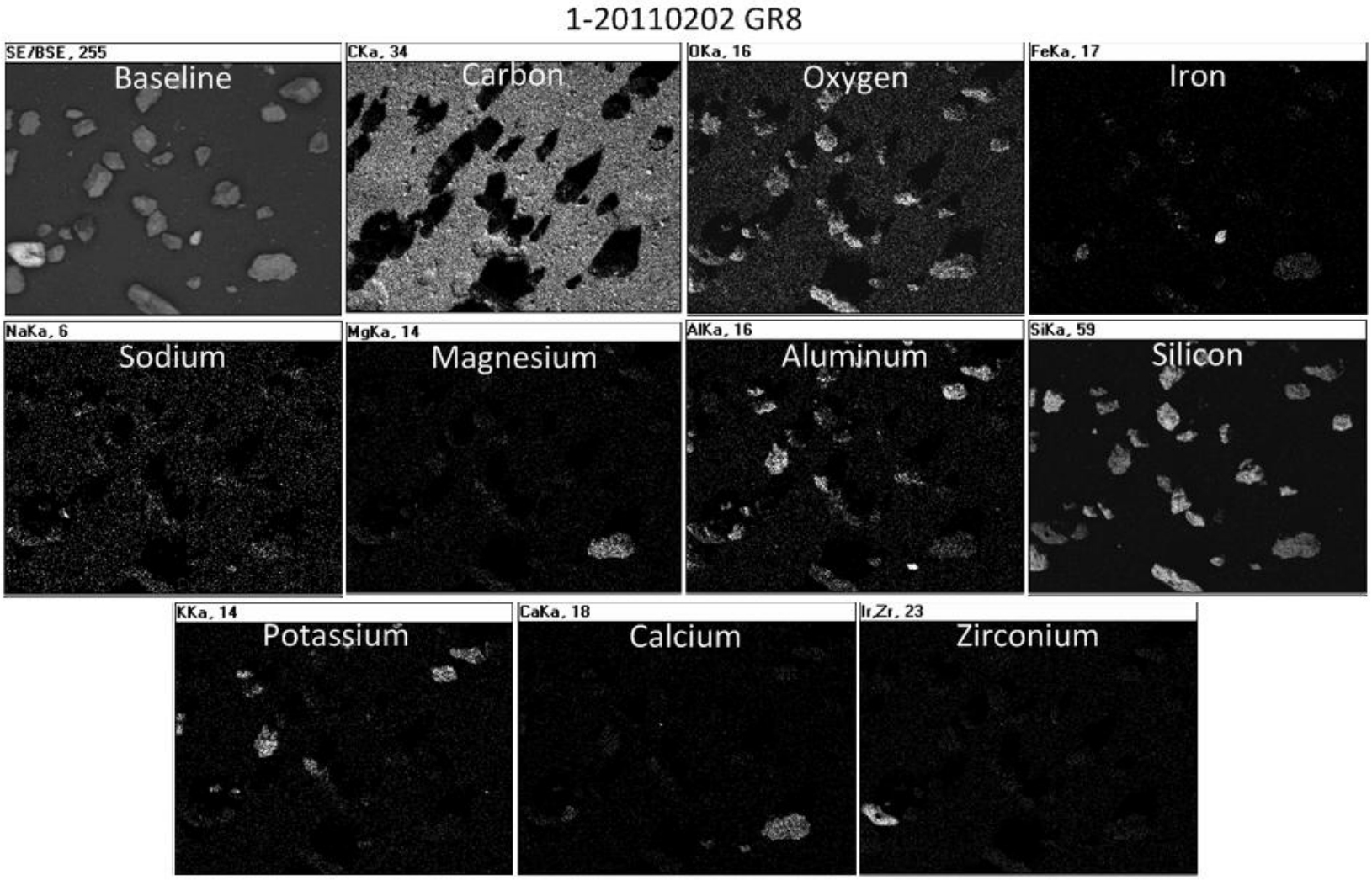

Figure 31: Elemental EDS X-ray Map of SF1 Extracted Solids Content, MBGF 8 kg/h

If the hypothesis presented above holds, a solids extraction from SF1 under normal PDU operation without the MBGF in-situ would not contain any jagged edged particulate. The comparative SEM images for SF1 extracted content are displayed in Figure 32. The PDU baseline sample shows no trace of jagged edged particulate, further supporting the hypothesis. The PDU sample also clearly indicates the presence of primary char. Comparatively, it would appear that the solids collected from the PDU baseline sample are due to a range of particles including both primary char and smaller amorphous particulate matter while the majority of the matter in the MBGF sample is due to the jagged edge particles. Due to its greater density, the jagged edged particulate would have an overwhelming effect on the solids content analysis performed in Section 4.6. The presence of this material is likely the reason a reduction in bio-oil solids content in SF1 samples collected post moving bed filtration could not be detected through mass differencing methods and could also be a factor in measurement consistency.

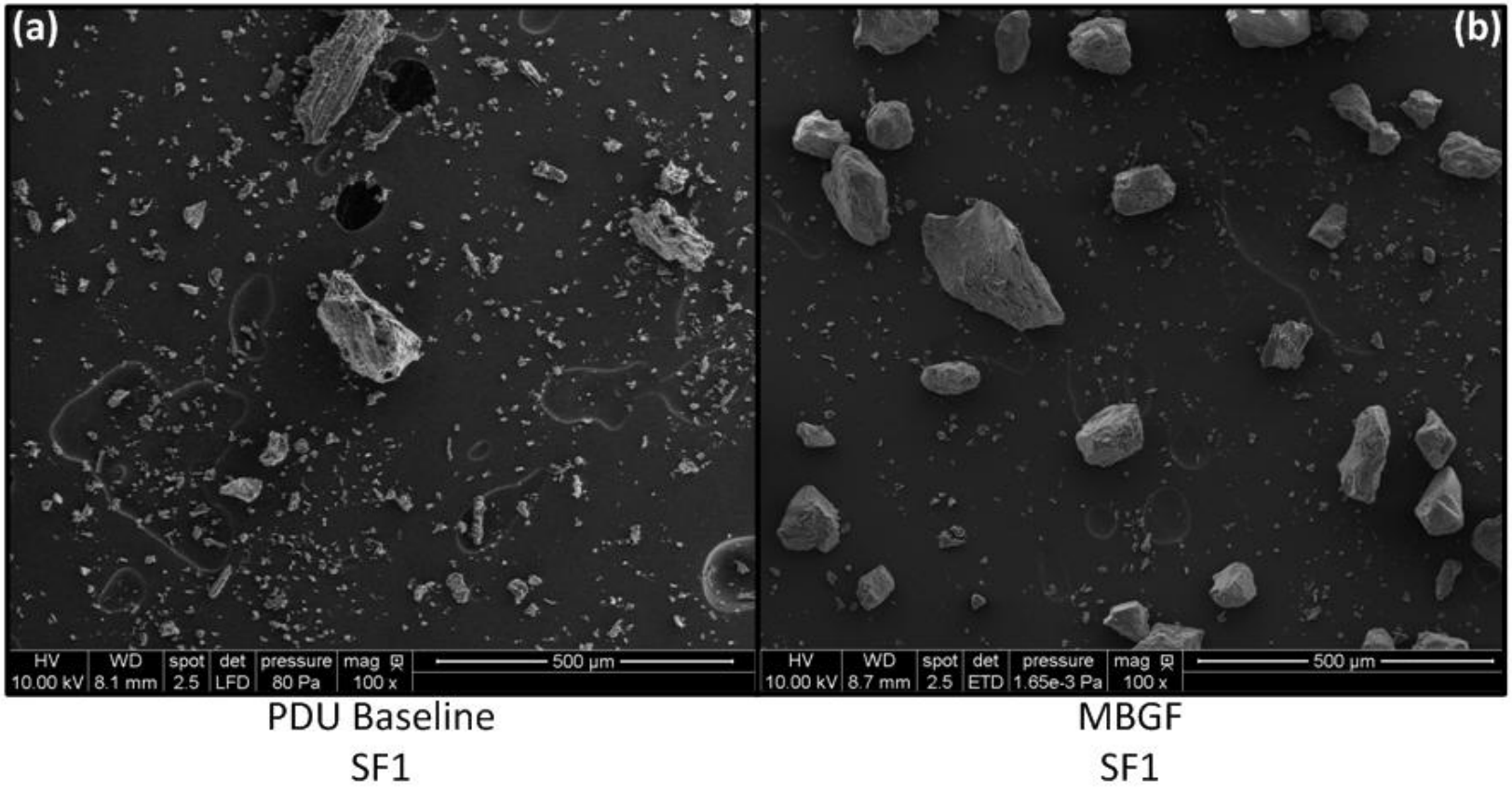

Figure 32: a) PDU Baseline and b) MBGF Bio-oil Solids Extraction SEM Comparison - 100x Magnification

As a result of this analysis it can be concluded that the jagged edge particulate present in the SF1 bio-oil extracted samples is originating from the elutriation of filter media derived mineral matter dust from the MBGF. Qualitatively, the 8 and 16 kg/h tests had increased mineral matter content in SF1 samples compared to the 24 kg/h test. This is likely due to the increased operating pressure differential associated with slower granular flow rates, which translates into increased face velocity at the gas disengagement section of the MBGF. Due to the uniformity of the size, greater density, and larger particle size when compared to the char particulate designated for removal, the MBGF could easily be redesigned to avoid this elutriation. A simple geometry change resulting in a larger surface area at the filter's exit and thus a slower exit face velocity could eliminate this phenomenon all together.

Figure 33 is a closer examination at 500x magnification of the smaller particulate matter in both of these samples. Once again, a range of biomass derived particles are present in the SF1 baseline sample along with amorphous particulate matter which appears in both SF1 and SF2 (circled). These same particles are present in both of the MBGF samples.

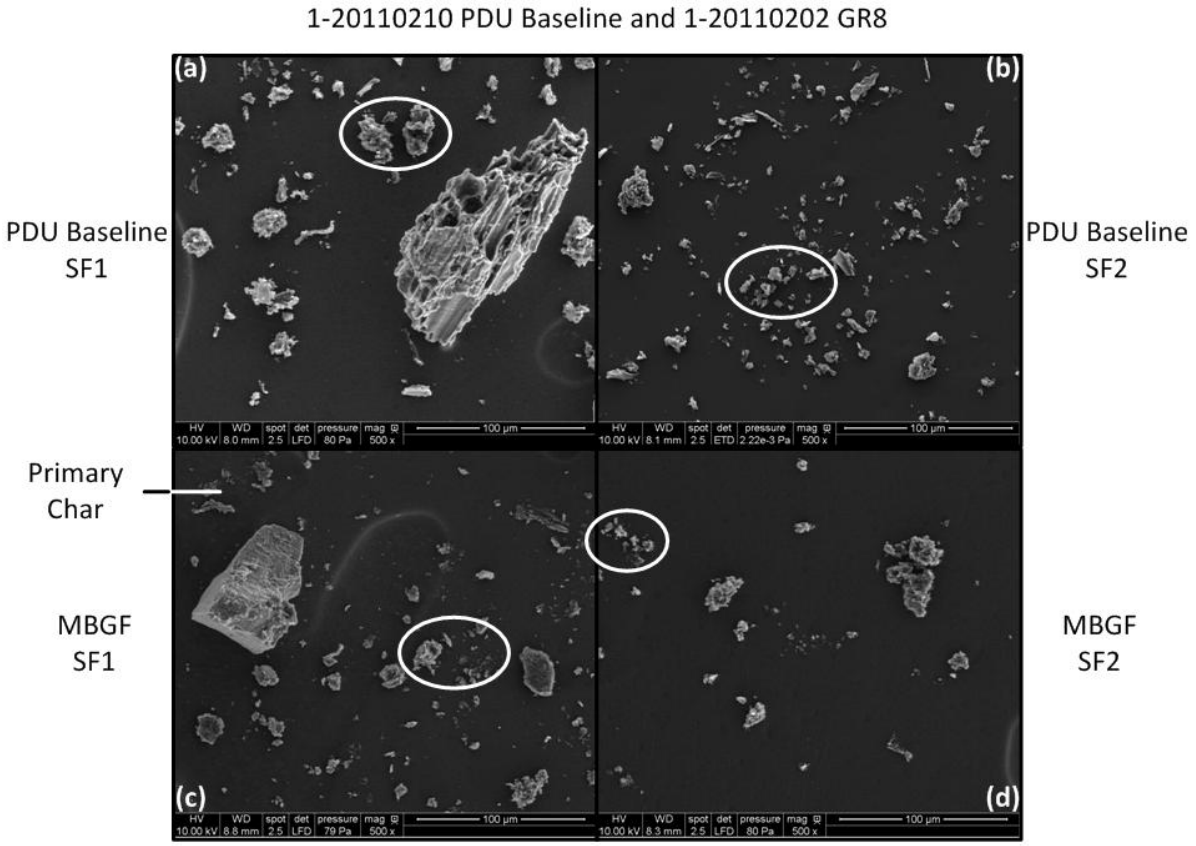

Figure 33: Bio-oil Solids Extraction SEM Images for a) SF1 PDU Baseline, b) SF2 PDU Baseline, c) SF1 MBGF, d) SF2 MBGF - 500x Magnification

Figure 34 provides a 2000x magnification of the amorphous particles highlighted by white circles in the figure above. Aside from nucleation size, the morphology of the structures is markedly similar in all four cases and appears to have formed by the same process.

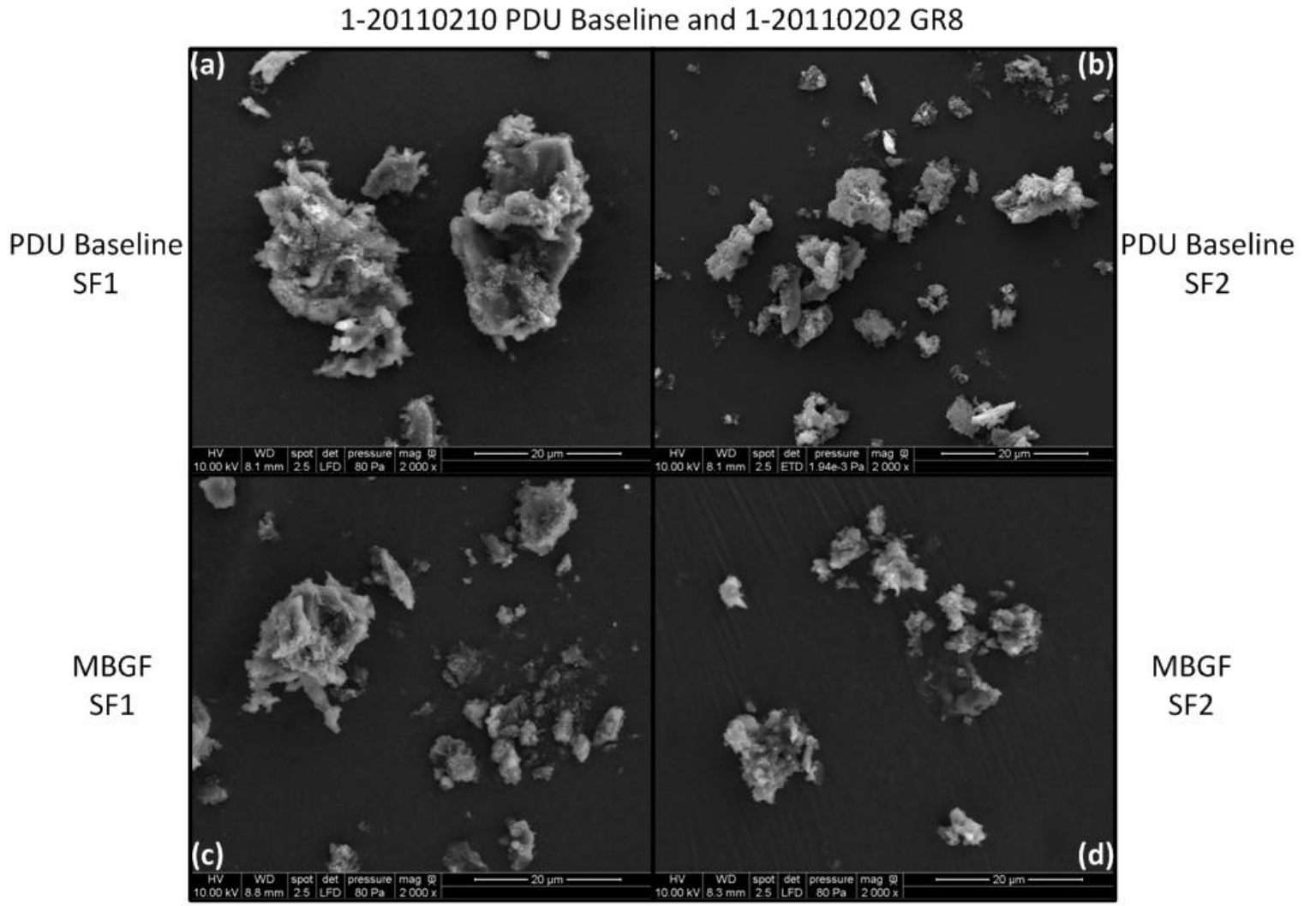

Figure 34: Bio-oil Solids Extraction SEM Images for a) SF1 PDU Baseline, b) SF2 PDU Baseline, c) SF1 MBGF, d) SF2 MBGF - 2000x Magnification of Amorphous Particles Indicated by White Circles Above

A 20,000x magnification of the amorphous particulate matter reveals very interesting morphology and some insight as to how the particles were formed. Figure 35 displays two different amorphous particles from an 8 kg/h MBGF char sample that were separated from the filter media with a sieve shaker. Image 'a' appears to be the result of a nucleation process in which spherical particles impacted or collected and melted together to form agglomerate. These particles appear to have formed as spheres no larger than 1µm dia. that partially sintered after impaction on the filter media. Image 'b' shows a combination of this type of formation along with a second type of nucleation. This process involves spherical particles on the order of 0.01 µm or smaller, resulting in extremely porous structures resembling amorphous rock. These amorphous structures appear to be the result of secondary reactions that occur due to either aerosol collection of pyrolysis stream constituents or condensation/dehydration reactions which nucleate and form larger charred structures.

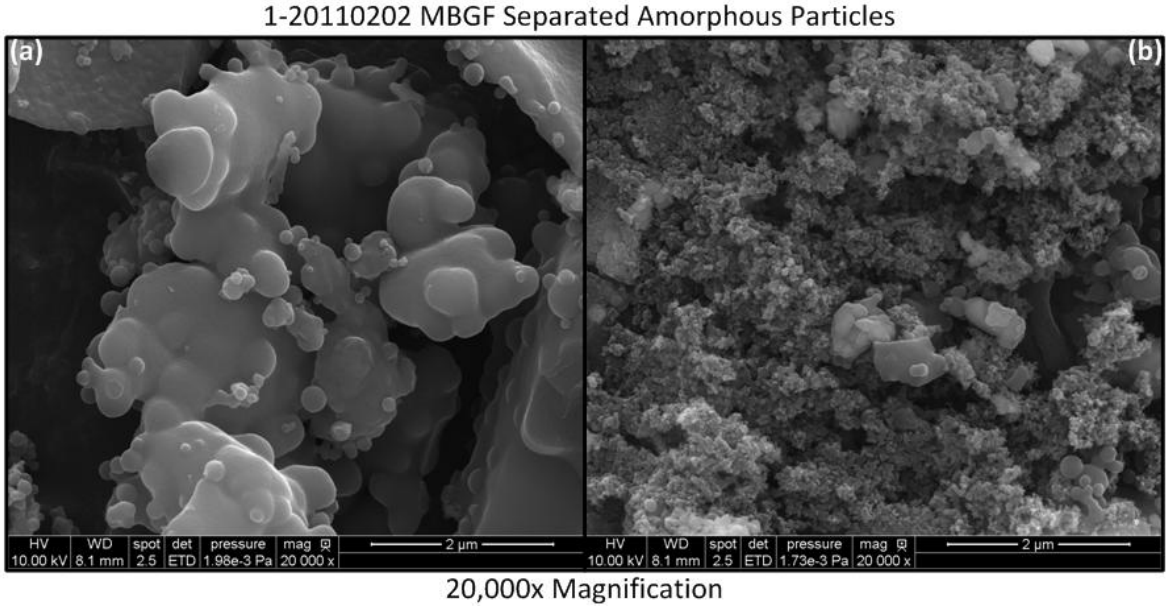

Figure 35: SEM Images of Two Amorphous Particles from MBGF Separated Char - 20,000x Magnification

Due to the limited amount of information available regarding secondary char production and morphology, a sample of pure secondary char was desired for analysis. In each MBGF test, a thin layer of char was observed on the interior surface of the outlet pipe of the filter. Since the primary char is assumed to be removed in the filter, it was hypothesized that this char formation was due to secondary reactions resulting in the accumulation of very fine particles. A sample of this char was collected and analyzed using the SEM, the results of which can be seen in Figure 36. Once again, these structures appear to have been formed by a nucleation process involving 1 µm and smaller particles which agglomerated to form a vitreous solid. This result is unexpected if the material impacted as discrete, refractory char particles.

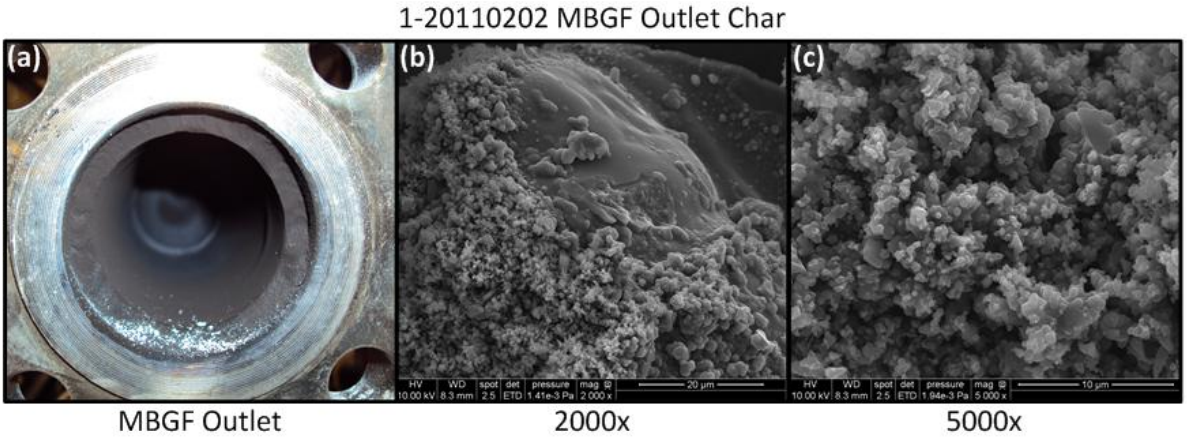

Figure 36: a) MBGF Outlet Char Sample and SEM Imaging at b) 2000x and c) 5000x Magnification

A test was devised to produce a sample of predominately secondary char for comparative analysis. This process involved the utilization of a high temperature barrier filter on the exit of a bench scale pyrolysis reactor. The pyrolysis stream was forced to pass through this filter in order to exit the reactor, resulting in the buildup of a char layer. The

continuous passing of vapors and aerosols through this char layer is assumed to cause secondary reactions as suggested in Figure 9. Details of this test can be found in APPENDIX F. A sample of the char generated in this test was analyzed with the SEM and is shown in Figure 37. These images reveal distinctly spherical particles on the order of 1 mm or smaller that appear to have undergone little sintering and consolidation. The extreme sphericity of these particles suggest their formation from a gas-phase nucleation process to directly form a solid or the production of a liquid with subsequent solidification before capture by the fibers of the barrier filter. In contrast, the deposits from the MBGF also show evidence of nucleation in the gas phase to form micron or submicron size spherical droplets, but these appear to have undergone significant sintering after capture by the granular filter media of the MBGF.

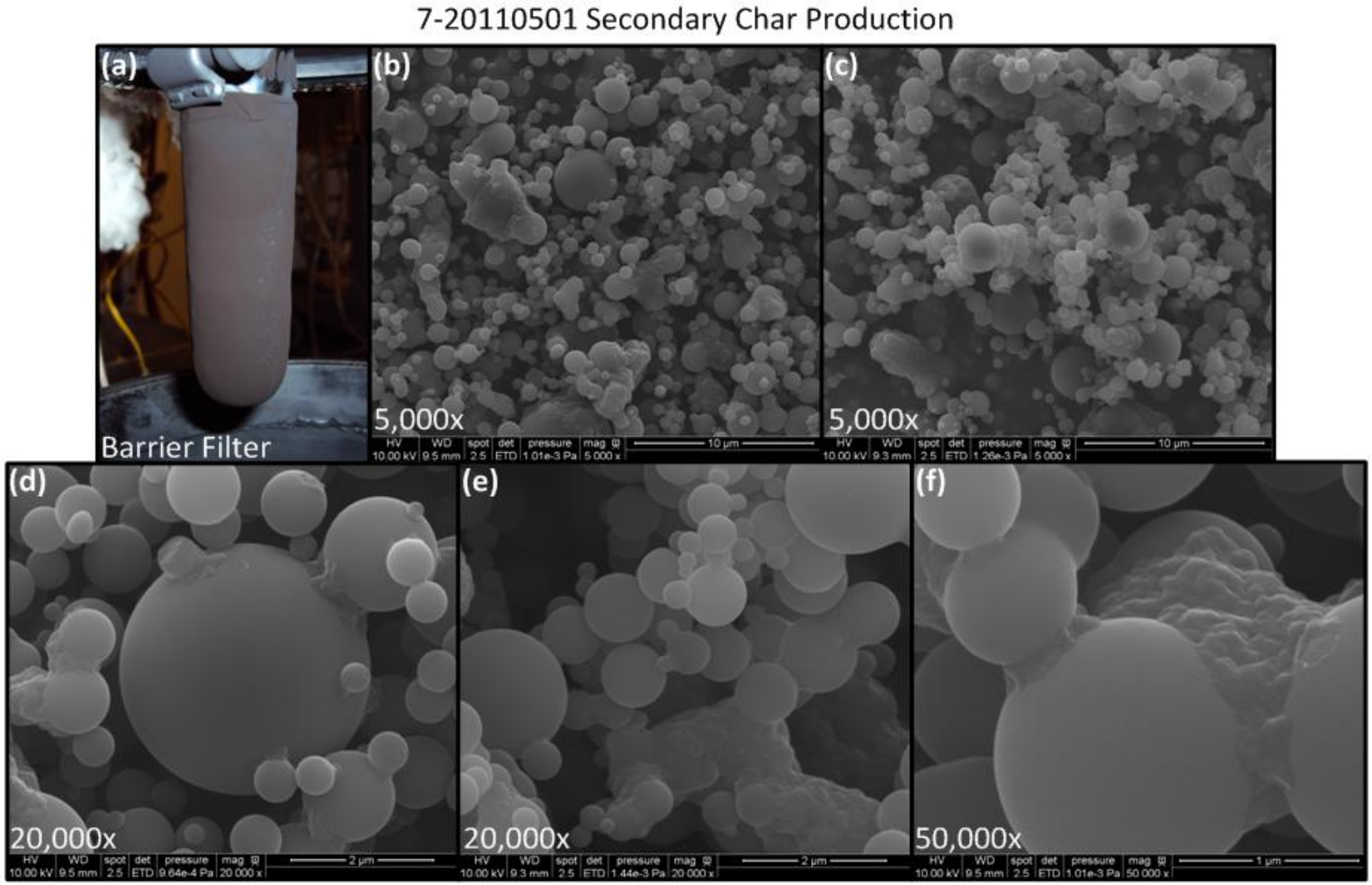

Figure 37: a) Secondary Char Produced on Bench Scale Pyrolyzer Using Barrier Filter – SEM Imaging at b) 5000x, c) 5000x, d) 20,000x, e) 20,000x, and f) 50,000x Magnifications

Production of secondary char from lignin-derived oligomers offers an explanation of the perfectly spherical particles observed in the barrier filter. When heated, lignin undergoes a melt phase. Some researchers explain the presence of "pyrolytic lignin" in bio-oil to entrainment of melted lignin oligomers as fine aerosols into the gas stream flowing through a pyrolysis reactor.[42] The dehydration of these oligomers to coke either before or after impaction on the filter would readily explain the SEMs observed in the present study. However, the mechanism by which up to 20-25 wt% of the pyrolyzed biomass is entrained as lignin-derived aerosols is unclear and even problematic, suggesting another explanation for secondary char from lignin. Some researchers have observed significant generation of phenolic monomers under some conditions of lignin pyrolysis.[16] These highly reactive compounds conceivable could re-polymerize in the gas-phase and nucleate as liquid phenolic oligomers. This would explain both the presence of non-volatile, lignin-derived compounds in bio-oil and the spherical structure of secondary char. Considering lignin-derived oligomers make up 20wt% or more of bio-oil suggests that most of the secondary char arises from melted phenolic oligomers.

The agglomeration of deposited aerosols in the MBGF suggests that dehydration to char occurs after deposition while the unconsolidated aerosols found on the barrier filter indicates their dehydration to char before impaction. One explanation of this inconsistency lies in the environments in which each phenomenon occurs. Aerosols moving through the MBGF are subject to constantly shifting filtration media, which when collapsing could fall through aerosol flow paths and impact the liquid droplets on the media surface as a result its movement. Contrarily, the stationary environment of the barrier filter would lend itself to the gradual deposition of aerosol droplets as a function of decreasing void space.

A second explanation involves the amount of sweep gas present in each environment. If it is assumed that the majority of the aerosol impinging occurs at the interfacial region of the MBGF, the surface area through which the 500 SLPM of pyrolysis gas passes is approximately 70 cm^2, resulting in a superficial velocity of 1.1 m/s. However, in the case of the barrier filter, the gas flow rate is 5 SLPM through a surface area of 67 cm^2, resulting in a superficial velocity of 0.012 m/s. The vast difference in sweep gas volume and velocity translates into increased vapor residence time in the barrier filter environment, allowing sufficient dehydration reactions to take place prior to impaction on the filter surface.

4.8 ICP-AES

In order to help track the movement of primary char through the pyrolysis and filtration process, samples of biomass, char and bio-oil were subjected to trace metal analysis via ICP-AES. Since primary char is high in alkali metal content, trace metal content within the produced bio-oil will give another metric to track filtration effectiveness. Table 6 details the trace metal content of samples of all five stages of bio-oil obtained from a PDU baseline test. Each sample was measured in duplicate providing the basis for the average and standard deviation calculations highlighted in bold. In addition to bio-oil, samples of biomass and cyclone char have been displayed at the top of the table for comparison. Most notably, the metal content from biomass is concentrated into the cyclone recovered char, especially in the cases of phosphorous, potassium, sodium, magnesium, calcium, manganese and iron. These results are in good agreement with Jendoubi et al.[43]

Table 6: Trace Metal Content of Pyrolysis Products from PDU Baseline Test

	Metal Content, PPM									
Sample Name	P	K	Na	Mg	Ca	Mn	Fe	Cu	Zn	Al
1-20110221 Red Oak	38	887	88	34	697	33	2	1	36	63
Feed	42	878	89	37	726	32	9	1	11	72
Average	**40 ± 3**	**883 ± 7**	**88 ± 0**	**35 ± 2**	**712 ± 21**	**33 ± 0**	**5 ± 5**	**1 ± 0**	**23 ± 18**	**67 ± 7**
1-20110221 1st	198	5510	139	379	7228	312	96	10	44	2
Cyclone Char	176	4769	116	331	6453	275	29	7	20	31
Average	**187 ± 15**	**5139 ± 524**	**127 ± 17**	**355 ± 34**	**6840 ± 548**	**294 ± 26**	**63 ± 47**	**8 ± 3**	**32 ± 17**	**17 ± 21**
1-20110221 2nd	232	8393	179	568	10114	468	147	13	21	26
Cyclone Char	235	7916	168	546	9454	446	151	12	23	7
Average	**234 ± 3**	**8154 ± 338**	**174 ± 7**	**557 ± 15**	**9784 ± 467**	**457 ± 16**	**149 ± 3**	**12 ± 1**	**22 ± 2**	**17 ± 13**
1-20110210 Stage	37	421	63	5	97	6	25	2	127	20
Fraction 1 (BASELINE)	34	490	110	13	37	8	3	4	101	47
Average	**36 ± 2**	**455 ± 49**	**87 ± 34**	**9 ± 5**	**67 ± 43**	**7 ± 2**	**14 ± 15**	**3 ± 1**	**114 ± 18**	**34 ± 19**
1-20110210 Stage	33	534	97	17	94	7	3	3	43	33
Fraction 2 (BASELINE)	35	684	91	21	61	8	0	5	32	59
Average	**34 ± 2**	**609 ± 106**	**94 ± 4**	**19 ± 3**	**78 ± 23**	**8 ± 1**	**2 ± 2**	**4 ± 1**	**38 ± 8**	**46 ± 18**
1-20110210 Stage	66	537	91	3	34	5	249	22	33	35
Fraction 3 (BASELINE)	40	601	82	12	65	7	217	1	22	60
Average	**53 ± 18**	**569 ± 45**	**87 ± 7**	**7 ± 6**	**49 ± 22**	**6 ± 1**	**233 ± 23**	**12 ± 15**	**28 ± 7**	**48 ± 18**
1-20110210 Stage	33	357	82	13	80	6	140	5	21	44
Fraction 4 (BASELINE)	30	357	82	13	61	6	142	5	31	71
Average	**32 ± 2**	**357 ± 0**	**82 ± 1**	**13 ± 1**	**70 ± 13**	**6 ± 0**	**141 ± 2**	**5 ± 0**	**26 ± 7**	**57 ± 19**
1-20110210 Stage	25	329	81	14	63	7	8	1	4	35
Fraction 5 (BASELINE)	26	349	84	15	38	7	11	1	28	49
Average	**25 ± 1**	**339 ± 15**	**83 ± 2**	**14 ± 1**	**51 ± 17**	**7 ± 0**	**10 ± 2**	**1 ± 0**	**16 ± 17**	**42 ± 10**

However, relatively large concentrations of potassium, sodium and calcium remain in each bio-oil stage fraction. This is most likely due to the periodic plugging of the high efficiency cyclone present during prolonged pyrolysis operation. The increased concentration of iron in stage fractions 3 and 4 is due to the use of carbon steel bottle adapters on these stages at the time of this study. The higher acidity of these fractions allows leaching of the base metal to take place as bio-oil exits the stages. Leaching is not observed in stage fractions 1 and 2 due to their low acidity or in stage fraction 5 due to the use of a stainless steel bottle adaptor for bio-oil collection.

A similar analysis was conducted using oil obtained from a 16 kg/h MBGF test, the results of which are displayed in Table 7. The metal concentrations of the feedstock and cyclone chars are reprinted for comparative purposes. Relatively large concentrations of phosphorous, potassium, sodium, calcium, and aluminum are present in MBGF derived bio-oil fractions. These concentrations appear to be on the same order of magnitude as those resulting from standard pyrolysis PDU operation shown previously in Table 6. However, a sample of clean filtration media was also ball milled and digested for analysis, the result of which is displayed in the last entry of Table 7. The filtration media also contains relatively high concentrations of these same elements present in the bio-oil. SEM analysis in section 4.7 confirmed the presence of filtration media derived dust in MBGF SF1 samples. The presence of this dust in the samples would result in increased trace metal concentrations in the resulting bio-oil. It is not unlikely that the dust contamination could reach additional stage fractions in the collection train, resulting in elevated trace metal concentrations in all bio-oil samples.

Table 7: Trace Metal Content of Pyrolysis Products from MBGF Test

	Metal Content, PPM									
Sample Name	P	K	Na	Mg	Ca	Mn	Fe	Cu	Zn	Al
1-20110221 Red Oak	38	887	88	34	697	33	2	1	36	63
Feed	42	878	89	37	726	32	9	1	11	72
Average	**40 ± 3**	**883 ± 7**	**88 ± 0**	**35 ± 2**	**712 ± 21**	**33 ± 0**	**5 ± 5**	**1 ± 0**	**23 ± 18**	**67 ± 7**
1-20110221 1st	198	5510	139	379	7228	312	96	10	44	2
Cyclone Char	176	4769	116	331	6453	275	29	7	20	31
Average	**187 ± 15**	**5139 ± 524**	**127 ± 17**	**355 ± 34**	**6840 ± 548**	**294 ± 26**	**63 ± 47**	**8 ± 3**	**32 ± 17**	**17 ± 21**
1-20110221 2nd	232	8393	179	568	10114	468	147	13	21	26
Cyclone Char	235	7916	168	546	9454	446	151	12	23	7
Average	**234 ± 3**	**8154 ± 338**	**174 ± 7**	**557 ± 15**	**9784 ± 467**	**457 ± 16**	**149 ± 3**	**12 ± 1**	**22 ± 2**	**17 ± 13**
1-20110221 Stage	70	421	59	4	93	11	2	0	10	35
Fraction 1 (MBGF)	75	363	61	3	131	11	1	0	14	48
Average	**72 ± 3**	**392 ± 41**	**60 ± 1**	**3 ± 0**	**112 ± 27**	**11 ± 0**	**1 ± 0**	**0 ± 0**	**12 ± 3**	**42 ± 9**
1-20110221 Stage	75	460	65	10	79	12	32	1	17	24
Fraction 2 (MBGF)	61	411	65	5	66	12	12	1	9	31
Average	**68 ± 10**	**435 ± 35**	**65 ± 0**	**7 ± 3**	**72 ± 9**	**12 ± 0**	**22 ± 14**	**1 ± 0**	**13 ± 5**	**27 ± 4**
1-20110221 Stage	79	398	60	7	126	14	655	1	22	30
Fraction 3 (MBGF)	64	389	63	7	220	15	630	1	26	170
Average	**72 ± 11**	**393 ± 6**	**61 ± 2**	**7 ± 0**	**173 ± 66**	**14 ± 0**	**642 ± 18**	**1 ± 0**	**24 ± 3**	**100 ± 99**
1-20110221 Stage	49	285	46	8	81	10	203	2	36	36
Fraction 4 (MBGF)	50	374	55	7	61	13	255	1	19	9
Average	**50 ± 0**	**329 ± 63**	**50 ± 6**	**7 ± 1**	**71 ± 14**	**12 ± 2**	**229 ± 37**	**1 ± 0**	**28 ± 12**	**23 ± 19**
1-20110221 Stage	46	322	58	5	63	10	5	1	34	23
Fraction 5 (MBGF)	65	514	58	16	96	12	17	3	10	46
Average	**56 ± 13**	**418 ± 136**	**58 ± 0**	**10 ± 8**	**79 ± 23**	**11 ± 1**	**11 ± 8**	**2 ± 2**	**22 ± 17**	**34 ± 16**
Ground Filter Media	366	1224	137	2230	1510	103	10380	12	117	2846
	380	866	132	2410	1926	106	11100	13	85	2952
Average	**373 ± 10**	**1045 ± 253**	**135 ± 4**	**2320 ± 127**	**1718 ± 294**	**105 ± 2**	**10740 ± 509**	**13 ± 0**	**101 ± 23**	**2899 ± 75**

It should be once again noted that the ball milling operation used for size reduction of the filtration media prior to acid digestion most likely contaminated the sample with iron (Fe). Therefore, the large concentration of iron displayed in Table 7 is not indicative of typical iron concentrations in the filtration media.

Graphical comparisons of trace metal content can be found in Figure 38 - Figure 39. The values are mass averaged by bio-oil yield and reported in milligrams of metal. Error bars associated with the data are also mass averaged standard deviations based on two determinations per sample. While all trace metal concentrations appear to be on the same order of magnitude, some differences are present. The phosphorous concentration of all five stage fractions appears to increase when using the MBGF. Potassium concentration was the most significant metal detected and appears to increase in the cases of SF3, SF4 and SF5 when using the MBGF; differences in the other fractions are undetectable due to excessive standard deviation. Sodium concentration is detectably higher when using the MBGF in fractions 3 and 5. Calcium content also increases in all stages barring SF2 where excessive standard deviation is present. Once again, iron concentration is subject to leeching from the bottle adapters and no inferences will be made regarding its content within collected bio-oils.

Due to the error between samples associated with ICP trace metal analysis and to the probable contamination of collected bio-oil by filtration media derived dust, inferences regarding the MBGF's ability to reduce alkali metal concentration are difficult to make. However, in most cases where differences were detectible the use of the MBGF resulted in increased metal content, most likely due to the addition of media dust. It is unclear by this analysis the relative amounts of alkali content that were removed through the filtration of primary char by the MBGF or the amount that was added by the elutriation of media dust.

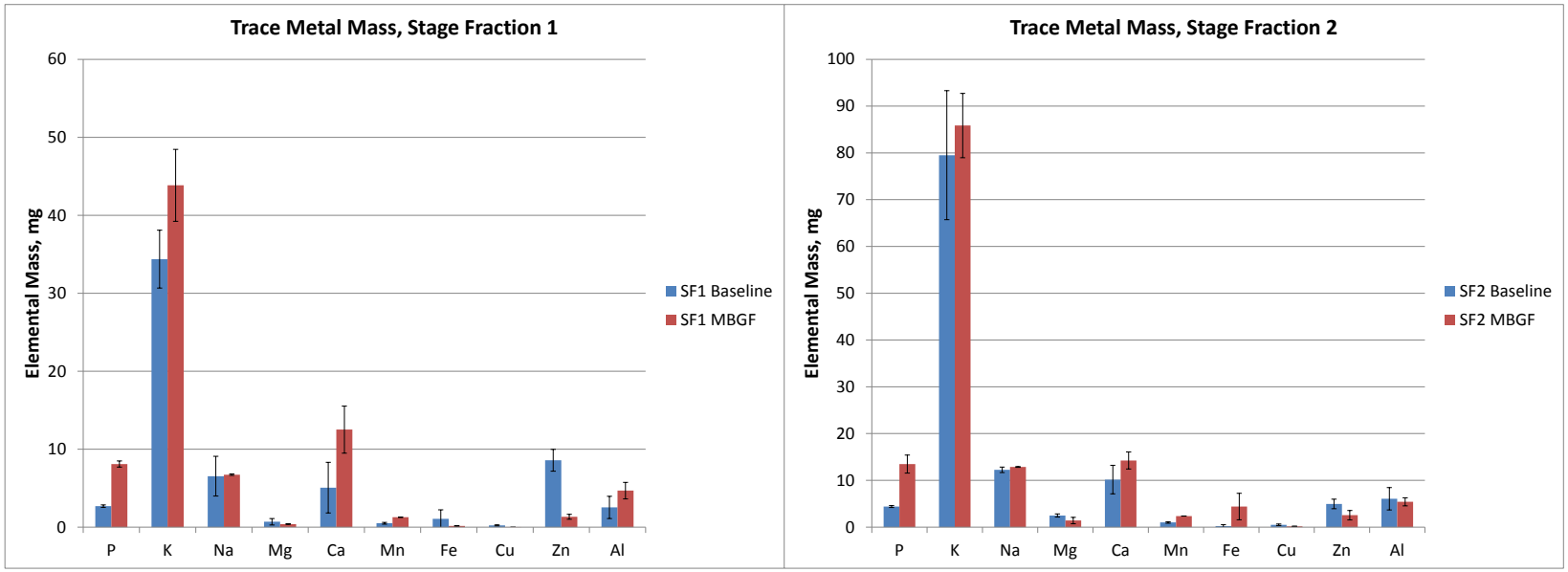

Figure 38: Baseline and MBGF Derived Bio-oil Trace Metal Comparison - SF1 & SF2

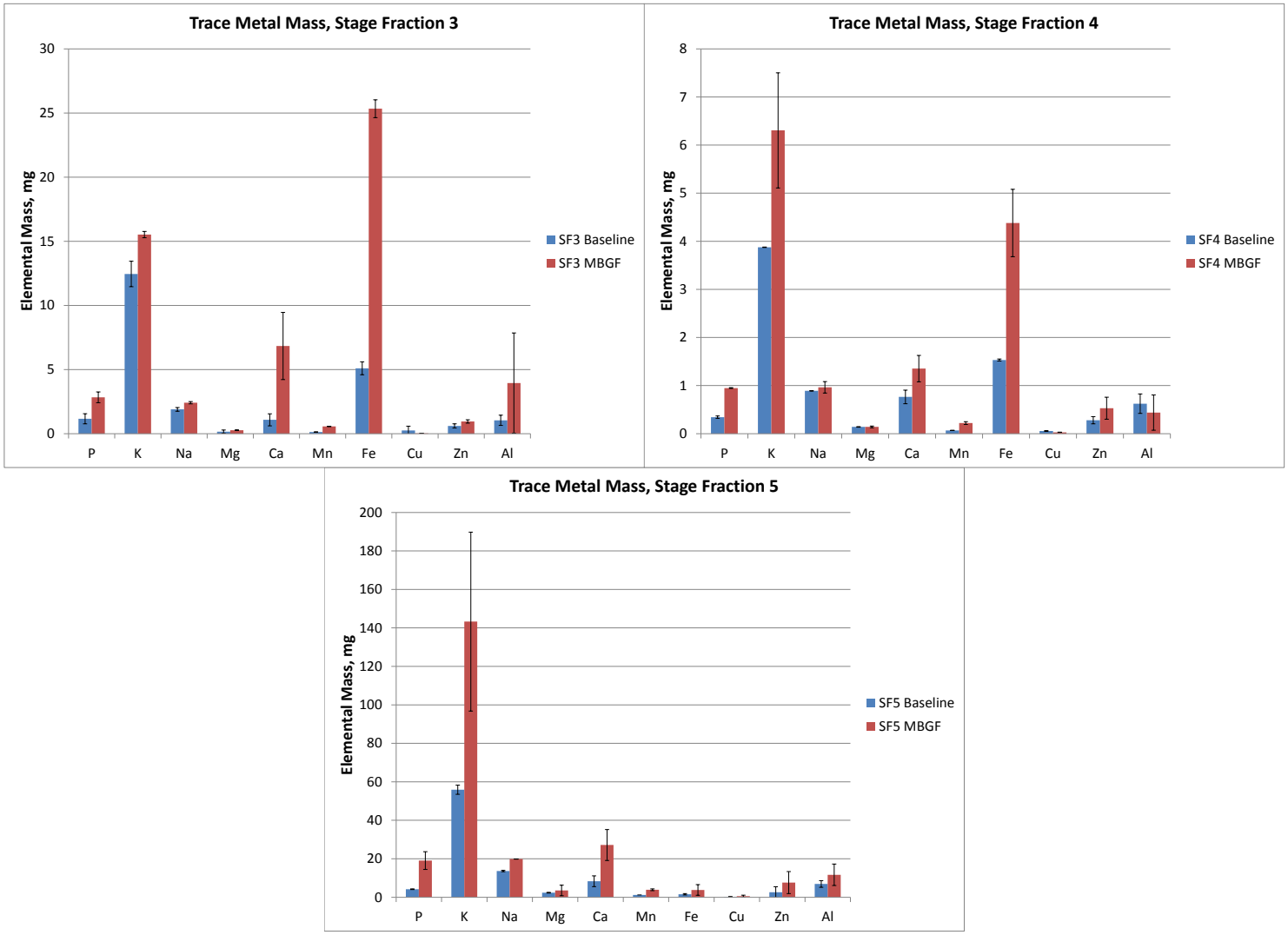

Figure 39: Baseline and MBGF Derived Bio-oil Trace Metal Comparison - SF3, SF4 & SF5

4.9 GPC

Due to the difficulty and inconsistency associated with traditional aging analysis, the most advanced technology available was used to evaluate the effect of bio-oil aging in this study. GPC is able to produce a molecular weight curve for a sample that displays response area vs. molecular weight. This technique can quickly identify the occurrence of bio-oil aging between samples as the area associated with lighter molecules will decrease while the area over larger molecules will increase indicating polymerization has taken place. GPC also produces a set of statistical averages, which can be used to summarize the curve as a single number. These averages include both number averaged and weight averaged molecular weight as well as polydipsersity, which is a ratio between the two. This study will focus on both the comparison of molecular weight distributions and number averaged molecular weights.

The baseline data of each MBGF test was compared to that of PDU baseline operation using the GPC software directly. These graphs plot milli-absorbance units by retention time in minutes resulting in higher molecular weight compounds on the left of the graph and progressively lower molecular weight compounds traversing to the right. By comparing these curves, anomalies in the types of compounds being collected during filtration would be apparent. As shown in Figure 40, no anomalies were present and the PDU baseline curves are nearly identical to that of the MBGF test. This same comparison was made for each granule flow rate tested and no anomalies were found. The details of additional comparisons can be found in APPENDIX G.

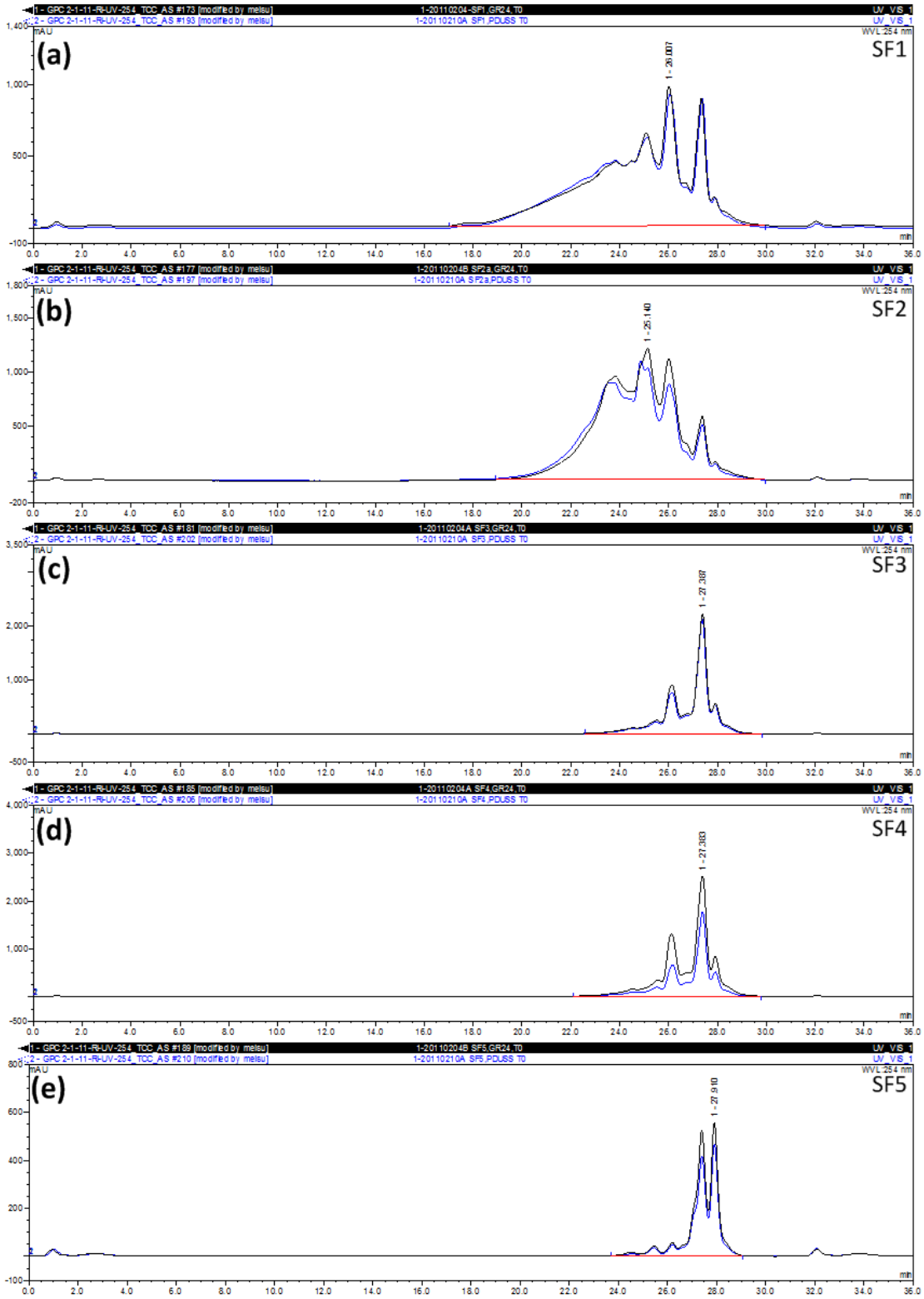

Figure 40: GPC Molecular Weight Curve Comparison between GR24 MBGF and PDU Baseline Operation for a) SF1, b) SF2, c) SF3, d) SF4, and e) SF5

An aging analysis was conducted on oil obtained from two tests performed at each of the granule flow rates. Three 5 g samples were obtained for each stage fraction of oil and aged according to the DOE guidelines. These results were then compared to each other and to a baseline analysis previously performed on the PDU.[44] Each GPC measurement was performed in triplicate to verify results.

Figure 41 displays the results of an aging study conducted previously on the pyrolyzer PDU.[44] As in Figure 8, the amplitude on the y-axis corresponds to the number of constituents in the sample that have the molecular weights shown on the x-axis. The molecular weight curves progress in aging from "TIME 0 HR"(blue) corresponding to bio-oil as collected to "TIME 24 HR"(purple) corresponding to 24 hours of aging at 90°C. In the case of each stage fraction, the peak(s) toward the beginning of the curve associated with lower molecular weight species shrink in response area height as the bio-oil is aged. At the same time, the last peak toward the end of the curve associated with higher molecular weight compounds increases and broadens as the bio-oil is aged. These graphs clearly indicate the occurrence of polymerization reactions in the oil under accelerated aging conditions.

Similar graphs have been generated for results obtained at each of the three tested MBGF granular flow rates. Aging analysis was conducted on two tests run at each granular rate, the results of which are displayed in Figures Figure 42 - Figure 44. Once again, a clear trend of increased higher molecular weight compounds and decreased lower molecular compounds with accelerated aging is present under all MBGF conditions tested.

Each fraction of baseline oil undergoes the majority of the aging process within the first 8 hours. The same conclusion could be drawn about bio-oil stage fractions 1, 2, 4, and 5 obtained from all three MBGF operating conditions tested. In the case of SF3,

polymerization appears to complete after 16 hours of accelerated aging. SF1 bio-oil samples appear to age less under MBGF operating conditions than baseline PDU operation. The lower molecular weight peaks associated with MBGF trials decrease to approximately 8,000 for the first peak and 12,000 for the second. However, baseline oil low molecular weight peaks settle at 5,000 and 8,000 after aging is complete. In all four cases, high molecular weight peaks in the SF1 samples increase to approximately 12,000. Therefore, MBGF SF1 samples appear to undergo a smaller reduction in low molecular weight species than the baseline SF1 sample. A similar trend is observed with SF2 bio-oil samples as the baseline sample decreased to 12,000 and increased to 20,000 for low and high molecular weight species respectively. The MBGF SF2 samples decreased to 14,000 and increased to 17,000 for low and high molecular weight species respectively. SF3 bio-oil ages to the same extent in all four instances, however, bio-oil obtained from MBGF trials does so at a much slower rate, requiring upwards of 16 hours of accelerated aging to reach stable molecular weight levels. No discernable differences between baseline and MBGF bio-oil aging can be determined in the cases of SF4 and SF5.

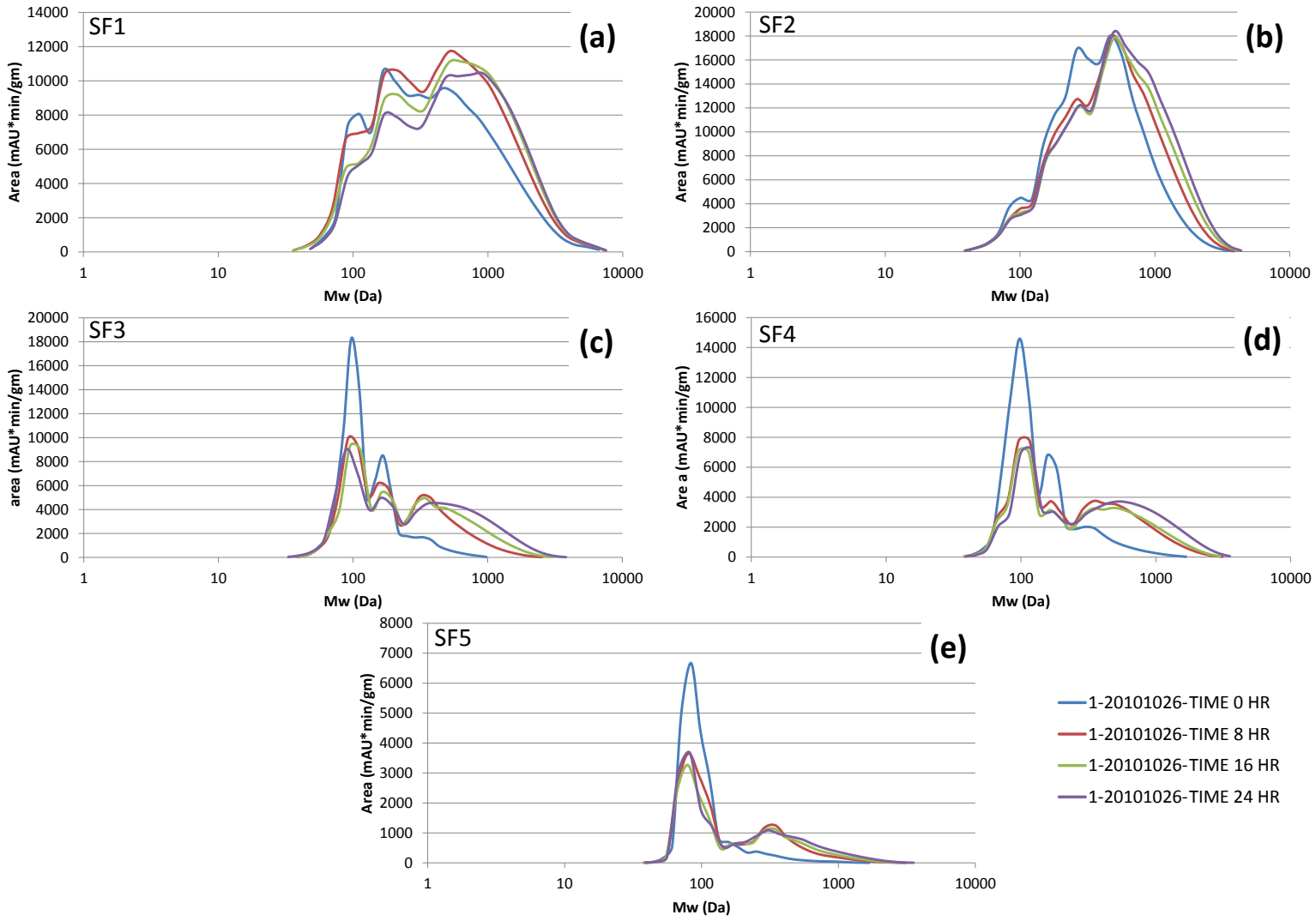

Figure 41: GPC Bio-oil Comparison of PDU Baseline Samples at 0, 8, 16, and 24h Aging Periods for a) SF1, b) SF2, c) SF3, d) SF4, and e) SF5[44]

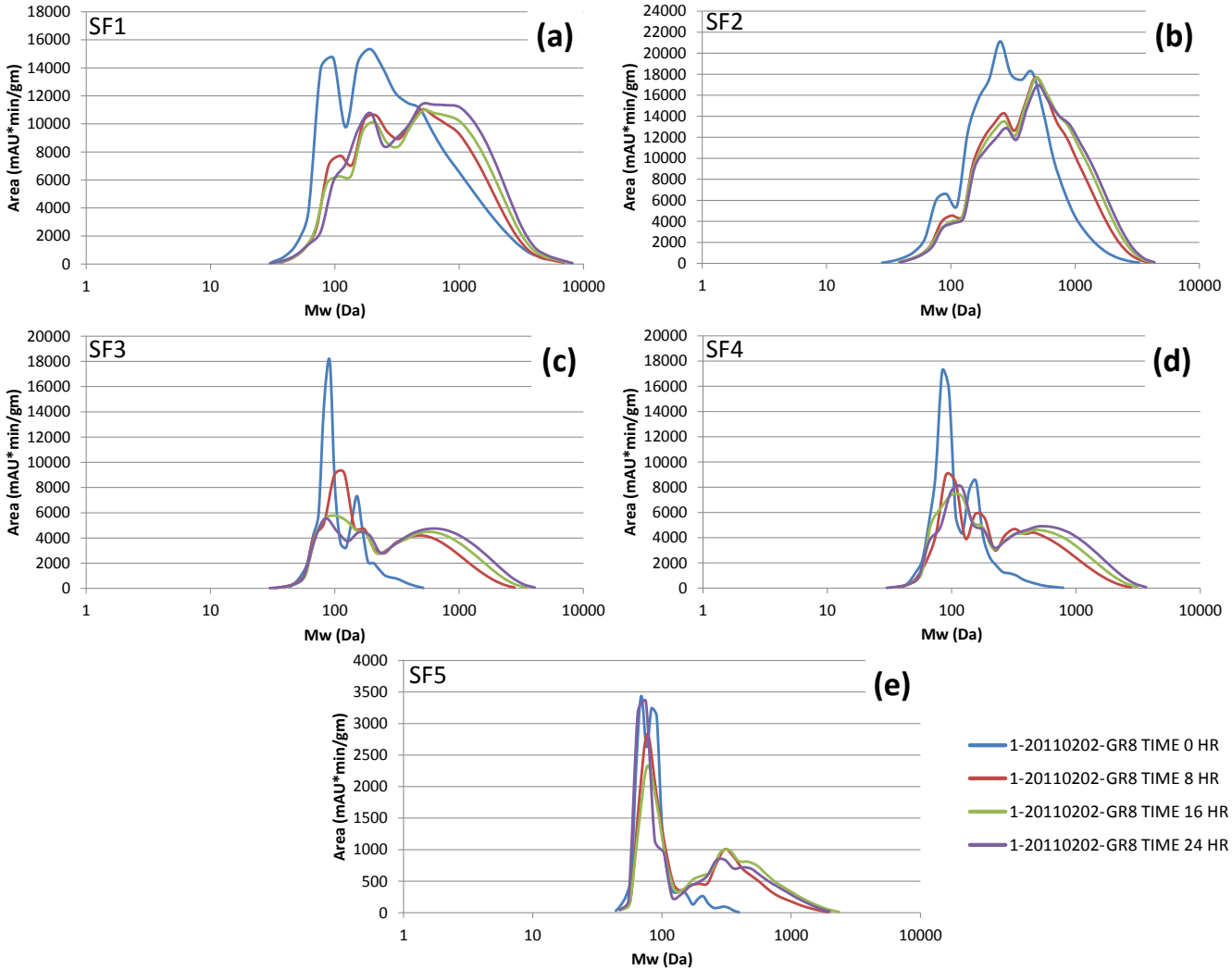

Figure 42: GPC Bio-oil Comparison of MBGF GR8 Samples at 0, 8, 16, and 24h Aging Periods for a) SF1, b) SF2, c) SF3, d) SF4, and e) SF5

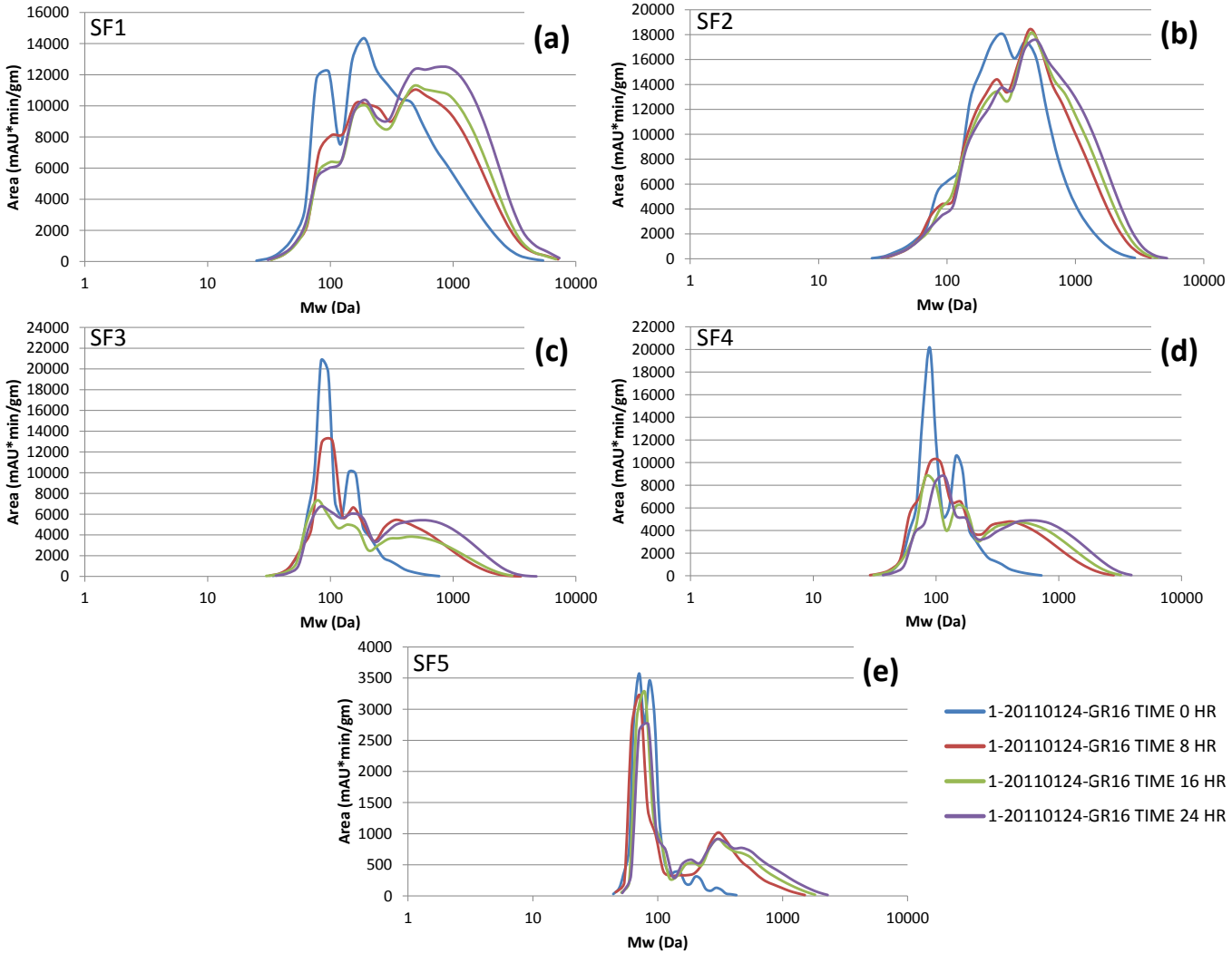

Figure 43: GPC Bio-oil Comparison of MBGF GR16 Samples at 0, 8, 16, and 24h Aging Periods for a) SF1, b) SF2, c) SF3, d) SF4, and e) SF5

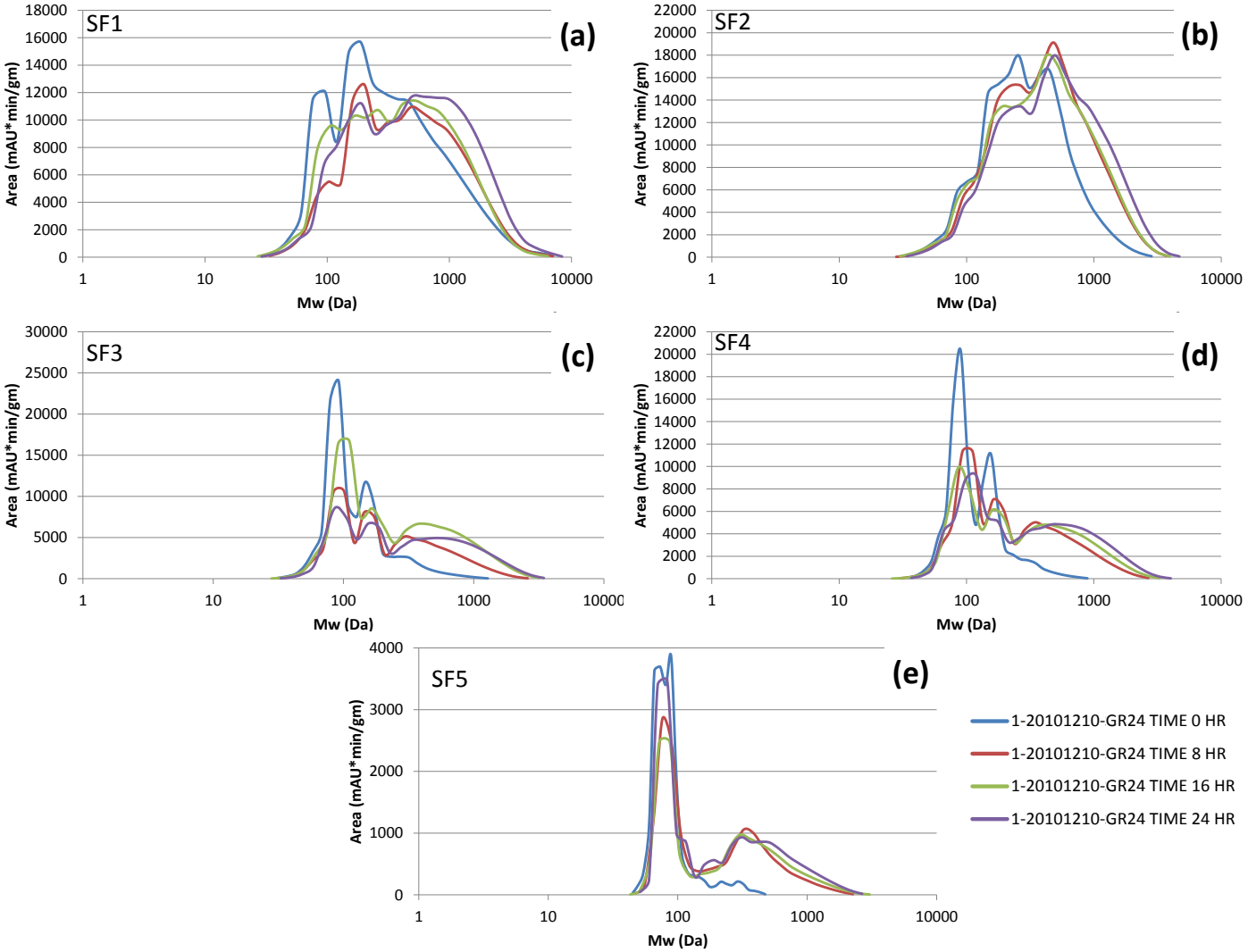

Figure 44: GPC Bio-oil Comparison of MBGF GR24 Samples at 0, 8, 16, and 24h Aging Periods for a) SF1, b) SF2, c) SF3, d) SF4, and e) SF5

To quantify the aging process, the molecular weight distributions from the GPC analyses were converted into number averaged molecular weights as a function of time using the relationship:

Equation 6: Number Averaged Molecular Weight

$$M_n = \frac{\sum_i N_i M_i}{\sum_i N_i}$$

where the products of the molecular weight of molecule *i* is multiplied by the number of molecules of that size, N_i, are summed, then divided by the total number of molecules. Although other kinds of average molecular weight could be calculated, this number averaged value has a close relationship with viscosity through the Mark-Houwink equation.[45] Acid-catalyzed free radical polymerization is expected to follow a second-order reaction model, which can be express as:

Equation 7: Acid-catalyzed Second-Order Reaction Model [46]

$$\frac{M_n(t)}{M_n(t_0)} - 1 = kt$$

where t is time, t_0 is the starting time, and k is the second-order reaction rate constant. This model was used to correlate the four time intervals evaluated for accelerated again trials (0, 8, 16, and 24 hours). These results are shown in Figures Figure 45 - Figure 47. All of the plots show excellent correlations with the two most viscous fractions (SF 1 and 2) generally shown rate constants for polymerization that were half that of the other fractions (SF 3, 4 and 5). This slower rate constant of aging for the viscous fractions may reflect that these samples are already highly oligomerized.

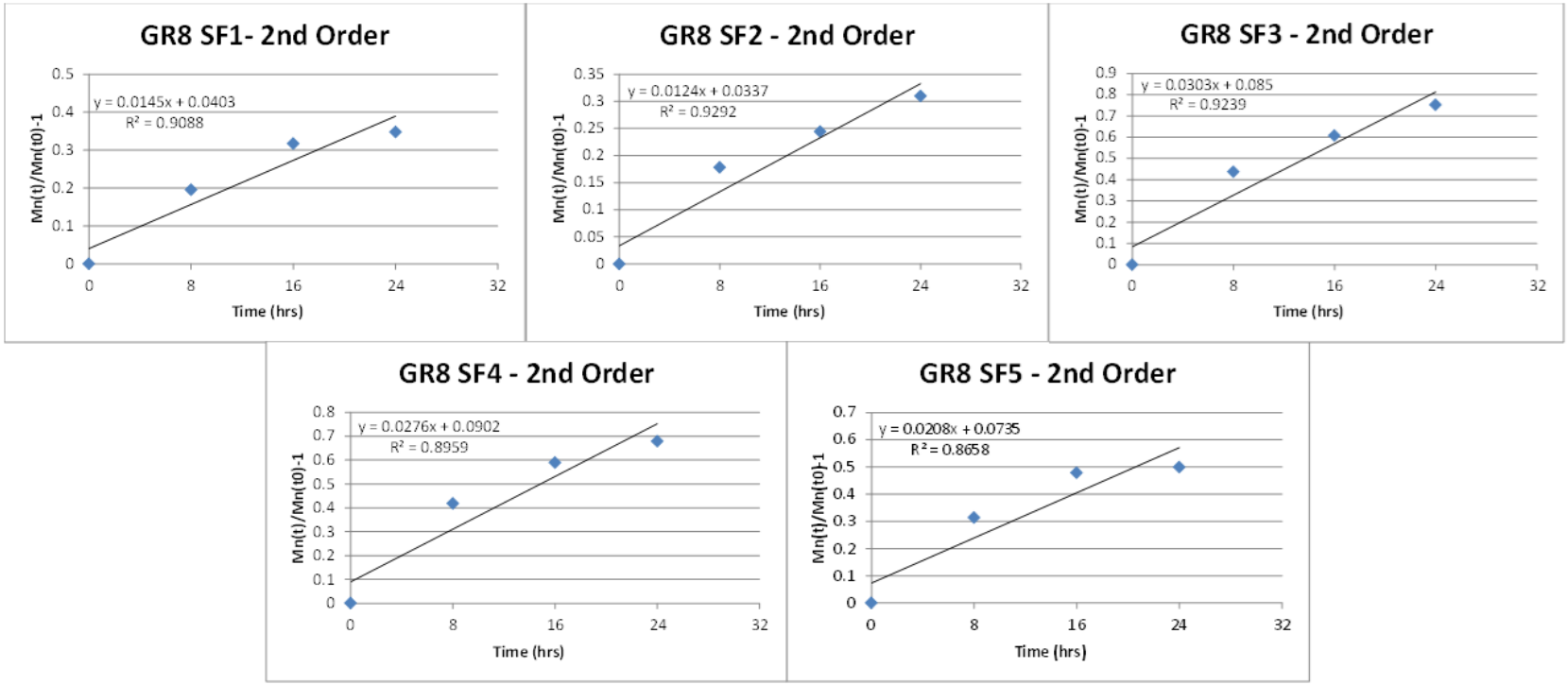

Figure 45: GPC 2nd Order Fitment of Aging Results - GR8

Figure 46: GPC 2nd Order Fitment of Aging Results - GR16

Figure 47: GPC 2nd Order Fitment of Aging Results - GR24

Figure 48 compares the effect of filtration on the rate constants for each stage fraction. The baseline reaction coefficient trends reasonably well with filtration occurring at a granular flow rate of 8 kg/h in the first three fractions. In the fourth and to a greater extent the fifth fraction the baseline reaction rate is greatly reduced. In general, the bio-oil obtained from baseline operating conditions had a lower polymerization reaction coefficient than bio-oil obtained from MBGF operating conditions.

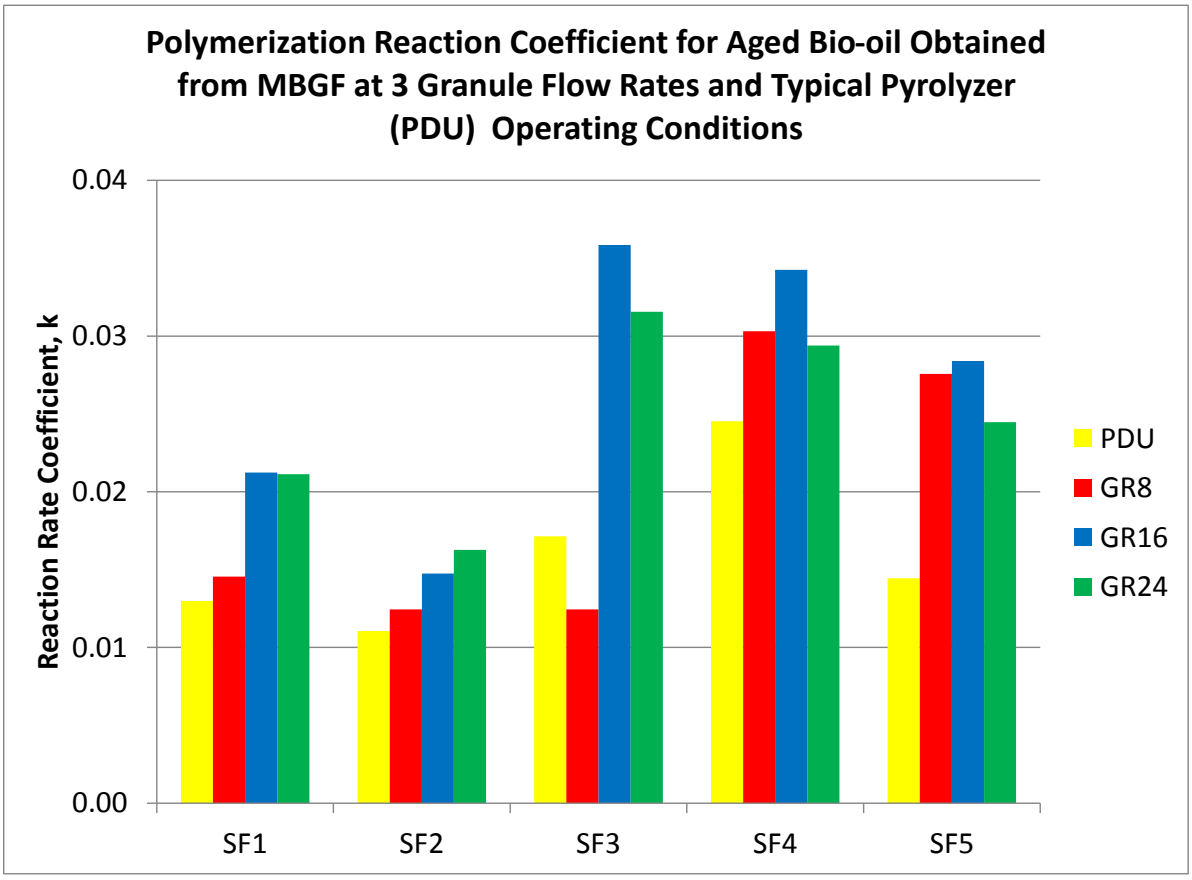

Figure 48: Second Order Polymerization Model Reaction Rate Coefficients for Aged Bio-oil Samples from PDU and MBGF at 3 Granular Flow Rates

CHAPTER 5. CONCLUSIONS

This work has successfully shown the ability to sustainably operate a demonstration scale moving bed granular filter at high temperatures in the presence of a pyrolysis product stream. Limitations on both granular flow rate and operating temperatures exist and have been identified.

5.1 Experimental Conclusions

Pyrolysis operation with the MBGF in-situ resulted in bio-oil that was higher in moisture content suggesting the occurrence of secondary dehydration reactions occurring in the filter. The extent of the moisture increase was dependent on granular flow rate. The presence of the filter had an apparent effect on bio-oil water insoluble content and was also dependent on granular flow rate.

Quantitative measurements with regards to solids removal were difficult to make and inconclusive using traditional methods. However, qualitative analysis by SEM shows no evidence of biomass derived particulate in MBGF derived bio-oil samples, yet shows distinct evidence of its presence in baseline derived oil. SEM analysis also confirms the presence filtration media derived dust in SF1 samples.

SEM analysis confirms the removal of primary char by the MBGF at all tested granular flow rates through examination of the spent filtration media. Additional analysis of SF1 derived bio-oil solids content confirms the presence of filtration media derived dust in

samples obtained at each granular flow rate. Smaller char particles present in bio-oil derived samples appear to have formed after primary pyrolysis during secondary reactions taking place post moving bed granular filtration.

ICP analysis of the baseline and MBGF collected bio-oil indicates that overall trace metal concentrations are not reduced when using the filter in-situ. However, analysis of the filtration media indicated that the same trace metals are present in the media and could contribute to bio-oil contamination through the transport of dust particles elutriating from the filter.

Accelerated bio-oil aging analysis indicates that all bio-oil samples collected with the MBGF in-situ experienced some degree of aging. This phenomenon could be a result of the presence of alkali metal remaining in the bio-oil product stream due to filtration media derived dust contamination. Additional polymerization reaction modeling indicates that bio-oil obtained from MBGF operation had a larger reaction coefficient than bio-oil obtained from baseline operation.

5.2 Future Work

Several areas of improvement for MBGF operation have been identified as a result of this work. A simple geometry change resulting in a larger surface area at the exit of the filter would eliminate the elutriation of larger filtration media derived dust which collects in SF1. This change should help facilitate more accurate bio-oil solids content measurements in future MBGF derived samples. The change to a less frangible filtration media would reduce grinding in the transport augers and eliminate the creation of very fine dust particles that

eventually contaminate collected bio-oil. The use of an inert filter media, such as glass beads or crushed granite, would eliminate the media as a source of trace metal contamination and allow mass balances on alkali partitioning occurring within the pyrolysis process. The incorporation of a recycling loop with the ability to remove carbonaceous residue from the media through combustion would decrease the amount of media needed for testing and reduce the amount of heat input required to operate the system. Future moving bed granular filtration work should include the application of these solutions and possible progression to the addition of rugged, deoxygenation catalysts to the filtration media.

CHAPTER 6. BIBLIOGRAPHY

1. Bridgwater, A.V., *BIOMASS FAST PYROLYSIS.* Thermal Science, 2004. **8**(2): p. 21-49.
2. Brown, R.C., *Biorenewable Resources : Engineering New Products from Agriculture*. 1st ed2003, Ames, Iowa: Iowa State Press. xii, 286 p.
3. Graham, R.G., M.A. Bergougnou, and R.P. Overend, *Fast pyrolysis of biomass.* Journal of Analytical and Applied Pyrolysis, 1984. **6**(2): p. 95-135.
4. Friedlander, S.K., *Smoke, Dust, and Haze*. 2nd ed, ed. N.C.S.U. Keith E. Gubbins2000, New York: Oxford University Press. 407.
5. Hinds, W.C., *Aerosol technology: properties, behavior, and measurement of airborne particles*. 2nd ed1998: Wiley-Interscience. Medium: X; Size: Pages: 483.
6. Brown, R.C., *Air Filtration: An Integrated Approach to the Theory and Applications of Fibrous Filters*1993. 272.
7. Tien, C., *Granular filtration of aerosols and hydrosols*. Butterworths series in chemical engineering1989, Boston: Butterworths. xii, 365 p.
8. Saxena, S.C., R.F. Henry, and W.F. Podolski, *Particulate removal from high-temperature, high-pressure combustion gases.* Progress in Energy and Combustion Science, 1985. **11**(3): p. 193-251.
9. Willeke, K., X. Lin, and S.A. Grinshpun, *Improved Aerosol Collection by Combined Impaction and Centrifugal Motion.* Aerosol Science and Technology, 1998. **28**(5): p. 439 - 456.
10. Bridgwater, A.V., D. Meier, and D. Radlein, *An overview of fast pyrolysis of biomass.* Organic Geochemistry, 1999. **30**(12): p. 1479-1493.
11. Daugaard, D.E. and R.C. Brown, *The transport phase of pyrolytic oil exiting a fast fluidized bed reactor*, in *Science in Thermal and Chemical Biomass Conversion Conference*2004: Victoria, B.C., Canada.
12. Klauser, N., *Independent Study of Electrostatic Precipitator*, D.R. Brown, Editor 2003, Iowa State university: Nevada, Ia. p. 38.
13. Pollard, A.J.S., *ESP Bio-oil Yields Fluidized Bed Fast Pyrolyzer BECON Research Facility*, L. Whitmer, Editor 2007, Iowa State University: Nevada.
14. Pollard, A.J.S., *Comparison of bio-oil produced in a fractionated bio-oil collection system*, in *Mechanical Engineering*2009, Iowa State University: Ames.
15. Garcia-Perez, M., et al., *Characterization of bio-oils in chemical families.* Biomass and Bioenergy, 2007. **31**(4): p. 222-242.
16. Patwardhan, P.R., *Understanding the Product Distribution from Biomass Fast Pyrolysis* in *Chemical Engineering*2010, Iowa State University: Ames. p. 119.
17. Diebold, J.P., *A Review of the Chemical and Physical Mechanisms of the Storage Stability of Fast Pyrolysis Bio-Oils*, S. Czernik, Editor 2000, Thermalchemie, Inc.: Lakewood, Colorado.
18. Agblevor, F.A. and D.K. Johnson. *Pyrolysis char catalyzed destabilization of biocrude oils*. in *AIChE National Meeting*. 1997.
19. Scahill, J., J.P. Diebold, and C. Feik, *Removal of residual char fines from pyrolysis vapors by hot gas filtration.* Fuel and Energy Abstracts, 1998. **39**(4): p. 286-286.

20. Fahmi, R., et al., *The effect of lignin and inorganic species in biomass on pyrolysis oil yields, quality and stability.* Fuel, 2008. **87**(7): p. 1230-1240.
21. Bridgwater, A.V. and G.V.C. Peacocke, *Fast pyrolysis processes for biomass.* Renewable and Sustainable Energy Reviews, 2000. **4**(1): p. 1-73.
22. Diebold, J.P. and S. Czernik, *Additives To Lower and Stabilize the Viscosity of Pyrolysis Oils during Storage.* Energy & Fuels, 1997. **11**(5): p. 1081-1091.
23. Czernik, S., D.K. Johnson, and S. Black, *Stability of wood fast pyrolysis oil.* Biomass and Bioenergy, 1994. **7**(1-6): p. 187-192.
24. Whitelock, D.P. and M.D. Buser, *Preliminary results of a series cyclone test*, in *ASABE Annual International Meeting*2005.
25. Agblevor, F.A. and S. Besler, *Inorganic Compounds in Biomass Feedstocks. 1. Effect on the Quality of Fast Pyrolysis Oils.* Energy & Fuels, 1996. **10**(2): p. 293-298.
26. WHEELDON, #160, and J. M., *Hot flue gas filtration experience at the Power Systems Development Facility*. Vol. 20. 2003, St Albans, ROYAUME-UNI: Science Reviews. 10.
27. Kang, B.-S., et al., *Fast pyrolysis of radiata pine in a bench scale plant with a fluidized bed: Influence of a char separation system and reaction conditions on the production of bio-oil.* Journal of Analytical and Applied Pyrolysis, 2006. **76**(1-2): p. 32-37.
28. Hoekstra, E., et al., *Fast Pyrolysis of Biomass in a Fluidized Bed Reactor: In Situ Filtering of the Vapors.* Industrial & Engineering Chemistry Research, 2009. **48**(10): p. 4744-4756.
29. Chen, J.-Y., et al., *Removal of Char Fines from Biomass Fast Pyrolysis Vapors by Moving Granular Bed Filter*, in *The 13th Asia Pacific Confederation of Chemical Engineering Congress*2010, APCChe: Taipei.
30. Nunez, J.S., *Evaluation of a Moving Bed Filter in Conjunction with a Biomass Gasifier*, in *Mechanical Engineering*2002, Iowa State University: Ames. p. 45.
31. Abatzoglou, N., M. Gagnon, and E. Chornet, *Cold and hot gas filtration using a novel mobile granular bed with an inner fluidized section.* Canadian Journal of Chemical Engineering, 2002. **80**(1): p. 17-27.
32. Ritzert, J.A., *Factors Influencing the Efficiency of a Moving Bed Granular Filter*, in *Mechanical Engineering*2004, Iowa State University: Ames. p. 75.
33. Soo, S.-C., *Empirical Model Optimization of a Moving Bed Granular Filter for Particulate Removal*, in *Mechanical Engineering*2002, Iowa State University: Ames. p. 65.
34. Huisenga, M.D., *Experimental Assessment of the Efficiency of a Moving Bed Granular Filter Using a Single Particle Counter*, in *Energy Technology*2006, Royal Institute of Technology: Stockholm, Sweden. p. 51.
35. Shi, H., *Similitude modeling and experiments on a moving bed granular filter*, in *Mechanical Engineering*2002, Iowa State University: Ames.
36. Brown, R.C., et al. *Design of a moving bed granular filter for biomass gasification*. in *Proceeding of the Progress in Thermochemical Biomass Conversion Conference*. 2000. Tyrol, Austria.

37. Hedok, I.E., *Moving Bed Granular Filtration of Pyrolysis Char: Granular Flow Rate Study*, in *Chemical & Biological Engineering*2009, Iowa State University: Ames. p. 66.
38. Scholze, B. and D. Meier, *Characterization of the water-insoluble fraction from pyrolysis oil (pyrolytic lignin). Part I. PY-GC/MS, FTIR, and functional groups.* Journal of Analytical and Applied Pyrolysis, 2001. **60**(1): p. 41-54.
39. Sadula, S. and R.C. Brown, *Iowa State University, personal communication*, 2010: Ames.
40. *Biomass Fast Pyrolysis Oil (Bio-oil) Stabilization*, D.o. Energy, Editor 2008: Golden, Colorado. p. 33.
41. Czernik, S. *Storage of Biomass Pyrolysis Oils*. in *Biomass Pyrolysis Oil Properties and Combustion Meeting*. 1994. Estes Park, Colorado.
42. Piskorz, J., P. Majerski, and D. Radlein, *Pyrolysis of Biomass - Aerosol Generation: Properties, Applications, and Significance for Process Engineers*, in *Biomass Conference of the Americas*1999: Oakland, California.
43. Jendoubi, N., et al., *Inorganics distribution in bio oils and char produced by biomass fast pyrolysis: The key role of aerosols.* Journal of Analytical and Applied Pyrolysis. **In Press, Corrected Proof**.
44. Olthoff, A. and R.C. Brown, *Effect of Reactor Temperature on Stability and Quality of Fractionated Bio-Oil*, 2011, Iowa State University: Ames.
45. Hiemenz, P.C. and T. Lodge, *Polymer chemistry*. 2nd ed2007, Boca Raton: CRC Press. xvii, 587 p.
46. Odian, G.G., *Principles of polymerization*. 4th ed2004, Hoboken, N.J.: Wiley-Interscience. xxiv, 812 p.
47. Incropera, F.P., *Fundamentals of heat and mass transfer*. 6th ed2007, Hoboken, NJ: John Wiley. xxv, 997 p.
48. Ellens, C., *Design, optimization and evaluation of a free-fall biomass fast pyrolysis reactor and its products*, 2009, Iowa State University: United States -- Iowa. p. 155.

APPENDIX A : PADDLE AUGER TEST RESULTS

Figure 49: Paddle Auger Test Rig

In order to answer questions arising from the experimental paddle auger design for the heating auger, a section was constructed and tested to confirm the auger's ability to reliably flow material. However, due to a malfunctioning VFD unit, the auger could not be tested at the designed rotational speed and had to be tested at 60 Hz or 20 rpm. Recalculating the flow rate of the auger design at this rotational speed yielded a value of 340 kg/hr. The flow rate of the test rig averaged 390 kg/hr, a value within 15% of the design speed. Performing a student's t analysis on the data set yielded a p-value < 0.0001, indicating no statistically significant differences between test points. The auger was able to flow sufficient material in standard configuration while still allowing for additional flow capacity using the adjustment of the pitch of the paddles to push along more or less of the material.

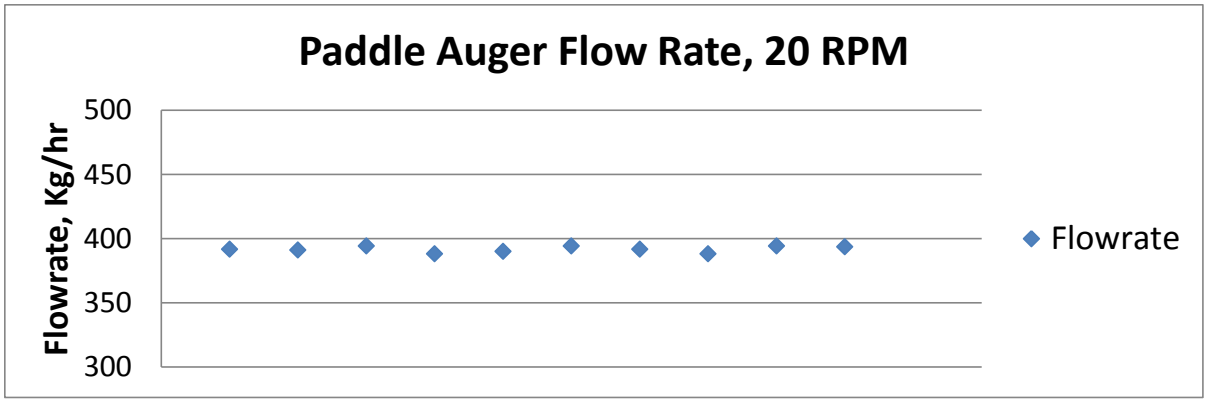

Figure 50: Paddle Auger Flow Rate

APPENDIX B : HEATED AUGER TEST RESULTS

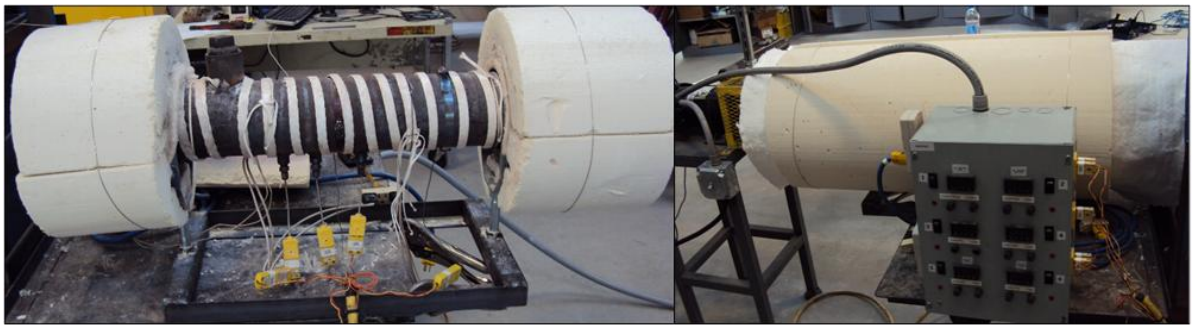

Figure 51: Heated Auger Test Rig

In order to ensure adequate sizing of the heat transfer surface of the heating auger, a second test rig was constructed in order to determine some properties of the filtration media as well as geometric and mixing effects on heating rate. While a convection coefficient determination was deemed most appropriate for the paddle auger conveyance geometry, it was decided that a conduction based heat transfer calculation would be the most conservative and therefore selected as the first method to determine the heating rate of the system.

The test rig, pictured in Figure 51, was constructed using a 20.3 cm long section of 15.2 cm nominal schedule 40 pipe of carbon steel construction. The end caps were constructed using 15.2 cm black iron pipe caps with a 2.5 cm center hole bored in each. A shortened section of the paddle auger described in APPENDIX A was centered in the pipe using the holes in the end caps and retained using a removable pinch collar on either end. Three pipe threaded half couplings were welded to the bottom of the pipe to act as thermocouple ports and were located such that they would not interfere with the auger paddles. Heat was provided to the system using three research grade heat tapes and a heat

control box with the ability to control 6 zones. The reactor was divided into 2 control zones as depicted in the schematic of the experimental setup shown in Figure 52.

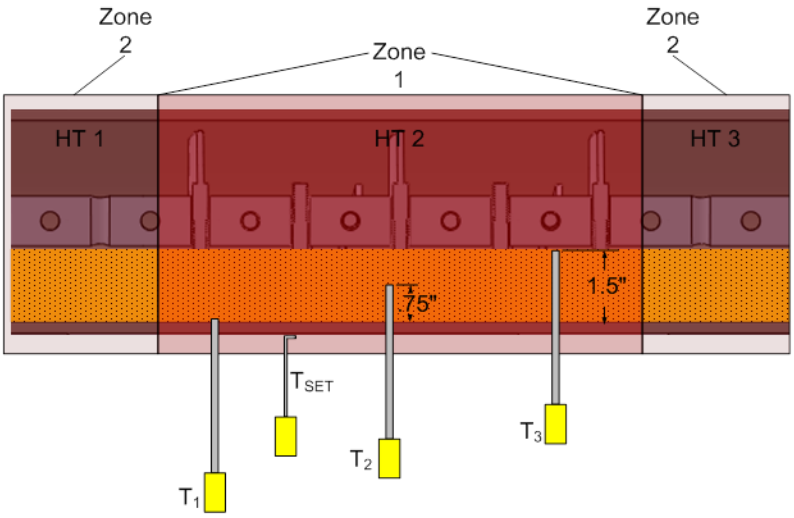

Figure 52: Heating Auger Conduction Test Rig

Zone 1 was used to provide the main heating to the media whose temperature is being monitored while zone 2 was independently controlled to help eliminate the end effects of the pipe caps. The power (watts) provided to each zone was also metered using a standard household appliance power meter for a 120VAC circuit. The pipe was filled to fifty percent capacity, the level at which the final auger system should operate. A combination of calcium silicate and Kaowool™ blanket insulation was used to provide over 15 cm of insulation to the reactor.

Equation 8: Fourier Equation for Cylindrical Geometry [47]

$$q_r = \frac{2\pi Lk(T_{s,1} - T_{s,2})}{ln\left(\frac{r_2}{r_1}\right)}$$

The three thermocouples were inserted into the media at various depths in order to calculate the temperature difference between known thicknesses of the material. A pure Fourier's law calculation was then used to back out the thermal conductivity of the granule filtration media using Equation 8 for the temperature differences between both T_1-T_2 and T_2-T_3. This calculation yielded values in the range of 3-18 W/m*K over the testing period and is shown in Figure 53.

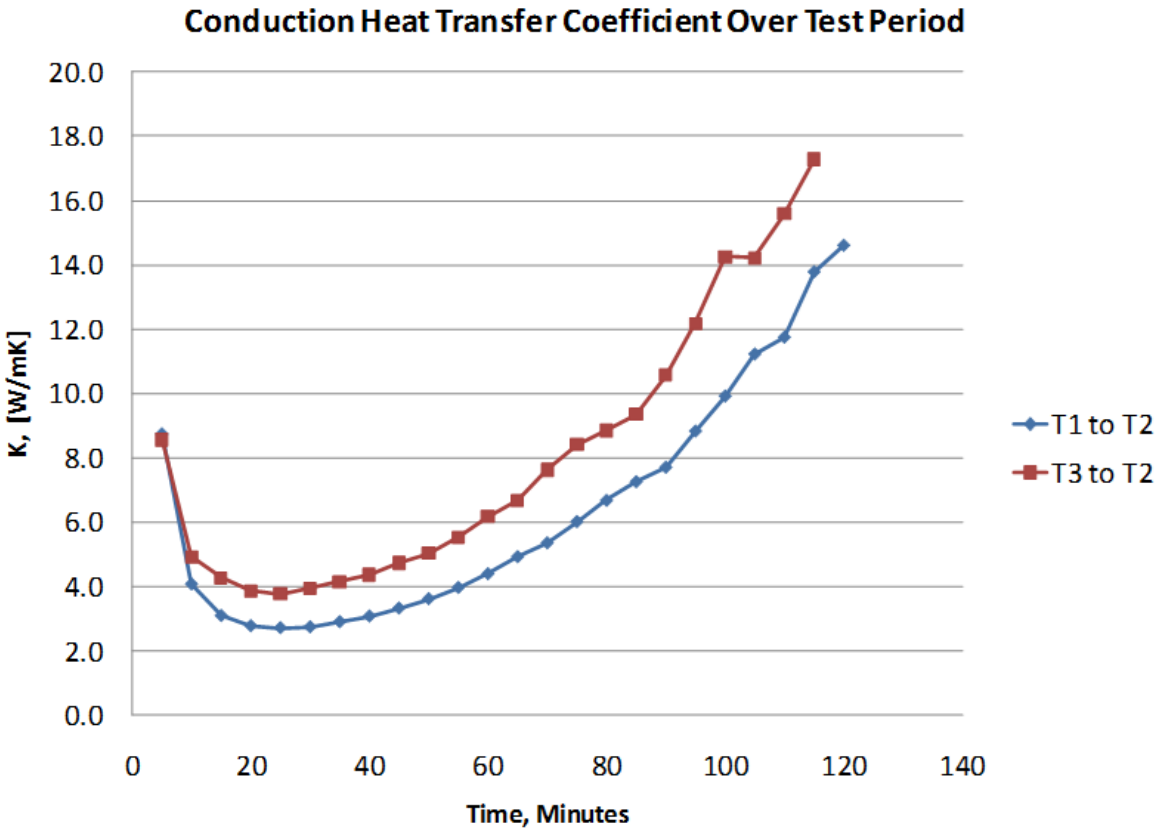

Figure 53: Fourier's Law K Value Calculation Results

However, this approach is flawed due to the apparent transient conduction occurring in the setup. Transient conditions would help to explain the large range of conduction

coefficient values calculated from the test data, as the Fourier equation assumes steady state operation.

The setup was modified to allow movement of filtration media through the reactor with the addition of an inlet and outlet pipes on the top and bottom of the pipe as depicted in Figure 54. The thermocouples were also modified to read temperature at the same depth transversely across the reactor. A fourth thermocouple was added to monitor outlet temperature.

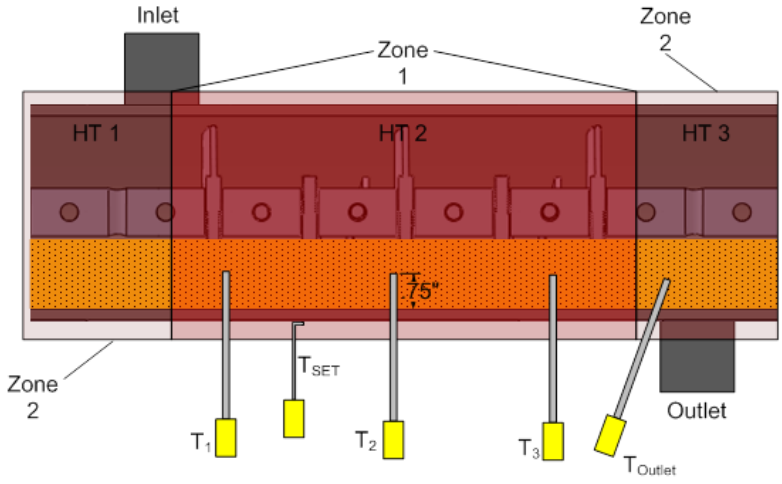

Figure 54: Heating Auger Test Rig Schematic

In this test the static system (no material flowing) was allowed to heat to 500°C before the granular flow was turned on and temperatures monitored. The resulting temperature curves are displayed in Figure 55.

A transient slab analysis was performed on the system during initial startup of the paddle auger in order to back out an average convection heat transfer coefficient between the spinning paddle auger and the heated reactor wall. First a Fourier number was calculated

based on the experimental conditions and the time elapsed since the auger began to move granular material according to the following equation:

Equation 9: Fourier Number, Adapted from Eqn. 5.12 [47]

$$Fo \equiv \frac{\alpha t}{r_o^2} \quad and \quad \alpha = \frac{k}{\rho c_p}$$

where t is the time since the transient system was initiated, r_o is the characteristic length of a cylinder, α is the thermal diffusivity as defined, ρ and c_p are the density and the heat capacity of the filtration media, and k is the thermal conductivity as defined from the analysis above and taken at its lowest value. In addition the dimensionless temperature distribution was calculated according to Equation 10.

Equation 10: Dimensionless Temperature Distribution, Adapted from Eqn. 5.31 [47]

$$\theta^*_{Exp} = \frac{(T - T_\infty)}{(T_i - T_\infty)}$$

where T is the experimental temperature recorded from thermocouple T_1, T_i is initial system temperature of 500C, and T_∞ is the ambient temperature. Once the Fourier number and the experimental value of θ^* were known, the approximate solution to the temperature distribution was matched to the experimental solution by varying the coefficients (ζ, C_1 found in Table 5.1 for an infinite cylinder, [47]) in Equation 11.

Equation 11: Dimensionless Temperature Distribution Approximate Solution, Adapted from Eqn. 5.40a [47]

$$\theta^*_{Approx} = C_1 exp(-\zeta_1^2 Fo)\cos(\zeta_1 r^*)$$

With the proper coefficients defined, the corresponding Biot number was read from the table, allowing the convective heat transfer coefficient to be calculated according to Equation 12.

Equation 12: Biot Number, Adapted from Eqn. 5.10 [47]

$$h = \frac{Bi\ k}{r_o}$$

The resulting calculated convective heat transfer coefficients ranged from 10-27 W/m^2*K. The inconsistency of this analysis left much to desire and an alternate approach was sought.

A second analysis was performed on the reactor after it had reached steady-state operating conditions as indicated by a leveling off of temperatures within the reactor. The convective heat transfer coefficient was calculated using the following equation:

Equation 13: Convective Heat Transfer Coefficient, Adapted from Eqn. 6.12 [47]

$$\bar{h} = \frac{\bar{Q}_{In} - \bar{Q}_{Loss}}{(T_E - T_\infty)\pi r_o L}$$

where $\bar{h}$ is the average convective heat transfer coefficient, $\bar{Q}_{In}$ is the average heat energy input into the heat tapes measured by the power monitor, $\bar{Q}_{Loss}$ is the heat energy lost to the atmosphere through the insulation, T_e is the exit temperature of granular media, T_∞ is the ambient air temperature, r_o is the outside radius of the pipe, and L is the length between the pipe inlet and outlet. Convective heat transfer was only assumed to occur on the bottom half of the cylindrical pipe. The resulting convective heat transfer coefficient had a consistent value of 29 W/m^2*K and was consistent with the higher values calculated in the transient slab analysis. Using this new convective coefficient, the desired output temperature of 500C, and the required heat input of 2700 watts for a 20 kg/h granular flow rate (see APPENDIX

D) the required length of the reactor was calculated to be 1.13 meters. With a general convective heat transfer coefficient determined, a more detailed analysis could be conducted which included additional conductive losses and radiation heat transfer effects.

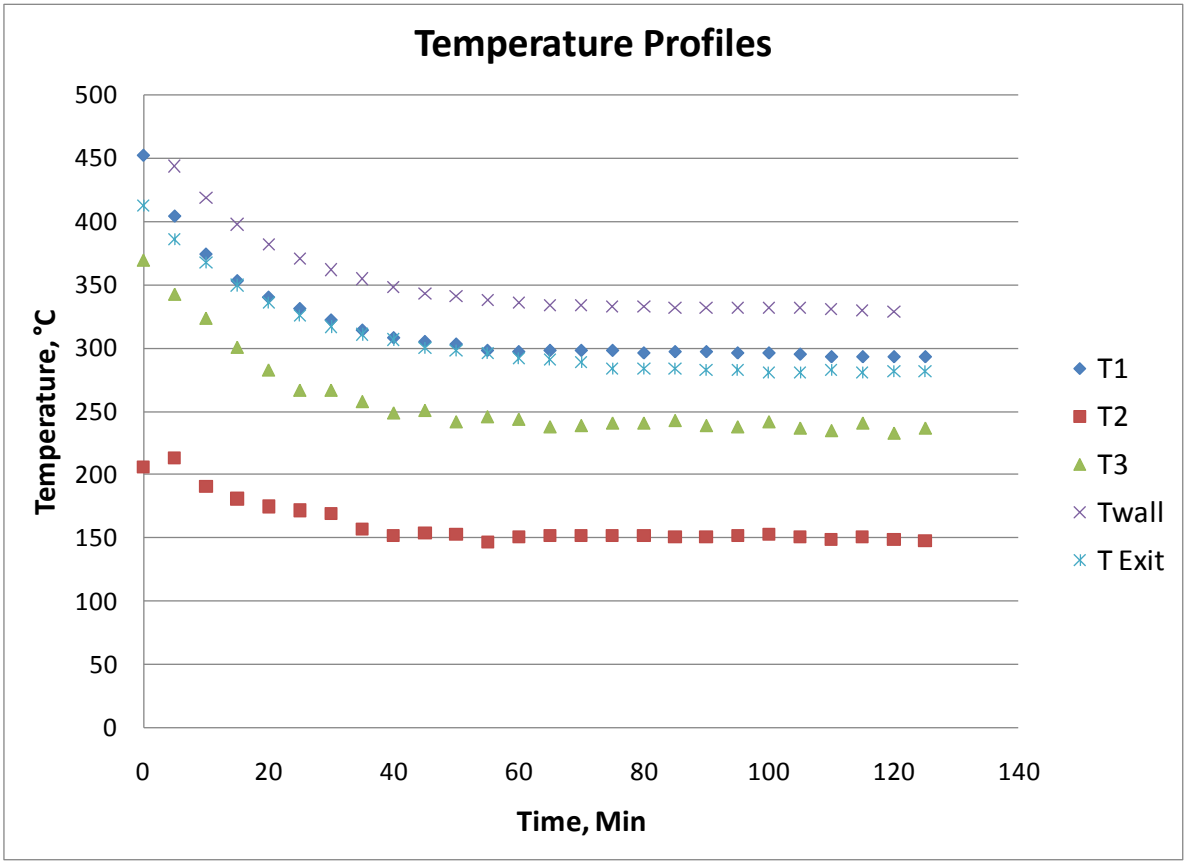

Figure 55: Heating Auger Test Rig Temperature Profiles

APPENDIX C : MBGF DESIGN DRAWINGS

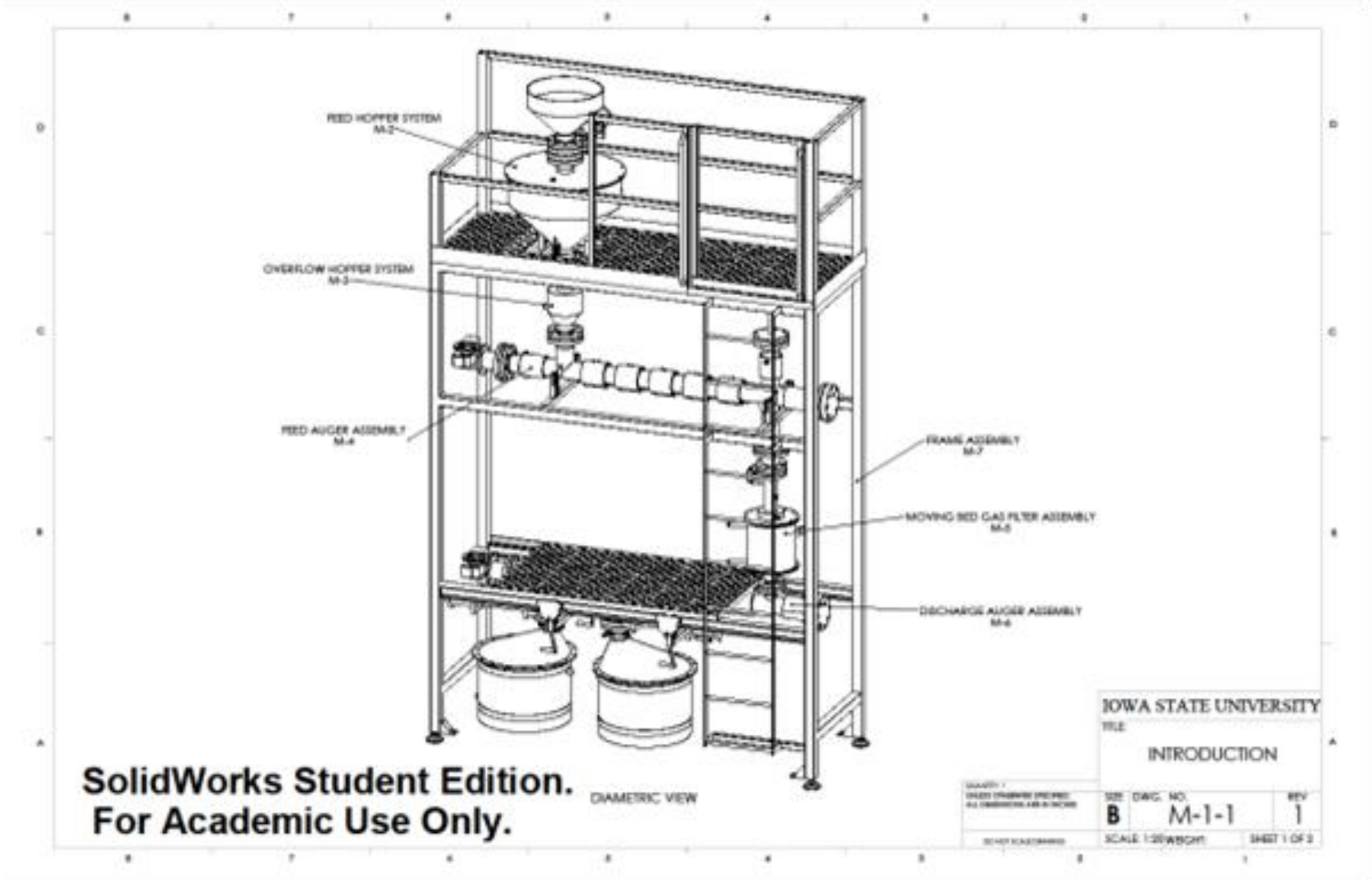

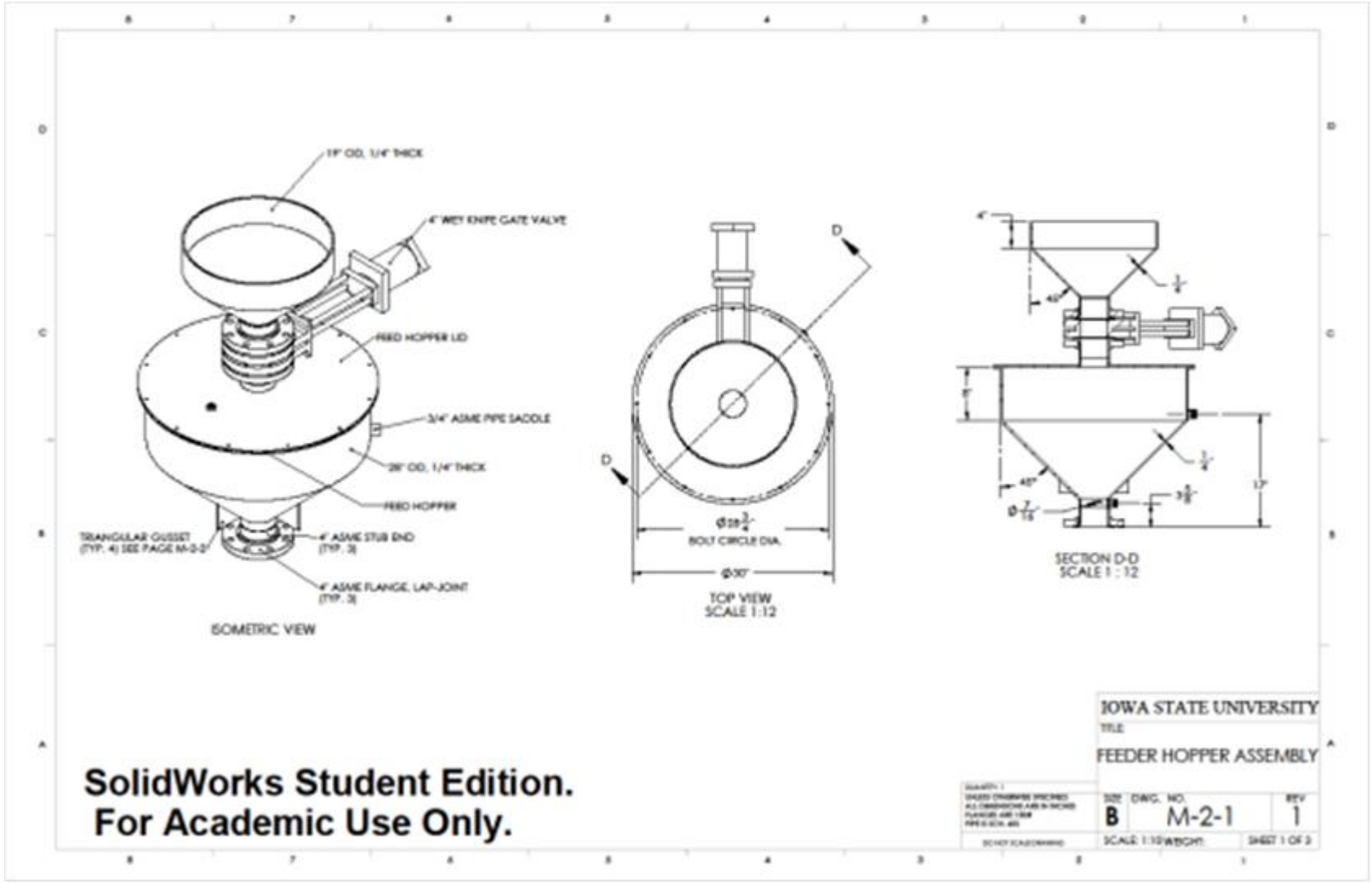

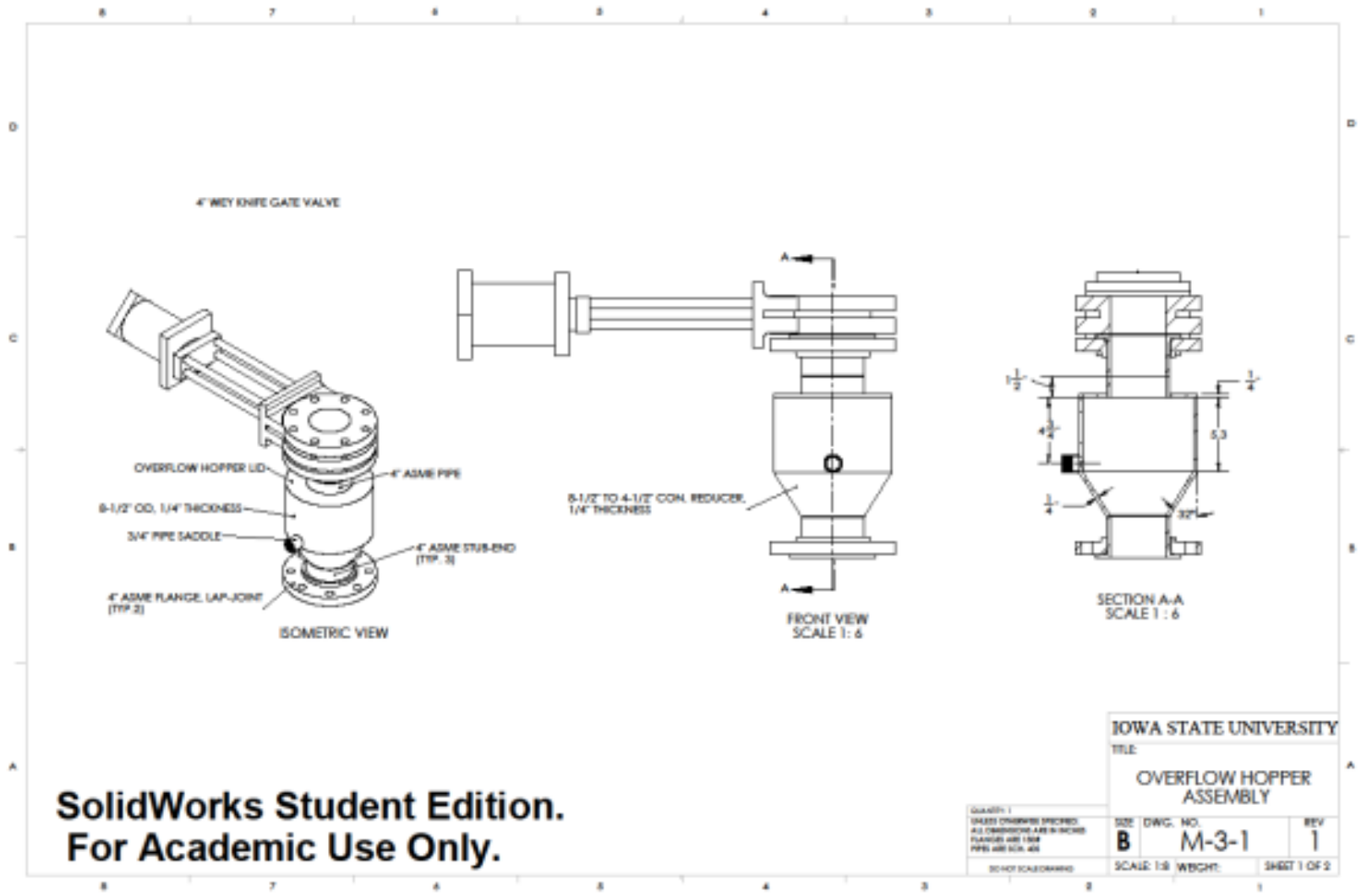

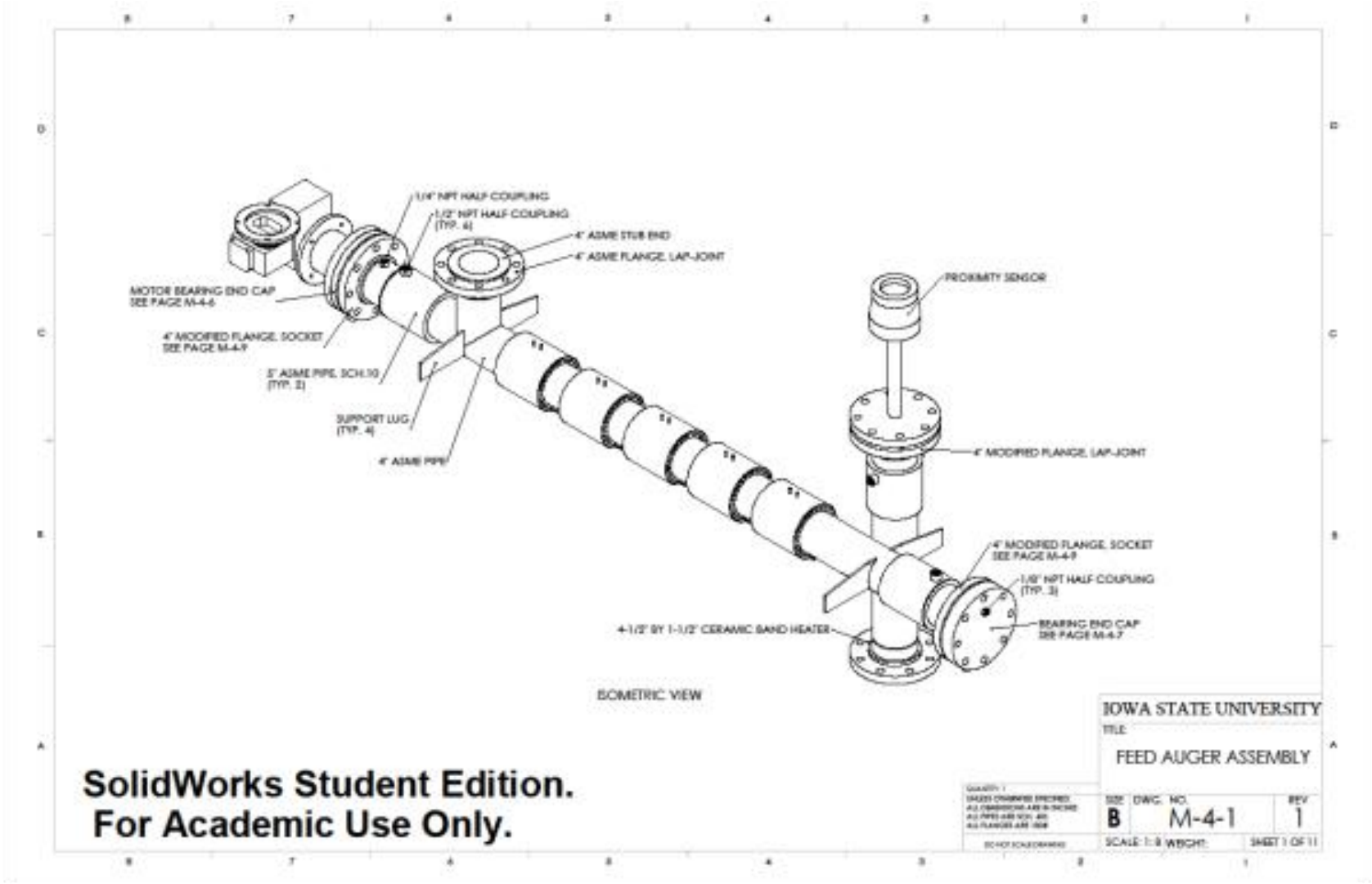

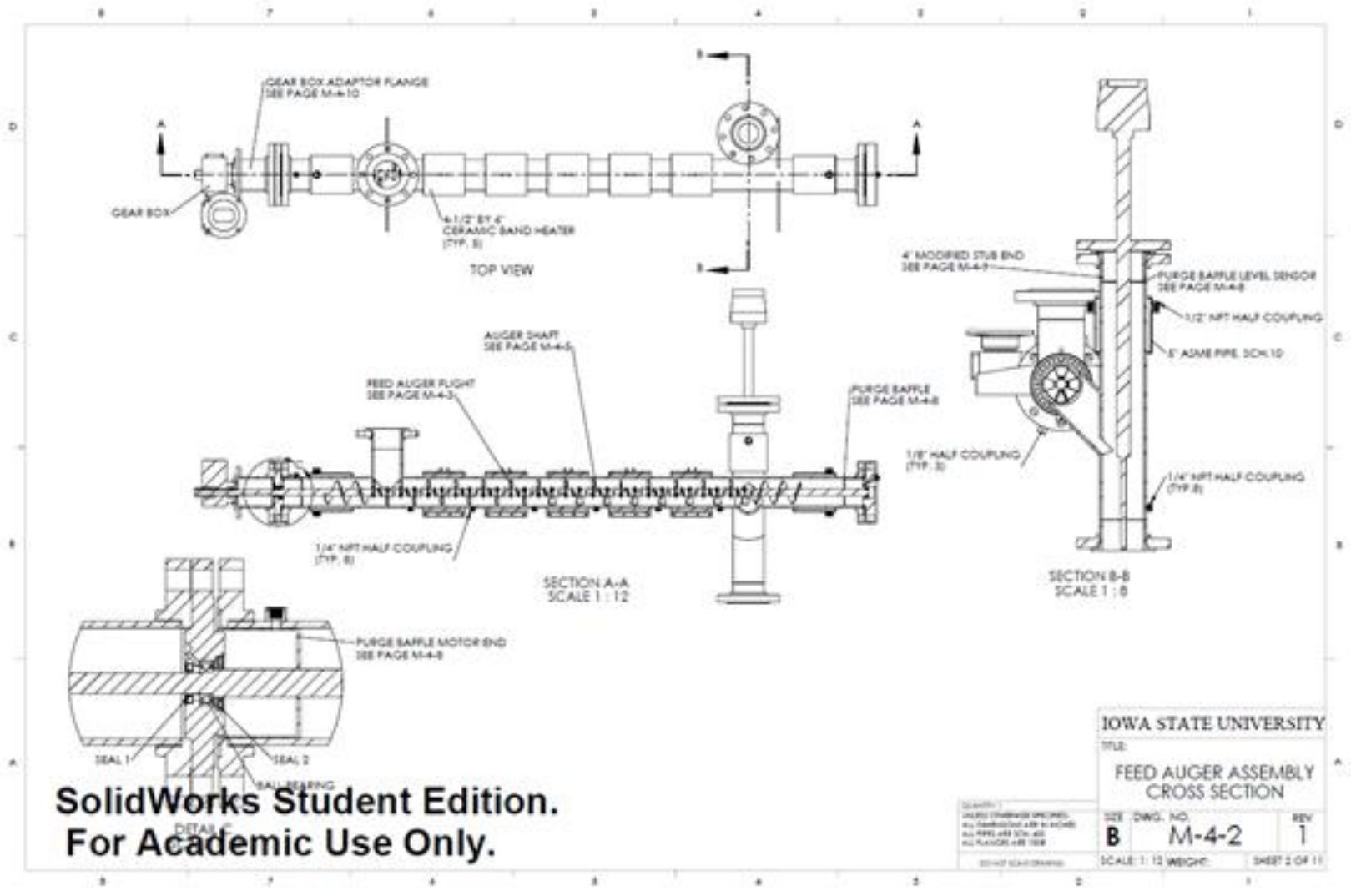

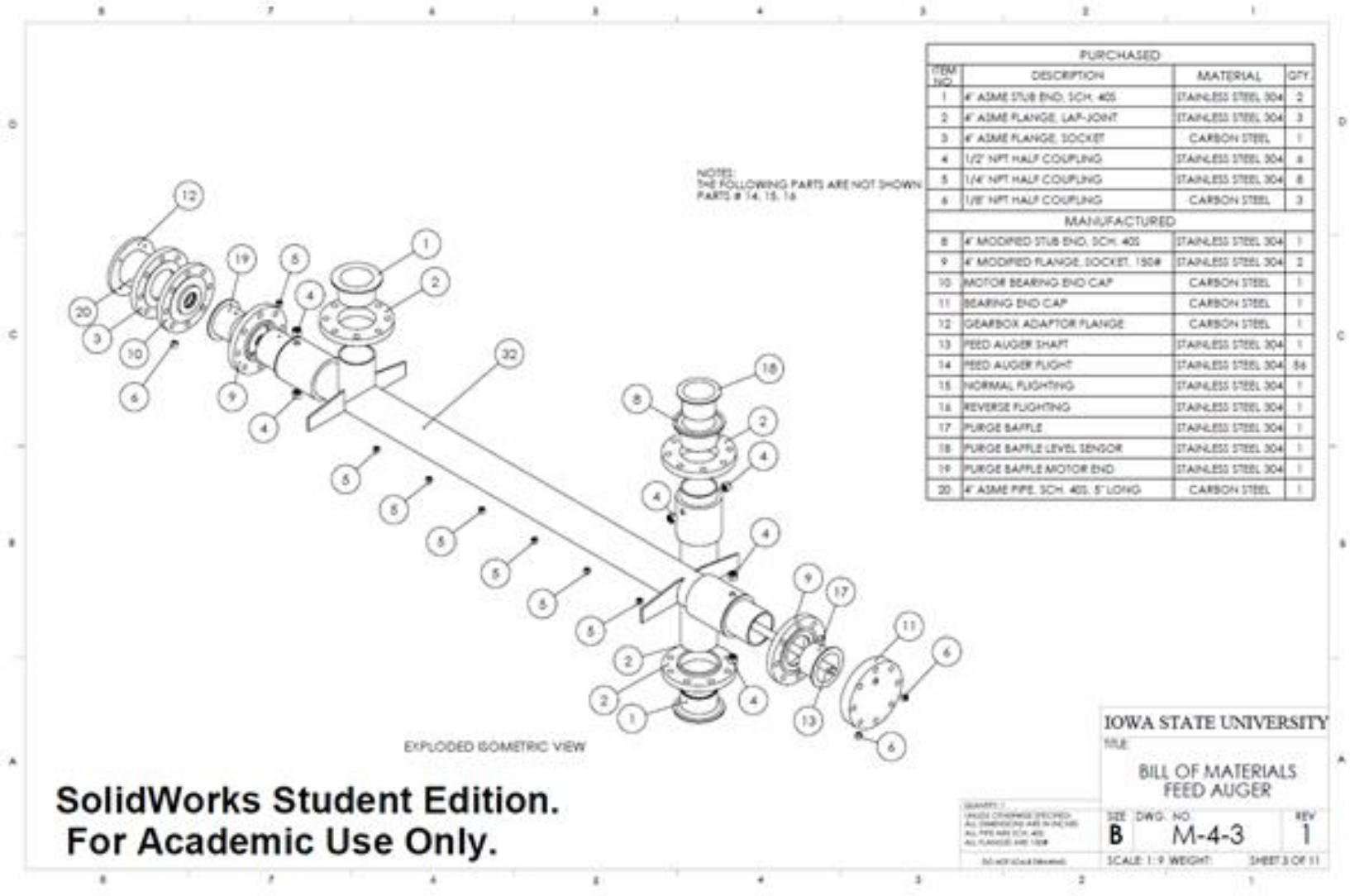

PURCHASED			
ITEM NO.	DESCRIPTION	MATERIAL	QTY.
1	4" ASME STUB END, SCH. 40S	STAINLESS STEEL 304	2
2	4" ASME FLANGE, LAP-JOINT	STAINLESS STEEL 304	3
3	4" ASME FLANGE, SOCKET	CARBON STEEL	1
4	1/2" NPT HALF COUPLING	STAINLESS STEEL 304	6
5	1/4" NPT HALF COUPLING	STAINLESS STEEL 304	8
6	1/8" NPT HALF COUPLING	CARBON STEEL	3
MANUFACTURED			
8	4" MODIFIED STUB END, SCH. 40S	STAINLESS STEEL 304	1
9	4" MODIFIED FLANGE, SOCKET, 150#	STAINLESS STEEL 304	2
10	MOTOR BEARING END CAP	CARBON STEEL	1
11	BEARING END CAP	CARBON STEEL	1
12	GEARBOX ADAPTOR FLANGE	CARBON STEEL	1
13	FEED AUGER SHAFT	STAINLESS STEEL 304	1
14	FEED AUGER FLIGHT	STAINLESS STEEL 304	56
15	NORMAL FLIGHTING	STAINLESS STEEL 304	1
16	REVERSE FLIGHTING	STAINLESS STEEL 304	1
17	PURGE BAFFLE	STAINLESS STEEL 304	1
18	PURGE BAFFLE LEVEL SENSOR	STAINLESS STEEL 304	1
19	PURGE BAFFLE MOTOR END	STAINLESS STEEL 304	1
20	4" ASME PIPE, SCH. 40S, 5" LONG	CARBON STEEL	1

IOWA STATE UNIVERSITY

TITLE: BILL OF MATERIALS FEED AUGER

SIZE	DWG. NO.	REV
B	M-4-3	1

SCALE: 1 : 9 WEIGHT: SHEET 3 OF 11

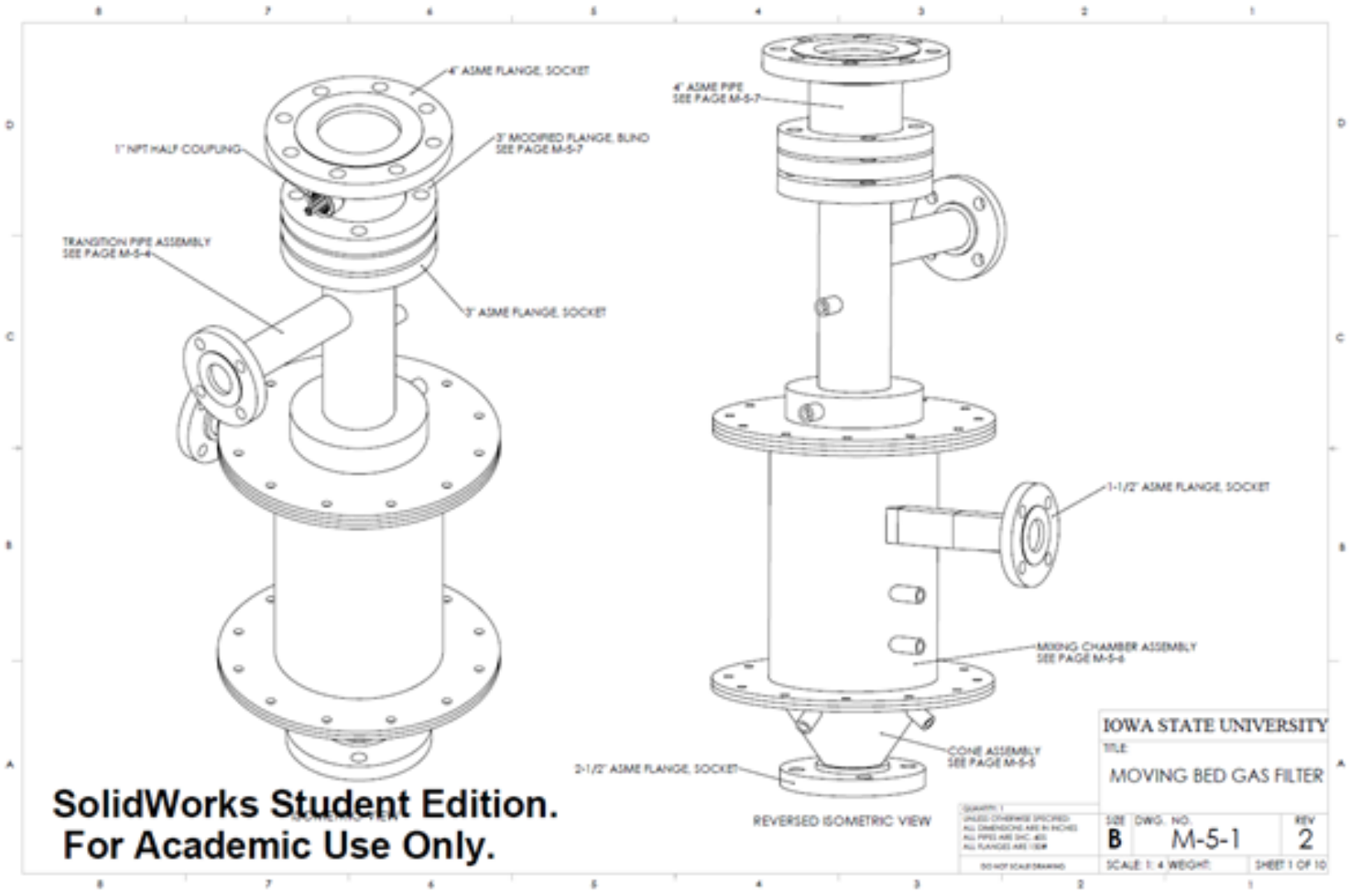

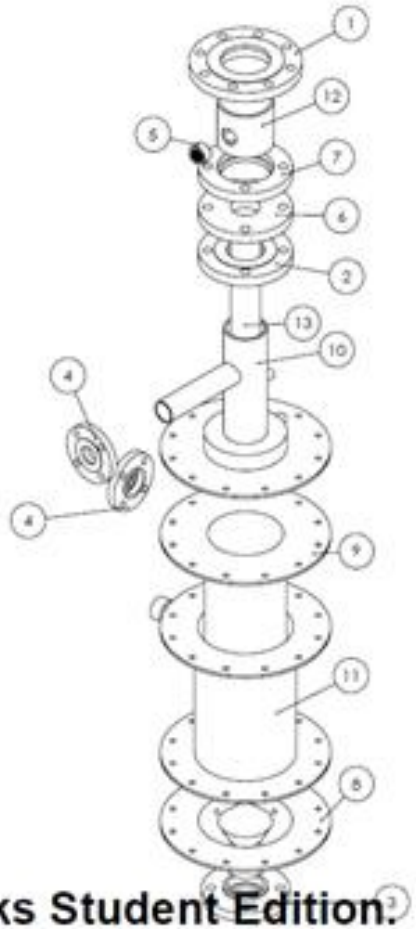

PURCHASED			
ITEM NO.	DESCRIPTION	MATERIAL	QTY.
1	4" ASME FLANGE, SOCKET, 150#	STAINLESS STEEL 304	1
2	3" ASME FLANGE, SOCKET, 150#	STAINLESS STEEL 304	1
3	2-1/2" ASME FLANGE, SOCKET, 150#	STAINLESS STEEL 304	1
4	1-1/2" ASME FLANGE, SOCKET, 150#	STAINLESS STEEL 304	2
5	1" NPT HALF COUPLING	STAINLESS STEEL 304	1
MANUFACTURED			
6	TRANSITION SLEEVE FLANGE	STAINLESS STEEL 304	1
7	3" MODIFIED FLANGE, BLIND, 150#	STAINLESS STEEL 304	1
8	CONE ASSEMBLY	STAINLESS STEEL 304	1
9	DOWNCOMER SLEEVE	STAINLESS STEEL 304	1
10	TRANSITION PIPE ASSEMBLY	STAINLESS STEEL 304	1
11	MIXING CHAMBER ASSEMBLY	STAINLESS STEEL 304	1
12	4" ASME PIPE, SCH. 40S, 4" LONG	STAINLESS STEEL 304	1
13	2" ASME PIPE, SCH. 40S,10-1/4" LONG	STAINLESS STEEL 304	1

IOWA STATE UNIVERSITY

TITLE

BILL OF MATERIALS
MOVING BED GAS FILTER

SIZE	DWG. NO.	REV
B	M-5-3	2

SCALE: 1:8 WEIGHT: SHEET 3 OF 10

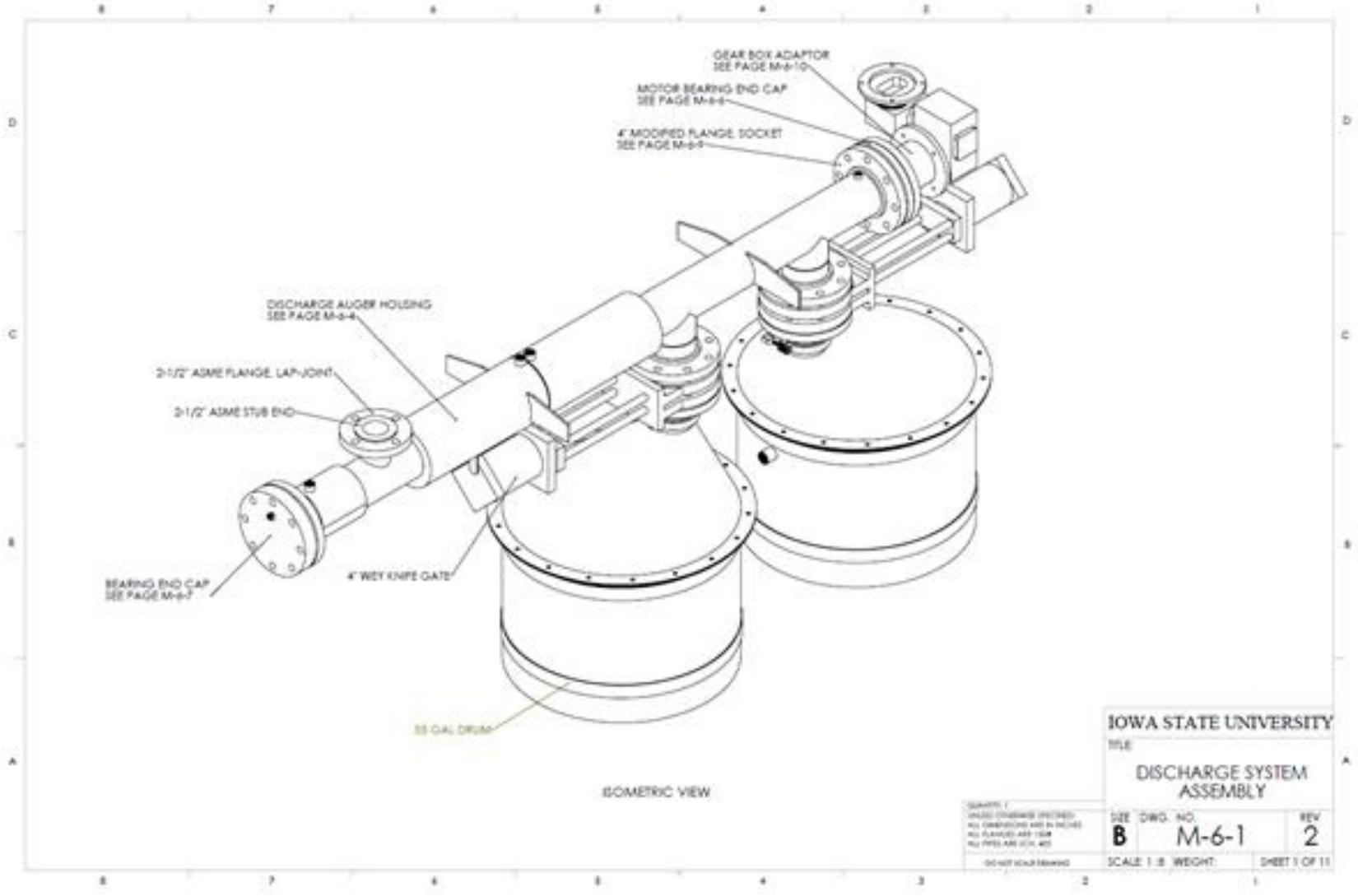

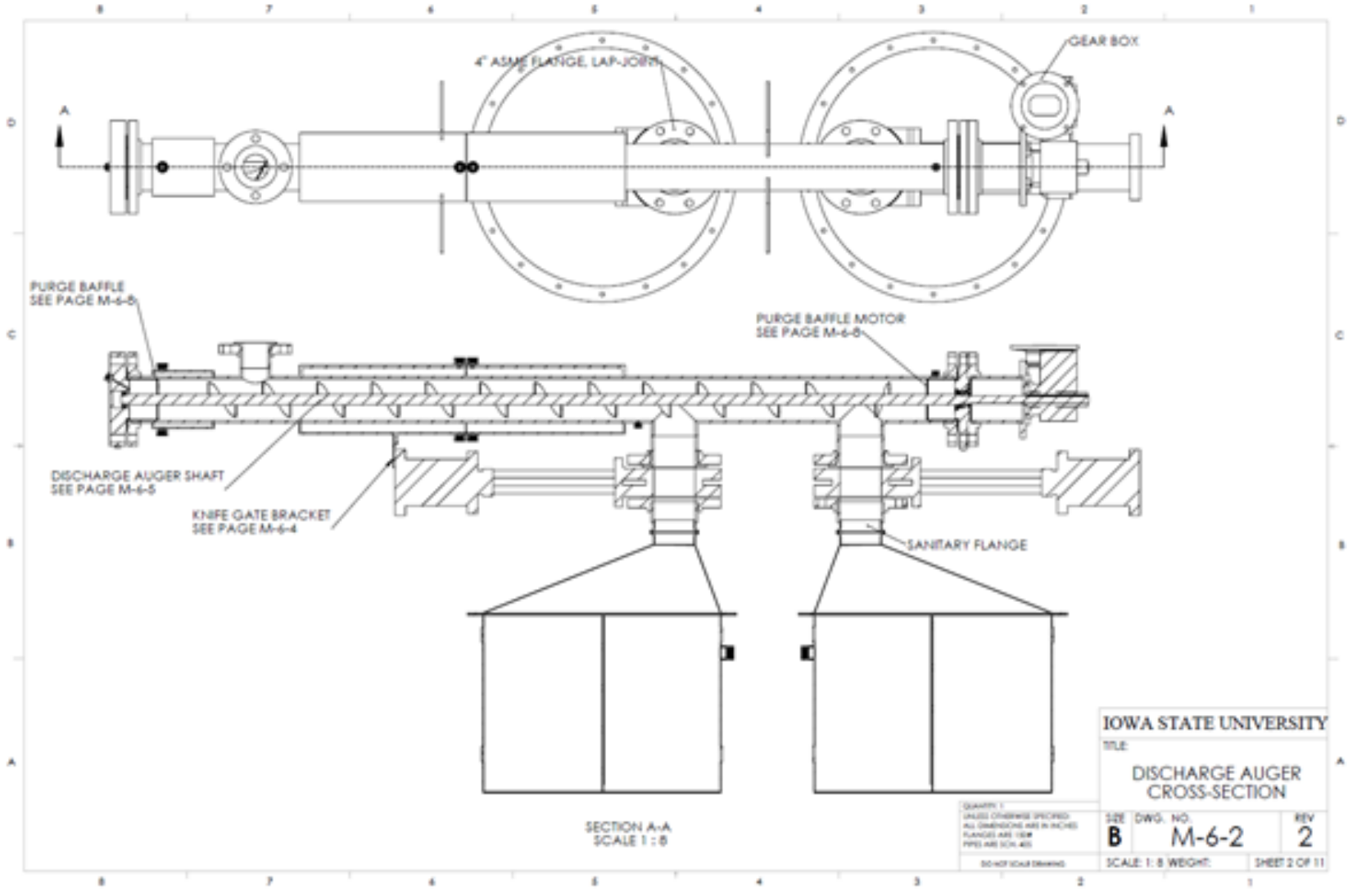

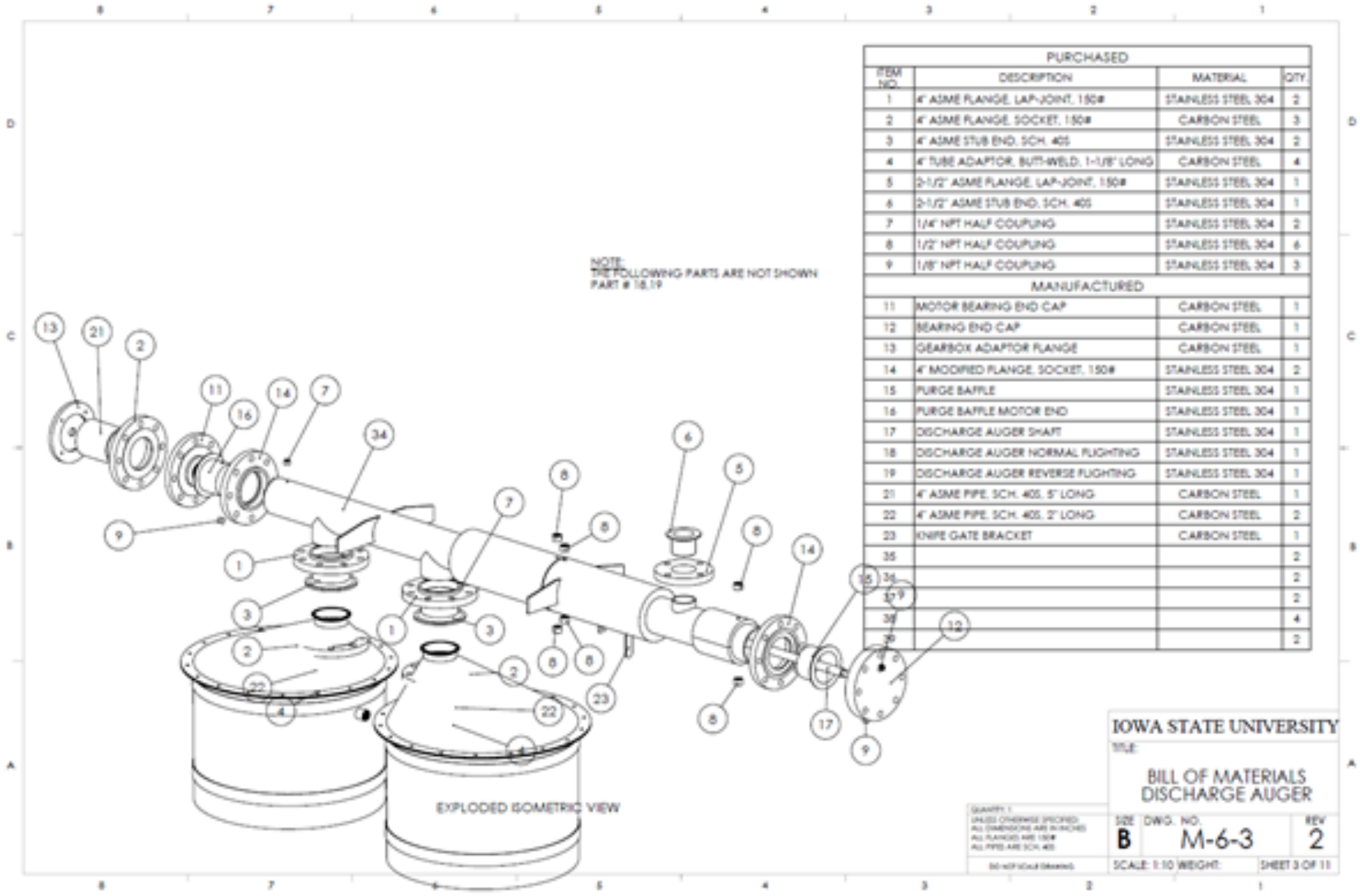

PURCHASED			
ITEM NO.	DESCRIPTION	MATERIAL	QTY.
1	4" ASME FLANGE, LAP-JOINT, 150#	STAINLESS STEEL 304	2
2	4" ASME FLANGE, SOCKET, 150#	CARBON STEEL	3
3	4" ASME STUB END, SCH. 40S	STAINLESS STEEL 304	2
4	4" TUBE ADAPTOR, BUTT-WELD, 1-1/8" LONG	CARBON STEEL	4
5	2-1/2" ASME FLANGE, LAP-JOINT, 150#	STAINLESS STEEL 304	1
6	2-1/2" ASME STUB END, SCH. 40S	STAINLESS STEEL 304	1
7	1/4" NPT HALF COUPLING	STAINLESS STEEL 304	2
8	1/2" NPT HALF COUPLING	STAINLESS STEEL 304	6
9	1/8" NPT HALF COUPLING	STAINLESS STEEL 304	3
MANUFACTURED			
11	MOTOR BEARING END CAP	CARBON STEEL	1
12	BEARING END CAP	CARBON STEEL	1
13	GEARBOX ADAPTOR FLANGE	CARBON STEEL	1
14	4" MODIFIED FLANGE, SOCKET, 150#	STAINLESS STEEL 304	2
15	PURGE BAFFLE	STAINLESS STEEL 304	1
16	PURGE BAFFLE MOTOR END	STAINLESS STEEL 304	1
17	DISCHARGE AUGER SHAFT	STAINLESS STEEL 304	1
18	DISCHARGE AUGER NORMAL FLIGHTING	STAINLESS STEEL 304	1
19	DISCHARGE AUGER REVERSE FLIGHTING	STAINLESS STEEL 304	1
21	4" ASME PIPE, SCH. 40S, 5" LONG	CARBON STEEL	1
22	4" ASME PIPE, SCH. 40S, 2" LONG	CARBON STEEL	2
23	KNIFE GATE BRACKET	CARBON STEEL	1
35			2
36			2
37			2
38			4
39			2

IOWA STATE UNIVERSITY

TITLE:
BILL OF MATERIALS
DISCHARGE AUGER

SIZE	DWG. NO.	REV
B	M-6-3	2

SCALE: 1:10 WEIGHT: SHEET 3 OF 11

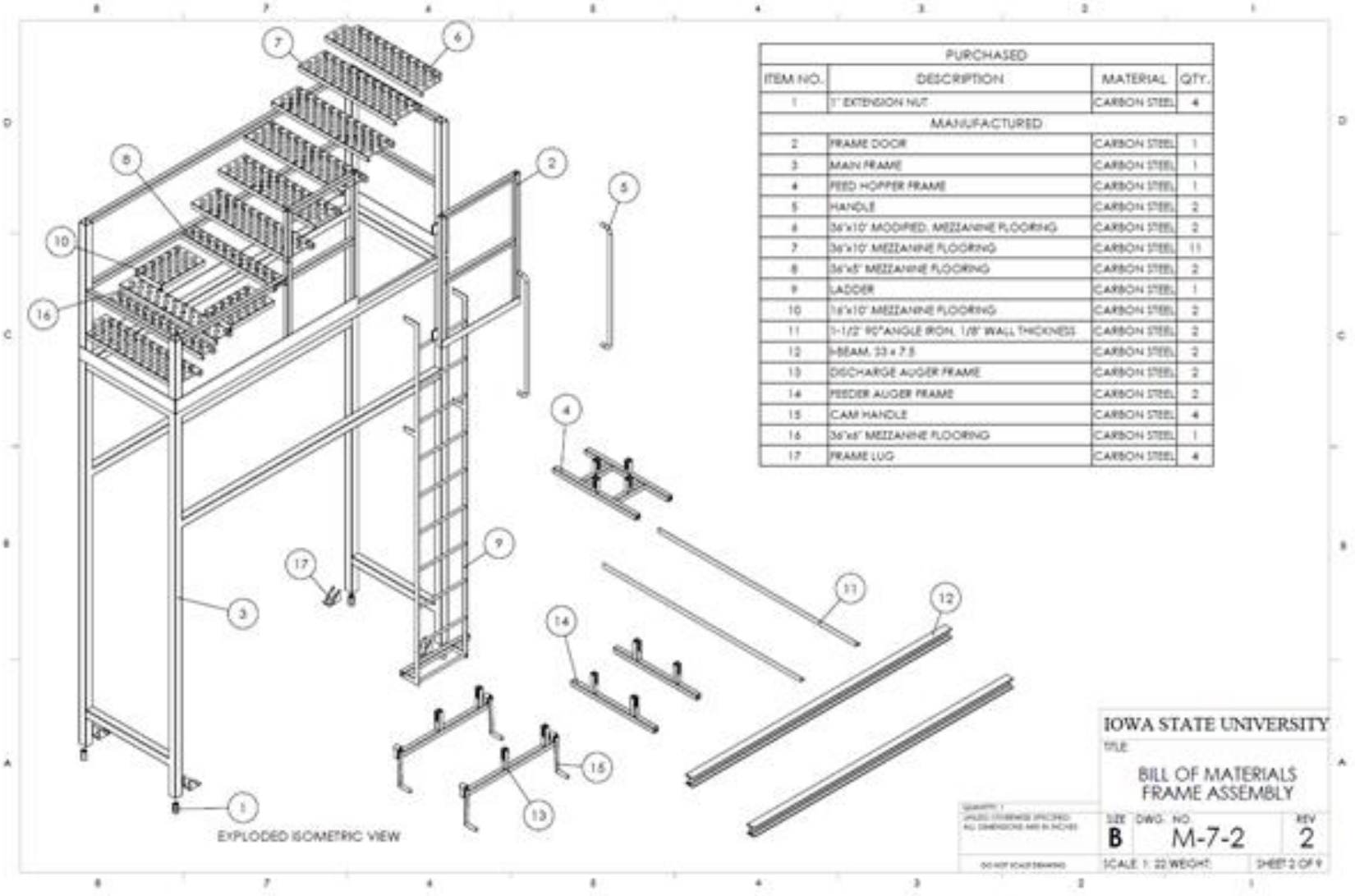

PURCHASED			
ITEM NO.	DESCRIPTION	MATERIAL	QTY.
1	1" EXTENSION NUT	CARBON STEEL	4
MANUFACTURED			
2	FRAME DOOR	CARBON STEEL	1
3	MAIN FRAME	CARBON STEEL	1
4	FEED HOPPER FRAME	CARBON STEEL	1
5	HANDLE	CARBON STEEL	2
6	36"x10" MODIFIED. MEZZANINE FLOORING	CARBON STEEL	2
7	36"x10" MEZZANINE FLOORING	CARBON STEEL	11
8	36"x5" MEZZANINE FLOORING	CARBON STEEL	2
9	LADDER	CARBON STEEL	1
10	18"x10" MEZZANINE FLOORING	CARBON STEEL	2
11	1-1/2" 90°ANGLE IRON, 1/8" WALL THICKNESS	CARBON STEEL	2
12	I-BEAM, 33 x 7.5	CARBON STEEL	2
13	DISCHARGE AUGER FRAME	CARBON STEEL	2
14	FEEDER AUGER FRAME	CARBON STEEL	2
15	CAM HANDLE	CARBON STEEL	4
16	36"x6" MEZZANINE FLOORING	CARBON STEEL	1
17	FRAME LUG	CARBON STEEL	4

IOWA STATE UNIVERSITY

TITLE: BILL OF MATERIALS FRAME ASSEMBLY

SIZE B | DWG. NO. M-7-2 | REV 2

SCALE: 1: 22 WEIGHT: | SHEET 2 OF 9

APPENDIX D : HEATING AUGER DESIGN

Plug Flow Reactor:

$T_{in} := 298.15K$ $T_{out} := 773.15K$

Material: Quartz Silica

Properties: 1105 Rock, Quartzite Sioux
Table A.3, pg. 940 - Fundamentals of Heat and Mass Transfer

Granule Properties

$c_{pg} := 1000\frac{J}{kg \cdot K}$ $k_g := 6.5\frac{W}{m \cdot K}$

$\rho_g := 1565\frac{kg}{m^3}$ $\varepsilon_g := 0.90$

Emissivity from Table A.11, pg. 956 - Fundamentals of Heat and Mass Transfer

$m_{dotg} := 20\frac{kg}{hr}$

$q := m_{dotg} \cdot c_{pg} \cdot (T_{out} - T_{in})$

Required Heat Input

$q = 2.639 \times 10^3 \cdot W$

Auger Properties

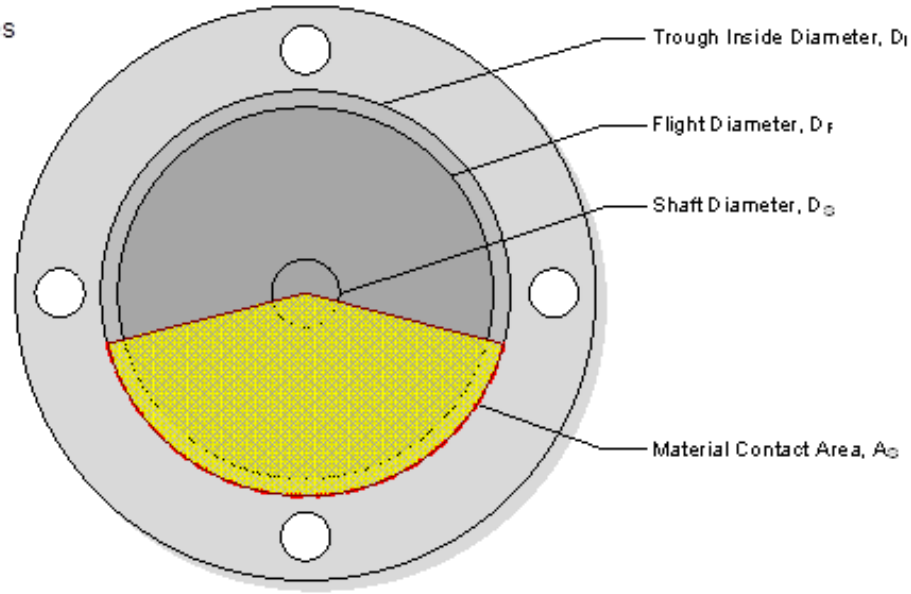

Heating Auger Specifications

$D_i := 4.026in$ $D_f := 3.5in$ $D_s := 1in$ $P := 0.4$ $D_o := 4.5in$

$RPM := 0.94\frac{rev}{min}$

Net Area

$NA := \frac{(\pi)}{4}\cdot\left(D_f^2 - D_s^2\right)$ $NA = 8.836in^2$

Equations from Table 4.7, pg. 155- Bulk Materials Handling Handbook Frucktbaum, Jacob

Full Capacity for one turn

$FC_1 := NA\cdot D_s$ $FC_1 = 8.836in^3$ $FC_1 = 1.448\times 10^{-4}\cdot m^3$

Full Capacity Flow Rate

$FC_2 := FC_1\cdot RPM$ $FC_2 = 0.051\frac{m^3}{hr}$ $m_{FC2} := FC_2\cdot\rho_g$

$RPM = 0.098\frac{1}{s}$ $FC_2 = 1.812\frac{ft^3}{hr}$ $m_{FC2} = 80.3\frac{kg}{hr}$

Assume a Capacity Percentage

$C := 0.5$

Standard-Pitch, Paddle Conveyor Capacity, with Fill Capacity Factor

$C_{paddle} := 0.5$ $C_{pitch} := 1$

$m_P := m_{FC2}\cdot C\cdot C_{paddle}\cdot C_{pitch}$

$m_P = 20.075\frac{kg}{hr}$

Heat Transfer

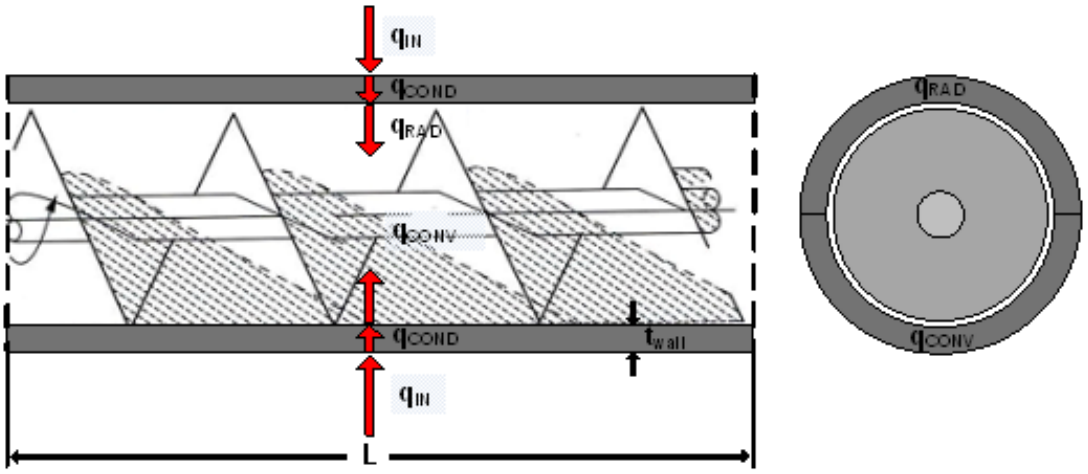

Assume:

$T_g := T_{out}$ $T_o := T_{in}$ $T_i := 873K$

$k_{ss304} := 22.6\frac{W}{m \cdot K}$ Properties: 304 Stainless Steel, 800K
Table A.1, pg. 931 - Fundamentals of Heat and Mass Transfer

$\varepsilon_{ss} := 0.33$ Properties: 304 Stainless Steel, 800K
Table A.11, pg. 954 - Fundamentals of Heat and Mass Transfer

$\rho_{ss} := 7900\frac{kg}{m^3}$ Properties: 304 Stainless Steel
Table A.1, pg. 931 - Fundamentals of Heat and Mass Transfer

$\alpha_{ss} := 18.4\frac{\mu m}{m \cdot K}$ Properties: 304 Stainless Steel, 500C
AK Steel Corp. - Data sheet

$h_{auger} := 20\frac{W}{m^2 \cdot K}$ HT coefficient 11-34 W/m^2*C,
pp11-64, Perry's Chemical Engineers' Handbook, 7th Edition

$q_{in} := 4\frac{W}{cm^2}$ Information obtained from Watlow ceramic fiber heater specification sheet $T_{max} := 1255K$

$$q_{cond} := \frac{(T_o - T_i)}{\frac{\ln\left(\frac{D_i}{D_o}\right)}{2 \cdot \pi \cdot L \cdot k_{ss304}}}$$

Adapted from Eqn 3.27, pg. 117 - Fundamentals of Heat and Mass Transfer

$q_{cond} := q_{in}(\pi \cdot D_o \cdot L)$ $L := 7.238ft$ From solve block below

$A_s := \pi \cdot D_i \cdot L$

$q_{conv} := h_{auger} \cdot C \cdot A_s \cdot (T_i - T_g)$ $q_{conv} = 215.702\frac{W}{ft}$

Radiation Heat Transfer

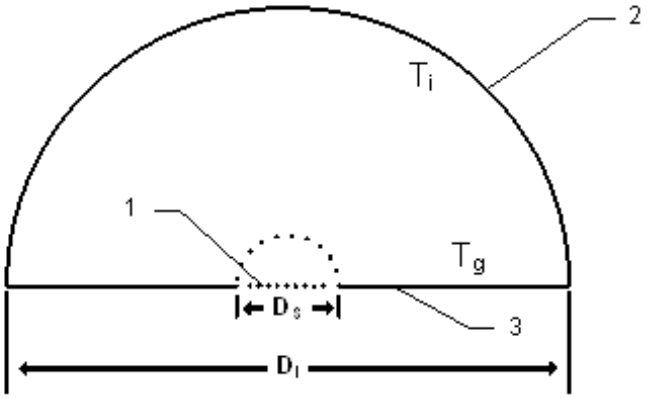

Assume shaft is flat w hen caclulating view factor, F_{23}

$A_1 := D_s$

$A_2 := \frac{\pi D_i}{2}$

$A_3 := D_i - D_s$

$F_{12} := 1$

$F_{23} := F_{12} \cdot \frac{D_i - D_s}{\frac{\pi \cdot D_i}{2}}$ $\quad F_{23} = 0.478$

$\sigma := 5.6710^{-8} \frac{W}{m^2 \cdot K^4}$

$q_{radBB} := (1 - C) A_s \cdot F_{23} \cdot \sigma \cdot \left(T_i^4 - T_g^4 \right)$

Adapted from Eqn 13.17, pg. 830 - Fundamentals of Heat and Mass Transfer

$$q_{rad} := \frac{\left[\sigma \cdot \left(T_i^4 - T_g^4 \right) \right]}{\left(\frac{1 - \varepsilon_{ss}}{\varepsilon_{ss} \cdot A_2} \right) + \frac{1}{(A_2 \cdot F_{23})} + \left(\frac{1 - \varepsilon_g}{\varepsilon_g \cdot A_3} \right)}$$

Adapted from Eqn 13.18, pg. 832 - Fundamentals of Heat and Mass Transfer

$q_{rad} = 142.566 \frac{W}{ft}$

Solve Block

Assume:

$T_i := 107K$ $T_g := 77K$ $q = 2.639 \times 10^3 W$

Guess

$L := 0.5m$

Given

$$q = h_{auger} \cdot \frac{\pi \cdot D_i \cdot L}{2} \cdot \left(T_i - T_g\right) + \frac{\left[\sigma \cdot \left(T_i^4 - T_g^4\right)\right]}{\left(\frac{1 - \varepsilon_{ss}}{\varepsilon_{ss} \cdot \frac{\pi D_i}{2} \cdot L}\right) + \frac{1}{\left(\frac{\pi D_i}{2} \cdot L \cdot F_{23}\right)} + \left[\frac{1 - \varepsilon_g}{\varepsilon_g \cdot \left(D_i - D_s\right) \cdot L}\right]}$$

$Z := Find(L)$

$Z = 2.895ft$

APPENDIX E : MBGF CONTROL SYSTEM AND HMI

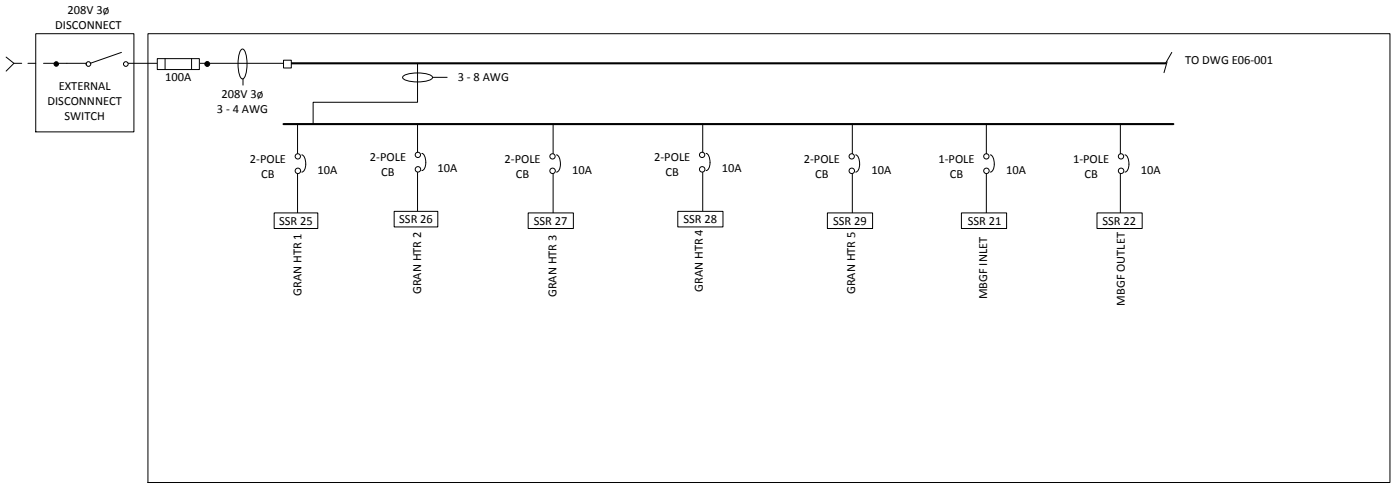

Revisions:	Reference :	Notes	Title:	Iowa State University, Ames, Iowa
	CONFIDENTIAL	MAIN I/O PANEL 208V ONE-LINE	Moving Bed Granule Filter	DES L. Whitmer · APP · DR. T. Heithoff · Cust. Ordr. No. xxxx-xxxx · Date: 7-30-2010
		Scale: None	Cust: Interstates Control Systems	Size B · Drawing No. E200-000 · Rev. 1

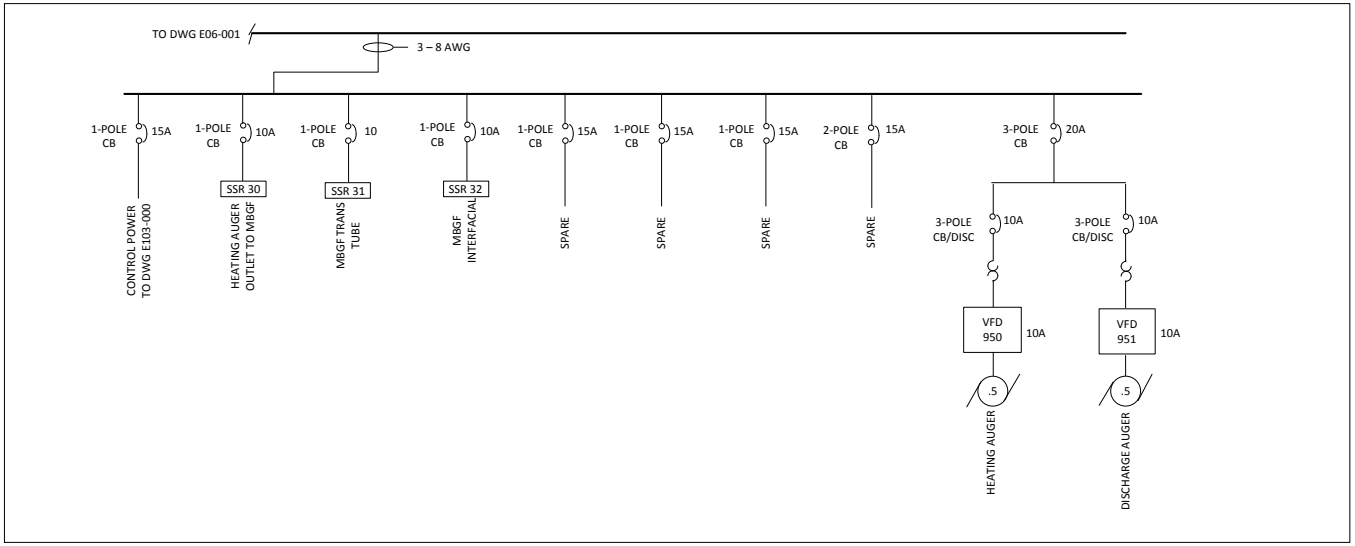

Revisions:	Reference :	Notes	Title:	
	CONFIDENTIAL	MAIN I/O PANEL 208V ONE-LINE	Moving Bed Granule Filter	Iowa State University, Ames, Iowa
		Scale: None	Cust: Interstates Control Systems	DES L. Whitmer; APP; DR. T. Heithoff; Cust. Ordr. No. xxxx-xxxx; Date: 7-30-2010; Size B; Drawing No. E200-001; Rev. 1

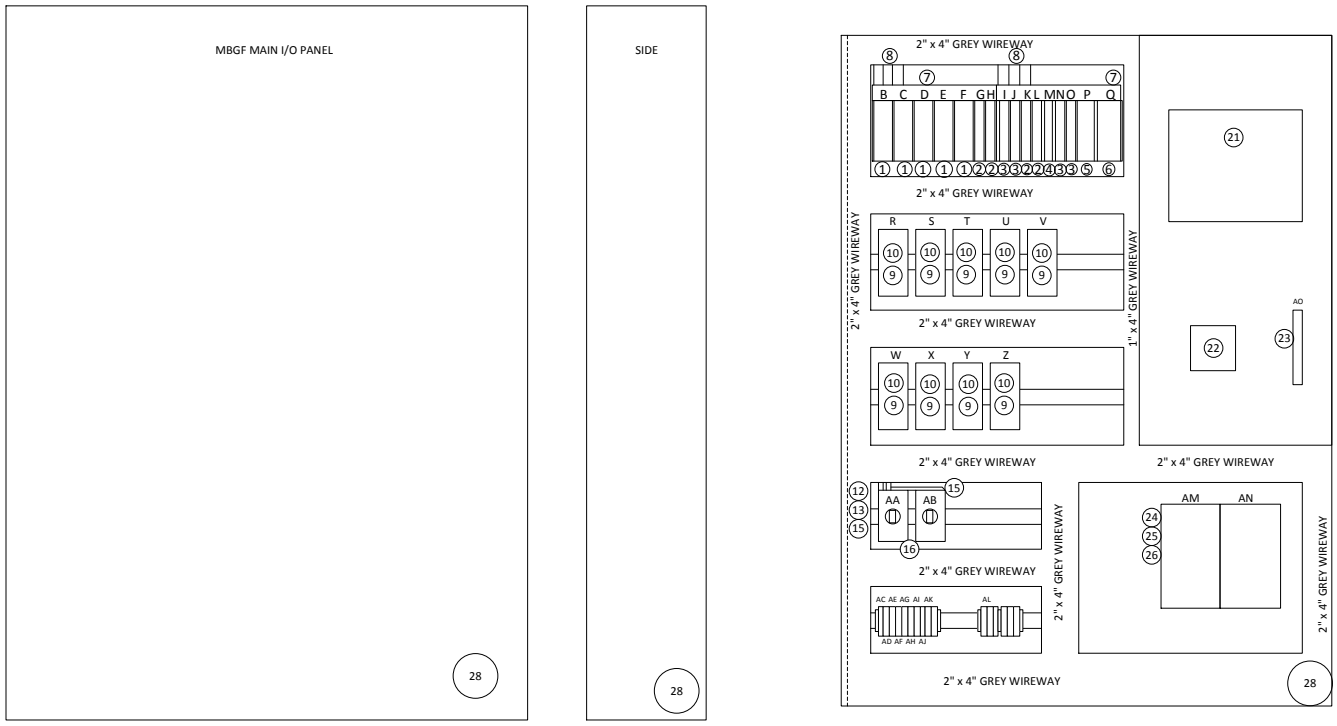

Revisions:	Reference : **CONFIDENTIAL**	Notes: MAIN I/O PANEL LAYOUT	Title: Moving Bed Granule Filter	Iowa State University, Ames, Iowa
		Scale: None	Cust: Interstates Control Systems	DES L. Whitmer; APP; DR. T. Heithoff; Cust. Ordr. No. XXXX-XXXX; Date: 7-30-2010; Size B; Drawing No. E202-000; Rev. 1

BOM

Number	Quantitiy	Description
1	5	A-B 1489-A2C100 10AMP 2-POLE MINI CB
2	4	A-B 1489-A1C060 6AMP 1-POLE MINI CB
3	4	A-B 1489-A1C150 15AMP 1-POLE MINI CB
4	1	A-B 1489-A1C050 5AMP 1-POLE MINI CB
5	1	A-B 1489-A2C150 15AMP 2-POLE MINI CB
6	1	A-B 1489-A3C200 20AMP 3-POLE MINI CB
7	2	1489 AACL312 BUS BAR 3 PHASE 12
8	6	1489 AACLT35 BUS BAR 3 TERMINAL LUG
9	9	700 SH25GZ24 SOLID STATE RELAY
10	9	700 SN25 HEAT SINK
11	AS REQUIRED	DIN RAIL SEPARATION BLOCK
12	2	140M-C2E-C10 MAN MTR STARTER
13	2	140M-C-AFA11 AUXILLARY CONTACT, FRONT
14	2	140M-C-KRY LOCKABLE TWIST KNOB, RED
15	1	140M-C-W453 COMPACT BUS-BAR SPACING, 45MM, FOR 140M-C
16	1	140M-C-WTE COMMONING LINK **REPLACES 140M-CWT
17	AS REQUIRED	1492-W4-BL BLACK TERMINAL
18	AS REQUIRED	1492-W4-G GREEN TERMINAL
19	AS REQUIRED	1492-EB3 END BARRIER
20	AS REQUIRED	1492-WFB4250 FUSE BLOCK WITH LED INDICATOR
21	1	100AMP 3 PHASE FUSE BLOCK
22	1	LD2570-3 DISTRIBUTION BLOCK
23	1	NUETRAL BAR
24	2	A-B 22B-B2P3N104 POWERFLEX 40
25	2	22B-CCB COMMUNICATION ADAPTER COVER FOR B-FRAME PF40
26	2	A-B 22-COMM-E PF40 ETHERNET/IP ADAPTER
27	AS REQUIRED	DIN RAIL
28	1	N4483608 - WEIGMANN TYPE 4 WALL MOUNT PANEL W/ BACKPLATE

TAGS

Tag	Lines	Text	Tag	Lines	Text	Tag	Lines	Text
A	1	MBGF Main I/O Panel	N	1	SPARE	AF	1	SSR
B	1	GRANULE	O	1	SPARE		2	26
	2	HEATER 1	P	1	SPARE	AG	1	SSR
C	1	GRANULE	Q	1	MOTORS		2	27
	2	HEATER 2	R	1	SSR 21	AH	1	SSR
D	1	GRANULE	S	1	SSR 22		2	28
	2	HEATER 3	T	1	SSR 25	AI	1	SSR
E	1	GRANULE	U	1	SSR 26		2	29
	2	HEATER 4	V	1	SSR 27	AJ	1	SSR
F	1	GRANULE	W	1	SSR 28		2	30
	2	HEATER 5	X	1	SSR 29	AK	1	SSR
G	1	MBGF	Y	1	SSR 30		2	31
	2	INLET	Z	1	SSR 31	AL	1	TB5
H	1	MBGF	AA	1	VFD 950	AM	1	VFD 950
	2	OUTLET		2	HEATING	AN	1	VFD 951
I	1	CONTROL	AB	1	VFD 951	AO	1	NUETRAL BAR
	2	VOLTAGE		2	DISCHARGE			
J	1	AUGER OUT	AC	1	SSR			
	2	TO MBGF		2	21			
K	1	TRANSPORT	AD	1	SSR			
	2	TUBE		2	22			
L	1	INTERFACIAL	AE	1	SSR			
M	1	SPARE		2	25			

Revisions:

Reference :

CONFIDENTIAL

Notes

BOM AND TAGS FOR MAIN I/O PANEL

Scale: None

Title:

Moving Bed Granule Filter

Cust: Interstates Control Systems

Iowa State University
Ames, Iowa

DES	L. Whitmer	APP	
DR.	T. Heithoff	Cust. Ordr. No. XXXX-XXXX	Date: 7-30-2010
Size B	Drawing No. F202-001		Rev. 1

NUMBER	QUANTITY	DESCRIPTION
29	2	1734-AENT POINT I/O ETHERNET/IP ADAPTER
30	3	1734-EP24DC 24VDC PWR EXTEN MOD
31	20	1734-IT2I 24VDC TEMP INPUT
32	4	1734-232ASC RS232 ASCII INTERFACE
33	2	1734-OE2V VOLTAGE ANALOG OUTPUT MODULE
34	1	1734-OE2C CURRENT ANALOG OUTPUT MODULE
35	2	1734-OW2 24VDC COIL N.O.
36	3	1734-OB8E 24VDC 8 CHANNEL
37	2	1734-IB8 24VDC 8 CHANNEL
38	6	1734-IE2C CURRENT ANALOG IN
39	1	1783-SMO8T ETHERNET SWITCH
40	20	1734-TBCJC SCREW TERMINAL BASE
41	1	PSM24-180S RHINO 24VDC 180W 7.5A PWR SUPPLY
42	20	1734-TB3 SCREW TERMINAL BASE
43	AS REQUIRED	199-DR1 DIN MOUNTING RAIL
44	AS REQUIRED	1492-W4-B BLUE TERMINAL
45	AS REQUIRED	1492-W4-W WHITE TERMINAL
46	AS REQUIRED	1492-W4-G GREEN TERMINAL
47	10	1492-WFB424
48	5	1492-WFB4250
49	1	1734-FPD
50	1	N4303008 WEIGMANN TYPE 4 WALLMOUNT PANEL W/ BACKPLATE

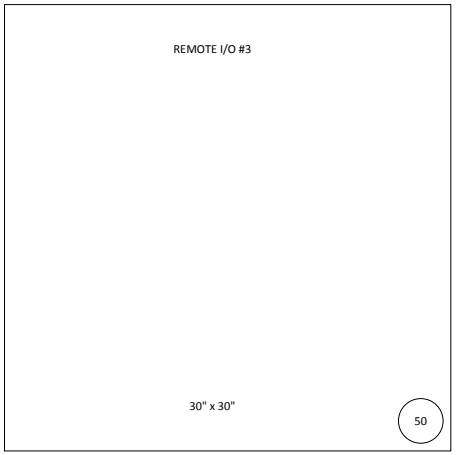

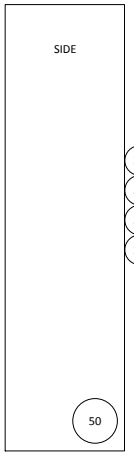

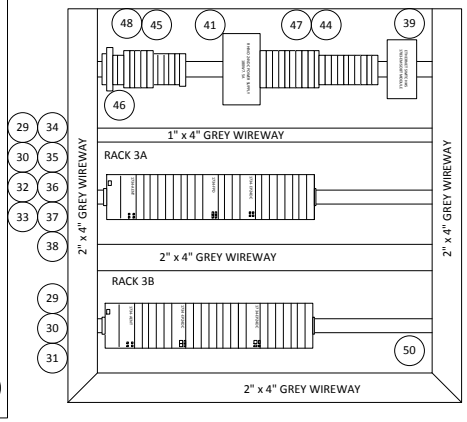

Revisions:	Reference : **CONFIDENTIAL**	Notes: REMOTE I/O #3 PANEL ENCLOSURE	Title: Moving Bed Granule Filter	Iowa State University, Ames, Iowa
		Scale: None	Cust: Interstates Control Systems	DES L. Whitmer; APP; DR. T. Heithoff; Cust. Ordr. No. XXXX-XXXX; Date: 7-30-2010; Size B; Drawing No. E202-003; Rev. 1

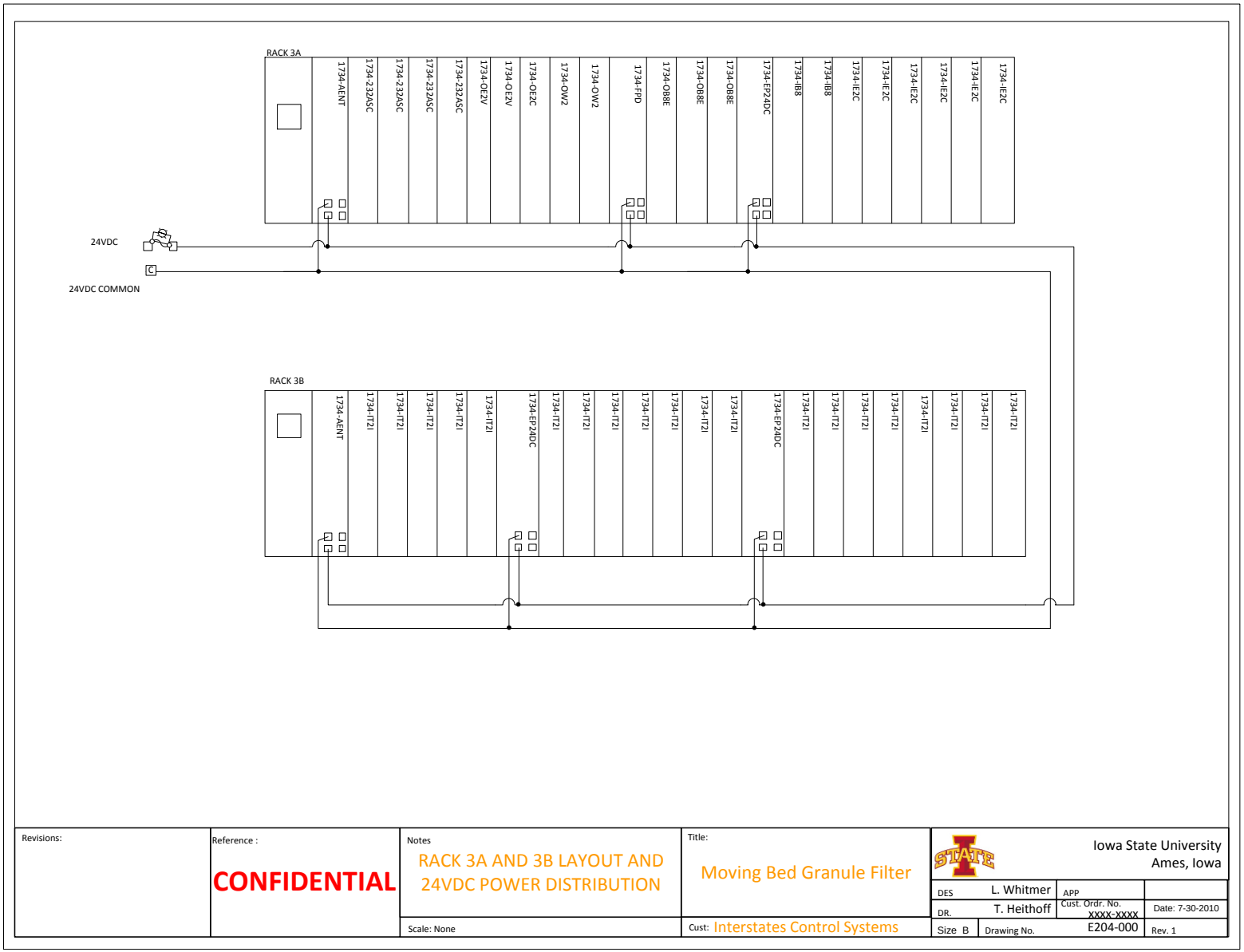

Revisions:	Reference : **CONFIDENTIAL**	Notes: RACK 3A AND 3B LAYOUT AND 24VDC POWER DISTRIBUTION	Title: Moving Bed Granule Filter	Iowa State University, Ames, Iowa
		Scale: None	Cust: Interstates Control Systems	DES: L. Whitmer; DR.: T. Heithoff; APP; Cust. Ordr. No.: XXXX-XXXX; Date: 7-30-2010; Size B; Drawing No.: E204-000; Rev. 1

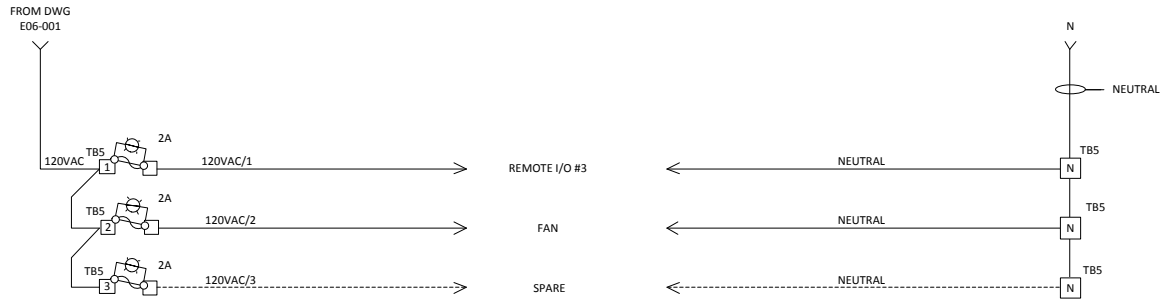

Revisions:	Reference : **CONFIDENTIAL**	Notes: MAIN I/O PANEL 120V PWR DIST	Title: Moving Bed Granule Filter	Iowa State University, Ames, Iowa
		Scale: None	Cust: Interstates Control Systems	DES: L. Whitmer; APP: ; DR.: T. Heithoff; Cust. Ordr. No.: XXXX-XXXX; Date: 7-30-2010; Size B; Drawing No.: E203-000; Rev. 1

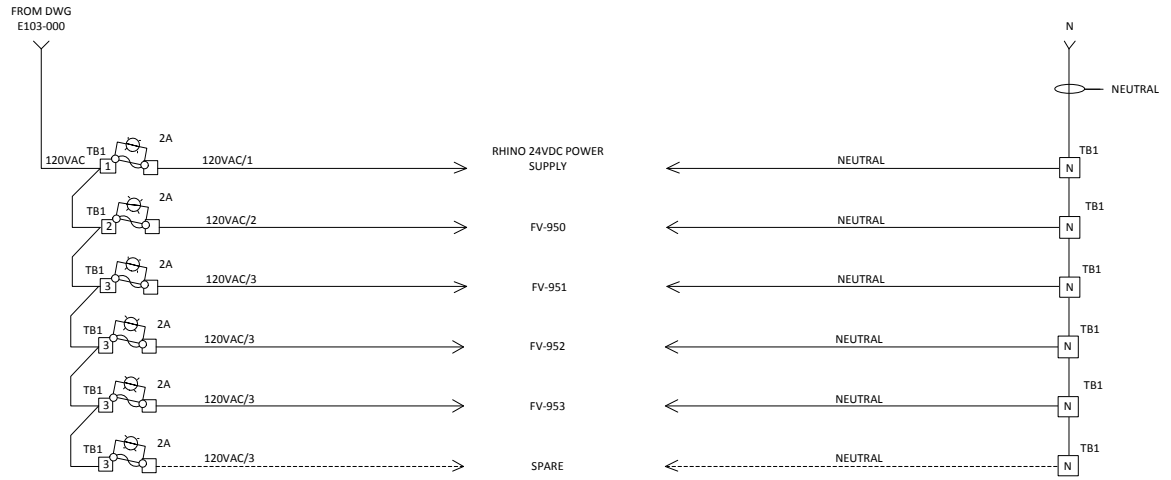

Revisions:	Reference : **CONFIDENTIAL**	Notes: REMOTE I/O #3 PANEL 120V PWR DIST	Title: Moving Bed Granule Filter	Iowa State University, Ames, Iowa	
		Scale: None	Cust: Interstates Control Systems	DES L. Whitmer / DR. T. Heithoff / APP / Cust. Ordr. No. XXXX-XXXX / Size B / Drawing No. E203-001	Date: 7-30-2010 / Rev. 1

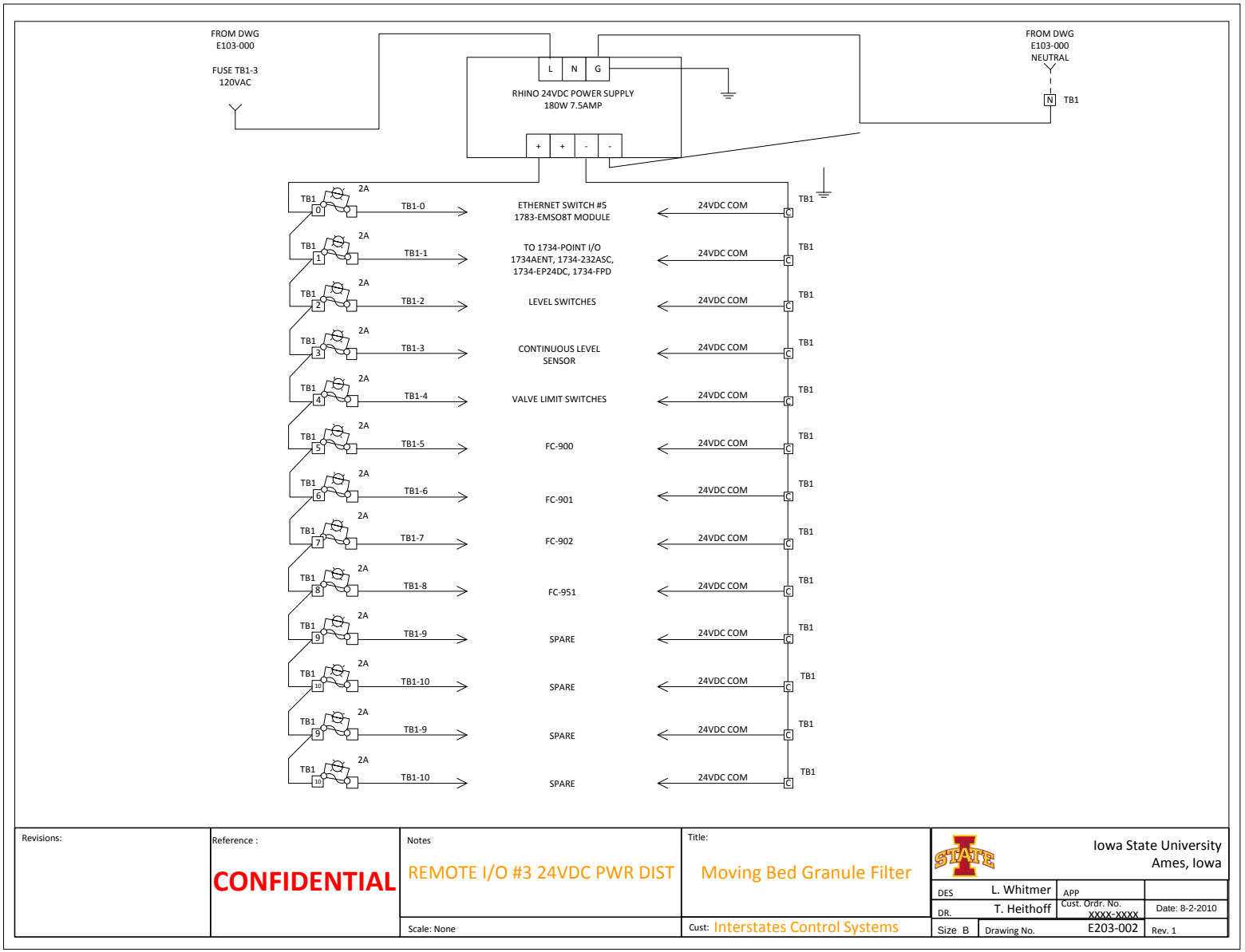

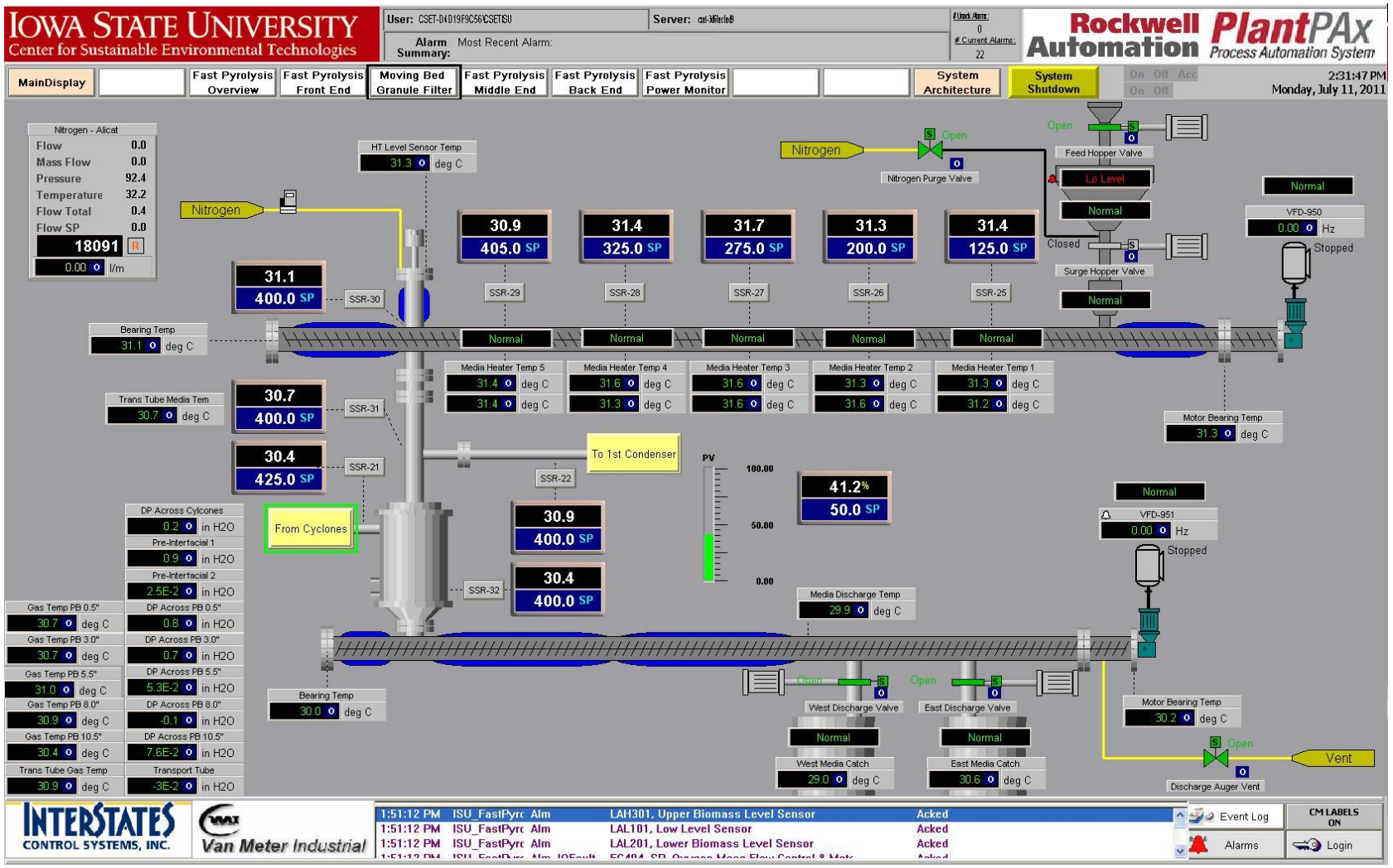

APPENDIX F : SECONDARY CHAR GENERATION TEST

A test was performed with the goal of obtaining a sample of primarily secondary reaction derived char in an effort to compare structures with char from MBGF samples. To this end, a bench scale drop-tube reactor was modified using a high temperature silica fiber barrier filter located at the gas exit. Primary char particles entrained in the pyrolysis gas flow will collect on the barrier filter surface forming a filter cake. As the filter cake becomes denser with particles, the void space decreases and the pyrolysis vapors are forced to pass through the primary char matrix. The pyrolysis vapors crack into additional char and water vapor in the presence of the primary char in what is referred to as "secondary reactions." The secondary char was collected from the barrier filter surface for additional analysis.

Table 8 displays a yield comparison between the test run in order to obtain secondary char (7-20110501) and a test run at typical operating conditions (7-20090112) as presented by Ellens et al.[48] The test with the barrier filter in place resulted in increased char and gas content while decreasing bio-oil content. These are typical indications that secondary reaction have occurred. Unfortunately, the oil was not analyzed for water content to provide further evidence of secondary reactions.

Table 8: Drop Tube Reactor Test Yield Comparison [48]

Test	Mass Fed	Cyclone Char	Filter Char	SF1	SF2	SF3	SF4	NCG	Unaccounted
7-20110501									
Collected Mass (g)	452.1	83.0	4.3	190.1	8.9	37.9	3.5	123.2	-
Yield Percentage	-	18.4%	1.0%	42.0%	2.0%	8.4%	0.8%	27.2%	0.3%
7-20090112									
Collected Mass (g)	1312.1	207.3	N/A	496.3	249.0	129.8	7.9	191.3	-
Yield Percentage	-	15.8%	N/A	37.8%	19.0%	9.9%	0.6%	14.6%	2.3%

Details regarding the non-condensable gas composition of both tests can be found in Figure 56 and Figure 57. Testing using the barrier filter resulted in a clear reduction of carbon dioxide in favor of an increase in carbon monoxide content. Slight increases in both hydrogen and methane were present over baseline levels.

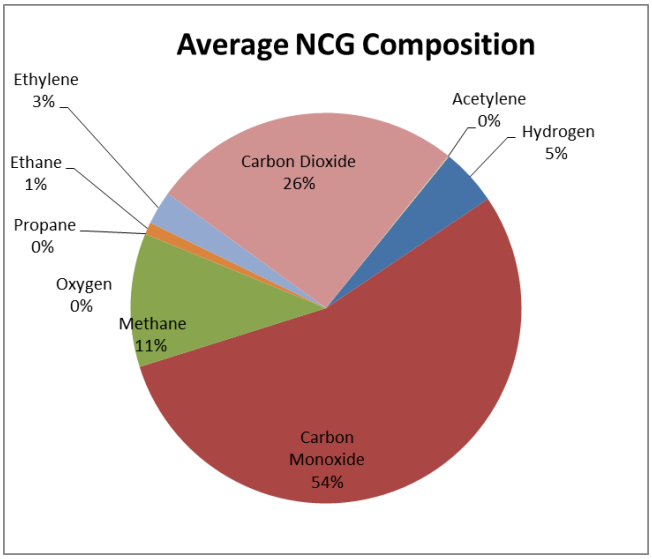

Figure 56: Secondary Char Generation Test Non-Condensable Gas Composition

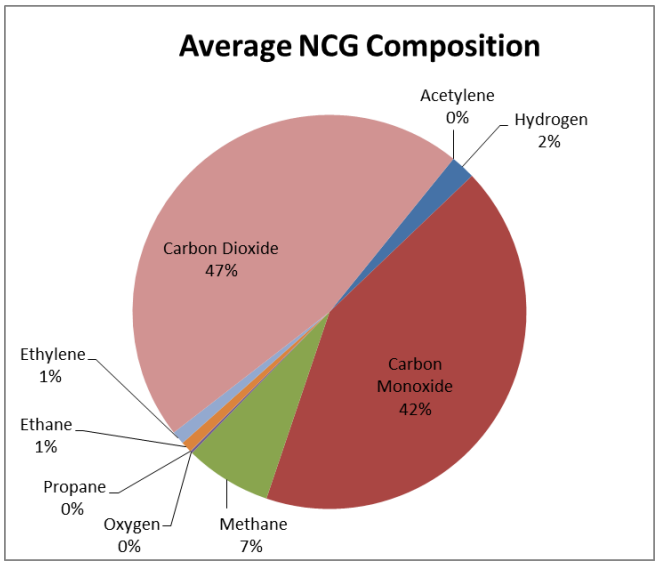

Figure 57: Baseline Non-Condensable Gas Composition [48]

APPENDIX G : GPC BASELINE COMPARATIVE DATA

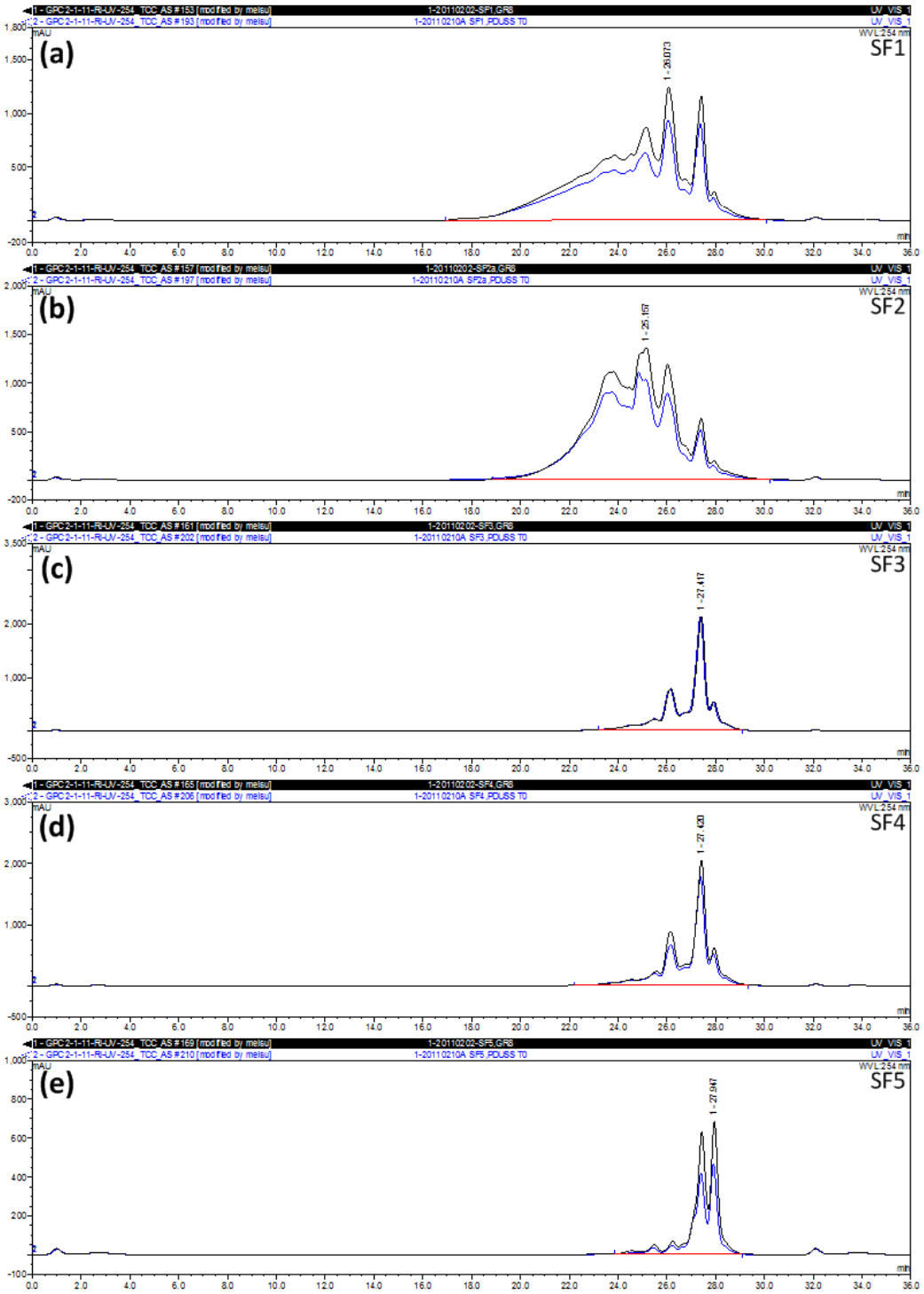

Figure 58: GPC Molecular Weight Curve Comparison between GR8 MBGF and PDU Baseline Operation for a) SF1, b) SF2, c) SF3, d) SF4, and e) SF5

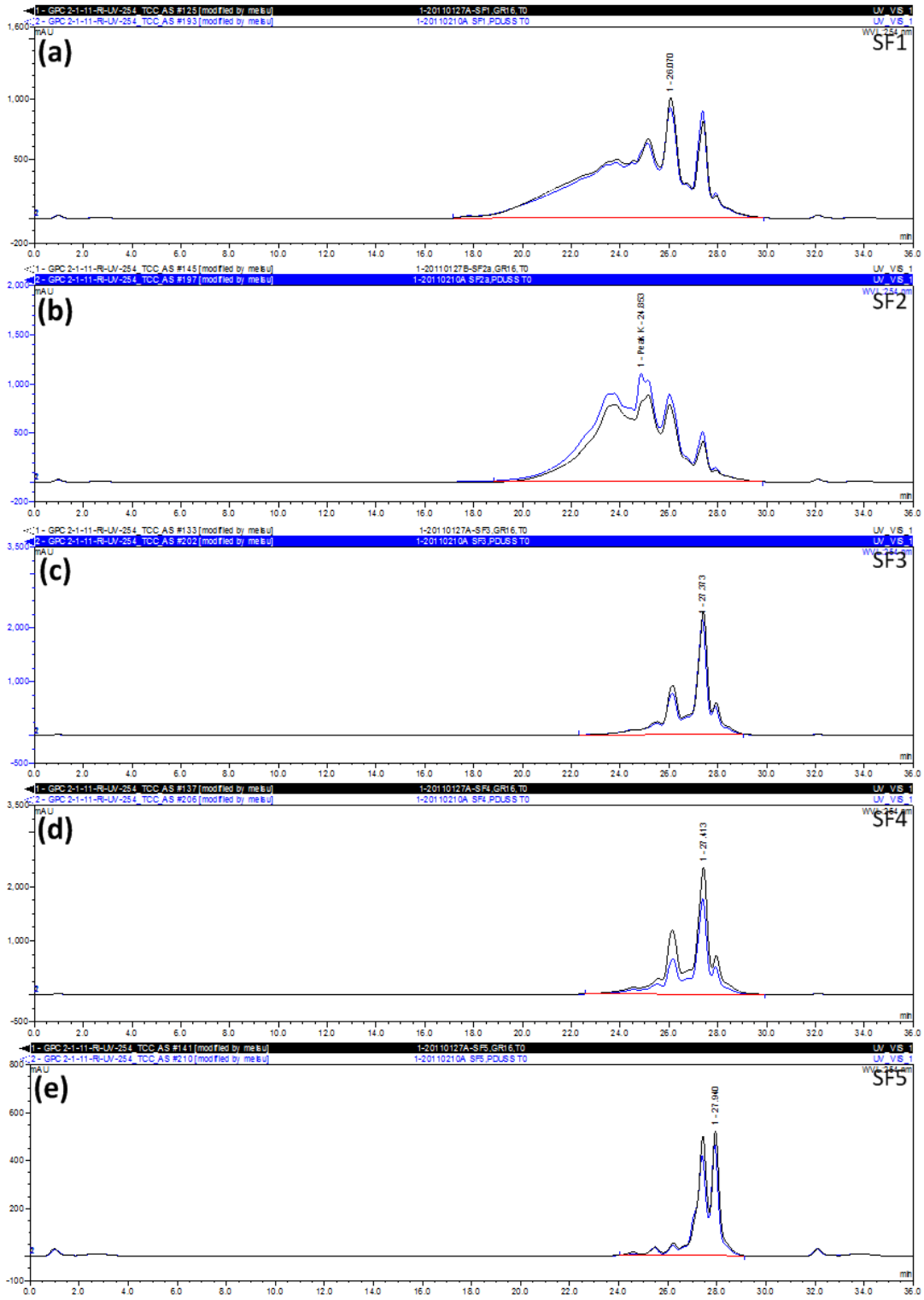

Figure 59: GPC Molecular Weight Curve Comparison between GR16 MBGF and PDU Baseline Operation for a) SF1, b) SF2, c) SF3, d) SF4, and e) SF5